

Dissertation presented to the Instituto Tecnológico de Aeronáutica, in partial fulfillment of the requirements for the degree of Master of Science in the Graduate Program of Physics, Field of Nuclear Physics.

Sarah Villanova Borges

**EMISSION MODELS OF SOFT GAMMA-RAY
REPEATERS/ANOMALOUS X-RAY PULSARS
DESCRIBED AS WHITE DWARFS**

Dissertation approved in its final version by signatories below:



Prof^a. Dr^a. Cláudia Vilega Rodrigues

Advisor

Prof. Dr. Pedro Teixeira Lacava
Dean for Graduate Education and Research

Campo Montenegro
São José dos Campos, SP - Brazil
2018

**Cataloging-in Publication Data
Documentation and Information Division**

Borges, Sarah Villanova
Emission models of Soft Gamma-Ray Repeaters/Anomalous X-Ray Pulsars described as White
Dwarfs / Sarah Villanova Borges.
São José dos Campos, 2018.
137f.

Dissertation of Master of Science – Course of Physics. Area of Nuclear Physics – Instituto
Tecnológico de Aeronáutica, 2018. Advisor: Prof^{ca}. Dr^a. Cláudia Vilega Rodrigues.

1. Cupim. 2. Dilema. 3. Construção. I. Instituto Tecnológico de Aeronáutica. II. Title.

BIBLIOGRAPHIC REFERENCE

BORGES, Sarah Villanova. **Emission models of Soft Gamma-Ray Repeaters/Anomalous X-Ray Pulsars described as White Dwarfs**. 2018. 137f. Dissertation of Master of Science – Instituto Tecnológico de Aeronáutica, São José dos Campos.

CESSION OF RIGHTS

AUTHOR'S NAME: Sarah Villanova Borges

PUBLICATION TITLE: Emission models of Soft Gamma-Ray Repeaters/Anomalous X-Ray Pulsars described as White Dwarfs.

PUBLICATION KIND/YEAR: Dissertation / 2018

It is granted to Instituto Tecnológico de Aeronáutica permission to reproduce copies of this dissertation and to only loan or to sell copies for academic and scientific purposes. The author reserves other publication rights and no part of this dissertation can be reproduced without the authorization of the author.

Sarah Villanova Borges
Itália St, 1325 E
89.806-165 – Chapecó - SC

EMISSION MODELS OF SOFT GAMMA-RAY REPEATERS/ANOMALOUS X-RAY PULSARS DESCRIBED AS WHITE DWARFS

Sarah Villanova Borges

Thesis Committee Composition:

Prof. Dr.	Rubens de Melo Marinho Júnior	President	-	ITA
Prof ^a . Dr ^a .	Cláudia Vilega Rodrigues	Advisor	-	INPE/ITA
Prof. Dr.	Jorge Ernesto Horvarth	External Member	-	USP
Prof. Dr.	João Braga	External Member	-	INPE

To my parents, Márcio e Rosane;
to my brother, Daniel;
to my lovely dog, Bolacha;
and to my grandmother Geralda.

Acknowledgments

I would like to thank my mother, Rosane, to inspire me and give me strength and support during all the hardest times of this journey. To my father, Márcio, for always encouraged me to be more curious. Thank you both for the unconditional love and to help me pursuing my dreams.

To my brother, Daniel for always being my best friend. To my dog, Bolacha, for showing me the meaning of fidelity.

To my grandmother Geralda, for always being at my side. To my aunts Lucília, Luciana, Simone and Sandra and to my cousins Marília, Catarina and Allan for being part of this wonderful family that always helps each other in the hard times.

To my advisor, Cláudia, for giving me an opportunity to work with astrophysics and for guiding my work during all those years.

To Professor Malheiro, for helping me with my research and bureaucratic matters during the last years of college and all my master. To Jaziel, for helping my research during all those years.

To CAPES for funding my research during this last couple of years.

*“E eu vos direi: “Amai para entendê-las!
Pois só quem ama pode ter ouvido
Capaz de ouvir e de entender estrelas”.”*

— OLAVO BILAC

Resumo

As fontes astrofísicas *Soft Gamma Repeaters* (SGR) e *Anomalous X-Ray Pulsars* (AXP) apresentam uma luminosidade quiescente em raios-X moles, no intervalo de 2 – 10 keV, da ordem de $10^{29} - 10^{35}$ erg.s⁻¹, período de 2–12 s e *spin-down* de 10^{-15} a 10^{-10} s.s⁻¹. Em geral, os SGR/AXPs apresentam *bursts* em altas energias, nos quais a luminosidade pode atingir 10^{43} erg.s⁻¹. A natureza da emissão desses SGR/AXPs é motivo de debate e vários cenários já foram propostos. O cenário mais aceito é o modelo magnetar. Neste modelo, as fontes SGR/AXPs apresentam um enorme campo magnético (B), da ordem de $10^{13} - 10^{15}$ G, e sua luminosidade quiescente em raios-X, bem como os *bursts*, são produzidos pelo decaimento de seus altíssimos campos magnéticos. No entanto, algumas limitações desse cenário, como a descoberta da fonte de baixo campo magnético ($< 10^{13}$ G) SGR 0418+5729, aumentaram o interesse por cenários alternativos nos últimos anos. Nesta dissertação, apresentamos um novo cenário para explicar a emissão de SGR/AXPs. Nós propomos que a emissão persistente vem de uma anã branca isolada, que acreta matéria de um disco de detritos. Para testar o modelo, ajustamos a emissão quiescente da AXP 4U 0142+61, que cobre uma ampla faixa de energia, do infravermelho médio aos raios-X duros. Obtivemos um bom ajuste para toda a SED, assumindo que as emissões óticas e infravermelhas são causadas pelo disco de poeira opticamente espesso e pela fotosfera da anã branca, que os raios-X duros são devidos à região pós-choque da coluna de acreção e que os raios-X moles são formados por uma mancha quente na superfície da anã branca. Os parâmetros ajustados apontam para uma anã branca rápida, massiva e altamente magnética. Tal anã branca provavelmente formou-se durante a coalescência de duas anãs brancas menos massivas. Nós também estimamos o campo magnético para os SGR/AXPs no cenário de acreção em anãs brancas e apresentamos novas estimativas de distância para 7 SGR/AXPs, incluindo 4U 0142+61.

Abstract

The Anomalous X-ray Pulsars (AXPs) and the Soft Gamma Repeaters (SGRs) present a quiescent soft X-ray luminosity, in the 2 – 10 keV range, of the order of $10^{31} - 10^{35}$ erg.s⁻¹, period of 2 – 12 s and spin-down of 10^{-14} to 10^{-10} s.s⁻¹. In general, the SGR/AXPs have already presented high-energy outburst events, in which the luminosity can achieve 10^{43} erg.s⁻¹. The nature of the SGR/AXPs emission is still reason for debate and several scenarios have been proposed. The most accepted scenario is the magnetar model. In this model, the SGR/AXPs present a huge magnetic field (B), from 10^{13} to 10^{15} G, and their persistent X-ray luminosity, as well as the bursts, are produced by the decay of their ultra strong magnetic fields. However, some limitations of this scenario, such as the discovery of a low-B ($< 10^{13}$ G) source, SGR 0418+5729, has increased the interest for alternative scenarios in the past few years. In this thesis, we present a new scenario to explain the emission of SGR/AXPs. We propose that the persistent emission comes from an accreting isolated white dwarf surrounded by a debris disk. To test the model, we fit the quiescent emission of the AXP 4U 0142+61, which covers a broad range of energy, from mid-infrared to hard X-rays. We obtained a good fit for the entire SED, assuming that the optical and infrared emissions are caused by the optically thick dusty disk and the white-dwarf photosphere, the hard X-rays are due to the post-shock region of the accretion column and the soft X-rays are formed by the heating of the white-dwarf surface. The fitted parameters point out to a white dwarf that is a fast rotator, massive and highly-magnetized. Such a white dwarf can be formed by a merger of two less massive white dwarfs. We also present new distance estimates for 7 SGR/AXPs, including 4U 0142+61, and estimate the magnetic field for the SGR/AXPs in the accreting white-dwarf scenario.

List of Figures

FIGURE 1.1 – Periods and magnetic field magnitude for different classes fo NSs. LMXB = Low-Mass X-ray Binaries; CCO = Central Compact Objects; MSP = Milliseconds Pulsars; HMXB = High-Mass X-ray Binaries; INS = Isolated NSs. This section contains a small definition of those classes. Reference: Harding (2013).	31
FIGURE 1.2 – Period versus period derivative. RRAT = Rotating Radio Transients. Reference: Harding (2013).	32
FIGURE 1.3 – Period versus magnetic field for some classes of NSs and WDs. Reference: Malheiro & Coelho (2013)	33
FIGURE 2.1 – Flux variation of 4U 0142+61 on Sep-10-2007 (dotted line) and Sep-12-2007 (solid line) relative to its phase for the i' band. Reference: Dhillon <i>et al.</i> (2005)	41
FIGURE 2.2 – Phase diagram of SGR 0501+4516 relative to its phase for the i' band flux. the upper profile is from Dec-31-08 and the bottom profile is from Jan-01-09. The solid and dotted lines represents the same data reduced by two different techniques. Reference: Dhillon <i>et al.</i> (2011)	41
FIGURE 2.3 – Flux variation of 1E 1048.1-5937 from Jun-09-2007 relative to its phase for the i' band. The solid and dotted lines represents the same data reduced by two different techniques. Reference: Dhillon <i>et al.</i> (2009)	42
FIGURE 2.4 – Photoelectric absorption cross section as a function of energy. The solid line is for relative abundances with all elements in the gas phase and in neutral atomic form. The dotted line shows the effect of condensing the fraction of each elements. The contributions of only hydrogen and only hydrogen + helium to the total cross section are also shown. Reference: Morrison & McCammon (1983).	43

- FIGURE 2.5 – Color-magnitude diagrams for two lines of sight for Galactic coordinates. Extinction causes a slight broadening in the K-giants strip for in-plane regions. The black dots is the position of the red clumps. The solid line shows the best fitted trace. The dashed lines show the limits for the red clump giants extraction within a width of 0.4 mag. Reference: : López-Corredoira *et al.* (2002). 50
- FIGURE 3.1 – Optical and infrared SED of 4U 0142+61 . The black crosses are from Wang *et al.* (2006, mid-infrared), Durant & van Kerkwijk (2006c, Gemini near-infrared) and Muñoz-Darias *et al.* (2016, optical); the orange crosses are from Dhillon *et al.* (2005); the blue crosses are from Hulleman *et al.* (2000), Hulleman *et al.* (2004); and the red crosses are from Morii *et al.* (2005). 59
- FIGURE 3.2 – Comparison between the long-term variability for the R, I and K bands as well as the soft x-ray emission. Reference: Durant & van Kerkwijk (2006c). 60
- FIGURE 3.3 – The top panel is the pulsed profile in the R band. The middle and bottom panel are the 1.0 – 2.0 keV and 0.5 – 1.0 keV soft X-ray pulsed profile by Chandra. Reference: Kern & Martin (2002). . . . 60
- FIGURE 3.4 – Optical spectrum of 4U 0142+61 (in red) and the spectrum of errors (in blue). The blue dots are the photometric values of SDSS bands. The dotted line marks the wavelength where we should see the $H\alpha$ lines. All the data were corrected by extinction ($E(B-V)=1.5$) .Reference: Muñoz-Darias *et al.* (2016). 61
- FIGURE 3.5 – 4U 0142+61 pulse profiles from soft to hard X-rays. In panels A, B and C, pulse profiles in the energy ranges 0.8-2.0 keV, 2.0-4.0 keV and 4.0-8.0 keV are the sums of the *XMM-Newton*. Panel D presents the *RXTE-PCA* pulse profile in the energy band 8.0-16.3 keV taken from Kuiper *et al.* (2006). In panels E and F *INTEGRAL* pulse profiles are shown in the energy ranges 20-50 keV and 50-160 keV. Phase interval blue (Ph. I) is the secondary pulsed from *INTEGRAL* profile, green (Ph. II) is the DC level from *INTEGRAL* profile and pink (Ph.III) is the main pulsed from *INTEGRAL* profile. 62

- FIGURE 3.6 – *left panel*: the phase-resolved pulsed-emission spectra and fits of INTEGRAL (square symbols) and RXTE-PCA (without markers) are presented. Black is the total-pulsed spectrum, the colored lines are from the same phases from fig 3.5 and the grey is the best power-law fit for the INTEGRAL total-spectrum and the power-law fit for the total-pulsed spectrum. The arrows indicate the flux measurements with a significance less than 1.5σ . For comparison the INTEGRAL/XMM-Newton-B total-spectrum fit is shown in black. *Right panel*: η is defined as the fraction of the pulsed emission in a selected phase interval Ph I, Ph II or Ph III of the total-pulsed emission, i.e. the sum equals unity. 63
- FIGURE 3.7 – Derreddened and deabsorbed SED of 4U 10142+61. The black crosses are from Wang *et al.* (2006, mid-infrared), Durant & van Kerkwijk (2006c, near-infrared) and Muñoz-Darias *et al.* (2016, optical); green crosses are soft X-rays from Enoto *et al.* (2010, Suzaku); and the magenta crosses are the 2003.12 data from Wang *et al.* (2014, INTEGRAL). 65
- FIGURE 3.8 – Magnetar fit to high-energy emission of 4U 0142+61 from Hascoët *et al.* (2014). The fit is composed by the cold blackbody (red), the hot (modified) blackbody (magenta), and the coronal outflow emission (blue). The dashed blue curve shows the best fit of the hard component obtained when only the phase-averaged spectrum is considered and the phase-resolved data are neglected. The data and model in the figure are not corrected for interstellar absorption. Reference: Hascoët *et al.* (2014). 66
- FIGURE 3.9 – Optical/infrared SED of 4U 0142+61 . The dot-dashed line represents the dust disk model, the dashed line is a blackbody component and the the dotted line is a power-law. The triangles are the observed data and the squares are the deabsorbed data for $A_v = 3.5$. The considered distance was 3.9 kpc. Reference: Wang *et al.* (2006). 67
- FIGURE 3.10 – *Suzaku* (black and red) and INTEGRAL (green) corrected from instrumental response spectra of 4U 0142+61 fitted with the XSPEC thermal and bulk Comptonization models. Reference: Zezas *et al.* (2015). 68

- FIGURE 3.11 – fit of 4U 0142+61 in the irradiated-disk (Ertan *et al.*, 2007). Circles are the absorbed data (taken from Hulleman *et al.* (2000), Hulleman *et al.* (2004), Morii *et al.* (2005), Durant & van Kerkwijk (2006c), and triangles are data dereddened ($A_V = 3.5, 2.6$). Squares are the irradiated-disk model energy flux. Reference: Ertan *et al.* (2007). 69
- FIGURE 3.12 – Fit of 4U 0142+61 in WD pulsar model presented by Rueda *et al.* (2013). The data is from Hulleman *et al.* (2000), Hulleman *et al.* (2004), Morii *et al.* (2005), Dhillon *et al.* (2005), Durant & van Kerkwijk (2006c), Morii *et al.* (2009). The dashed lines are the disk and photosphere components and the bold line is the sum of both components. The observed data are de-reddened ($A_v = 3.5$) and the considered distance was 3.6 kpc. Reference: Rueda *et al.* (2013). 70
- FIGURE 4.1 – —X-ray and UV spectrum produced by two different accretion rates onto a $1M_\odot$ degenerate white dwarf having a magnetic field of $B = 2 \times 10^7$ Gauss. Reference: Lamb & Masters (1979). 73
- FIGURE 4.2 – Accretion column geometry for a magnetized WD. Reference: Frank *et al.* (2002). 74
- FIGURE 4.3 – Log plot of the Gaunt factor as a function of $u = \frac{h\nu}{kT}$. Each curve represents a different value of temperature normalized as $\gamma^2 = \frac{Z^2 Ry}{kT}$, where $Ry=13.6$ eV and Z is the ion charge. The black lines are the non-relativistic g_{ff} and varies from -4 (upper curve) up to 4 (lower curve). The red lines are the relativistic g_{ff} and varies from -3.4 (upper curve) up to -2.3 (lower curve). Reference: Sutherland (1998), Nozawa *et al.* (1998). 76
- FIGURE 4.4 – The density of the flow is smaller upstream and changes abruptly after the shock. The shock wave has thickness of the order of the mean free path of the gas particles. Reference: Frank *et al.* (2002). 78
- FIGURE 4.5 – Post-shock temperature as a function of the WDs mass for different magnetic fields. We consider $\dot{M} = 10^{16}$ g.s $^{-1}$ and $\mu = 0.613$ 80
- FIGURE 4.6 – The black dots from Madej *et al.* (2004) are from DA WDs with carbon nuclei. The red line is the mass radius relation from Nauenberg (1972). 82

- FIGURE 4.7 – Comparison for different mass-radius relations for high-mass WDs. The blue circles marks the maximum mass for each model. The red line represents the mass value for the most massive WD EUVE J1659+440 (Vennes *et al.*, 1997) and the orange strip is the uncertainty for this mass value. SR = special relativity, GR = general relativity. 83
- FIGURE 5.1 – Relation between T_{brem} and χ^2/dof . The black point are the minimum χ^2/dof for each bremsstrahlung temperature and the blue curve is the best fit of those points. 85
- FIGURE 5.2 – *Left panel:* X-rays fit of 4U 0142+61. The dotted lines the blackbody components, the dashed line is the bremsstrahlung component and the bold black line is the total emission. The green and magenta crosses are the same from Fig. 3.7. *Right panel:* Optical/infrared fit of 4U 0142+61 the filled line is the disk component, the dot-dashed line is the blackbody emitted by the WD photosphere, the dashed line is the hard X-rays bremsstrahlung tail and the bold black line is the total emission. The black crosses are the same data from Fig. 3.7 and the red crosses are from Hulleman *et al.* (2000), Hulleman *et al.* (2004). 86
- FIGURE 5.3 – Complete SED of 4U 0142+61 for the WD accreting model. The bold black curve is the complete fit; the filled curve is the disk component; the dot-dashed curve is the WD photosphere; the dotted curves are each one of the hot spots components; and the dashed curve is the bremsstrahlung component. The observational data of 4U 0142+61 is the same from Figure 3.7. 88
- FIGURE 5.4 – Markov chain Monte Carlo distribution of EM for a fixed temperature of 670.3 keV. The blue bars are the histogram distribution of EM and the red line is the best Gaussian. The error in EM is the 1σ Gaussian. 89
- FIGURE 5.5 – Scatter distribution of the soft X-rays fitted parameters T_{spot1} , R_{spot1} , T_{spot2} and R_{spot2} 89
- FIGURE 5.6 – Markov chain Monte Carlo distribution of the soft X-rays fitted parameters T_{spot1} , R_{spot1} , T_{spot2} and R_{spot2} . The blue region are the histogram distribution of each parameter and the red line is the best Gaussian. The error is the 1σ Gaussian 90
- FIGURE 5.7 – Scatter distribution of the optical fitted parameters T_{wd} , T_{in} and T_{out} . 90

FIGURE 5.8 – Markov chain Monte Carlo distribution of the optical fitted parameters T_{wd} , T_{in} and T_{out} . The blue region are the histogram distribution of each parameter and the red line is the best Gaussian. The error is the 1σ Gaussian	91
FIGURE 5.9 – Post-shock structure for a $1.41 M_{\odot}$ WD for 4 different magnetic field strengths. Reference: Belloni (2018).	92
FIGURE 6.1 – Mass distribution histogram for magnetic and non-magnetic WDs. Reference: Kepler <i>et al.</i> (2013).	99
FIGURE 6.2 – Diagram of the final product of the coalesce by the mass of each WD progenitor. Each color in the mass-mass diagram represents the final outcome: HeCO core WD (brown); CO core WD (dark blue); ONe core WD (light blue); massive CO core WD (salmon); neutron star after some time (green); neutron star during the coalescence (yellow); small-mass black hole (red). The shaded area is the region where He detonations can occur. sdB (or sdO) = He-rich hot sub-dwarf of spectral type B (or type O); RCB = R Coronae Borealis stars; SN Ia = supernova Ia; AIC = auto-induced collapse. Reference: Dan <i>et al.</i> (2014)	100
FIGURE 6.3 – Relation between the magnetic field and the effective temperature for isolated WDs. Reference: Ferrario <i>et al.</i> (2015).	105
FIGURE 6.4 – Histogram of the period distribution for a sample of 30 magnetic WDs. Reference: Brinkworth <i>et al.</i> (2013).	107
FIGURE 6.5 – Periodic distribution histogram for magnetic WDs (yellow) and non-magnetic WDs (red). Reference: Kawaler (2015).	107
FIGURE 6.6 – Relation between the magnetic field and the period for magnetic WDs. White DA-type dwarfs are circled, DBs are triangles, and fonts that have already been reported as DA or DB are marked as an inverted triangle. Reference: Brinkworth <i>et al.</i> (2013).	108
FIGURE 6.7 – Relation between mass and period for magnetic WDs. Reference: Brinkworth <i>et al.</i> (2013).	108
FIGURE 6.8 – Relation between age and period for magnetic WDs. Reference: Brinkworth <i>et al.</i> (2013).	108
FIGURE 6.9 – Relation between temperature and period for magnetic WDs. Reference: Brinkworth <i>et al.</i> (2013).	109

-
- FIGURE A.1 – SED of the WD GD 356. The black dots are the observed flux and the dotted line is a blackbody with $T=8000$ K. Reference: Wickramasinghe *et al.* (2010) 132
- FIGURE A.2 – Sensitivity function for the photometric systems Johnson-Cousins and SDSS and its bands. Adapted from Bessell (2005) 134
- FIGURE A.3 – Extinction caused by the dust present in a interstellar cloud. Reference: Carroll & Ostlie (2007). 135

List of Tables

TABLE 1.1 – SGR/AXPs with confirmed optical or infrared counterparts. OPT = optical; NIR = near-infrared; MIR = mid-infrared. Reference: Olausen & Kaspi (2014).	29
TABLE 1.2 – SGR/AXPs properties such as WD pulsars. P = period in s; \dot{P} = period derivative in 10^{-11} s.s $^{-1}$; R = WD radius in 10^8 cm; M = WD mass in M_{\odot} ; B_{min} and B_{max} = minimum and maximum limiting magnetic field in 10^9 and 10^{10} G, respectively. Reference: Coelho (2017)	32
TABLE 1.3 – Properties of similar WDs. References: Beskrovnaya & Ikhsanov (2015), Vennes <i>et al.</i> (2003), Mereghetti <i>et al.</i> (2011).	35
TABLE 2.1 – Position, period, period derivative, observed energy ranges of SGR/AXPs. Reference: Olausen & Kaspi (2014). RA = right ascension, DEC = declination, P = period in s, \dot{P} = period derivative in 10^{-11} s.s $^{-1}$, H = hard X-rays, O = optical/infrared, R = radio, ? = unconfirmed in this energy range.	38
TABLE 2.2 – Optical Johnson magnitudes or limit magnitudes for SGR/AXPs. Some observations were not made in the Johnson photometric system. In this case, the relative band is written along with the magnitude. We only present the higher (less bright) limit. For the observed magnitudes, we present the minimum and maximum observed values for the Johnson bands. Reference: Olausen & Kaspi (2014)	39

TABLE 2.3 –	Near-Infrared magnitudes or limiting magnitudes for SGR/AXPs. Some observations were not made in J, H or K_s bands, specifically. In this case, the relative band is written along with the magnitude. We only present the higher (less bright) limits. For the observed magnitudes, we present the minimum and maximum observed values for the Johnson bands. Reference: Olausen & Kaspi (2014)	40
TABLE 2.4 –	Mid-Infrared fluxes or limiting fluxes for 5 AXPs. The fluxes are presented in μJy . Reference: Olausen & Kaspi (2014).	40
TABLE 2.5 –	Several relations between N_H and A_V	44
TABLE 2.6 –	Values of $R(a)$ for some photometric bands. References: Yuan <i>et al.</i> (2013).	45
TABLE 2.7 –	N_H values for some SGR/AXP using different models. The values in parenthesis are the reduced χ^2 for each model. BB= blackbody, PL= power-law; HPL= high power-law; SPL= soft power-law. . . .	46
TABLE 2.8 –	Extinction in the V band for SGR/AXP. If the reduced χ^2 is the same for both methods, the value outside the parenthesis is for the BB+BB model and the value in the parenthesis is for the BB+PL model.	47
TABLE 2.9 –	Estimated distances for the SGR/AXPs. SMC = Small Magellanic Cloud; LMC = Large Magellanic Cloud; MSC = massive star cluster; SNR = supernova remnant; ? = unconfirmed association. Reference: online version of Olausen & Kaspi (2014).	49
TABLE 2.10 –	Distance estimates for some SGR/AXP using the extinction. The 3D map uses the Galactic reddening 3D map by Green <i>et al.</i> (2018) and the red clump uses the extinction laws in the specific line of sight of the AXPs by Durant & van Kerkwijk (2006b).	51
TABLE 2.11 –	Temperature, radius and luminosity of the soft X-rays considering the BB+PL fit emission of SGR/AXPs. kT = temperature of the blackbody fit in keV, R of the blackbody emission in km; Γ = power-law index; L_x = luminosity in 2-10 keV in erg.s^{-1} , D = distance in kpc.	54

TABLE 2.12 – Temperature, radius and luminosity of the soft X-rays considering the BB+BB fit emission of SGR/AXPs. kT_1 = temperature of the hottest blackbody fit in keV, R_1 = radius of the hottest blackbody fit in km, kT_2 = temperature of the coolest blackbody fit in keV, R_2 = radius of the coolest blackbody fit in km, L_x = luminosity in 2-10 keV in 10^{35} erg.s $^{-1}$, D = distance in kpc.	55
TABLE 2.13 – Soft X-rays pulsed profile of some SGR/AXPs. The column model refers to the model with smaller χ^2 . If the difference between χ^2 for both models is smaller than 0.1, we consider that both models represents equally the data.	56
TABLE 2.14 – Hard X-rays emission properties of SGR/AXP in the 15-60 keV range. The second column shows the energy range of the observations. f_h/f_s is the relation between the hard-tail component and soft component X-ray luminosity. The Cutoff energy was take from Olausen & Kaspi (2014). All other information are from Enoto <i>et al.</i> (2010).	57
TABLE 3.1 – Optical and near-infrared data used in the 4U 0142+61 modelling. The errors in parenthesis represent the zero-point error and were also considered in the fitting procedure.	64
TABLE 5.1 – Parameters of the fitting of 4U 0142+61 in the accreting white dwarf model. The fixed parameters were derived before the fit by independent methods. For the infrared/optical fit all the X-rays parameters are considered fixed, therefore, R_{wd} is not a fitted parameter for this range of energy. The 1σ uncertainties for the last digit for the fitted parameters are between parenthesis.	87
TABLE 5.2 – Luminosity of photosphere	93
TABLE 6.1 – Spectral types of WDs and their respective temperatures. Source:Koester (2013).	105
TABLE A.1 – Johnson-Cousin photometric system. Reference: Léna <i>et al.</i> (1998) .	133
TABLE A.2 – Near-Infrared bands. Reference: Léna <i>et al.</i> (1998)	133
TABLE A.3 – SDSS photometric system. Reference: Fukugita <i>et al.</i> (1996)	134

TABLE B.1 – Estimated magnetic field for SGR/AXP using the BB+BB model. \dot{M} = accretion rate in 10^{16} g.s $^{-1}$; f = fraction of the WD surface occupied by the accretion; R_c = corotational radius in 10^8 cm; B = magnetic field in 10^7 G.	136
TABLE B.2 – Estimated magnetic field for SGR/AXP using the BB+PL model. \dot{M} = accretion rate in 10^{16} g.s $^{-1}$; f = fraction of the WD surface occupied by the accretion; R_c = corotational radius in 10^8 cm; B = magnetic field in 10^7 G.	137

List of Abbreviations and Acronyms

AIC	Auto-induced Collapse
AXP	Anomalous X-Ray Pulsars
CCO	Central Compact Objects
COBE	Cosmic Background Explorer
DIRBE	Diffuse Infrared Background Experiment
GRB	Gamma Ray Bursts
HMXB	High-Mass X-Ray Binaries
INS	Isolated Neutron Star
IRAS	Infrared Astronomical Satellite
LMC	Large Magellanic Cloud
MI	Interstellar Medium
MS	Milliseconds Pulsars
NS	Neutron Star
LMXB	Low-Mass X-Ray Binaries
ROSAT	Röntgensatellit
RRAT	Rotation Radio Transients
SDSS	Sloan Digital Sky Survey
SGR	Soft Gamma Repeaters
SMC	Small Magellanic Cloud
SN	Supernovae
WD	White Dwarf

List of Symbols

A	Extinction
B	magnetic field
d	distance
EM	emission measure
f	fraction of the white-dwarf surface occupied by accretion
g_{ff}	Gaunt factor
H	height of the post-shock region
I	moment of inertia
λ	wavelength
L_x	X-rays Luminosity
\dot{M}	accretion rate
N_H	columnar density of hydrogen
n_e	electrons number density
ω	angular speed
P	spin period
\dot{P}	spin-down
R_{brem}	radius of the post-shock region
R_c	corotational radius
R_M	magnetosphere radius
R_{in}	disk inner radius
R_{out}	disk outer radius
R_{spot}	radius of the soft X-ray spot
M_{WD}	white-dwarf mass
R_{WD}	white-dwarf Radius
T_{brem}	temperature of the hard X-rays emission
T_{in}	disk inner temperature
T_{out}	disk outer temperature
T_{shock}	temperature of the shock
T_{spot}	temperature of the soft X-ray spot
T_{WD}	white-dwarf effective temperature

Contents

1	INTRODUCTION	25
1.1	Degenerate stars	25
1.2	Discovery of SGR/AXPs	26
1.3	Magnetar model	27
1.4	Alternative models	28
1.5	Observational properties of SGR/AXPs	28
1.5.1	Optical and infrared emissions	29
1.5.2	Hard X-ray emission	29
1.6	SGR/AXPs among the NS class	29
1.7	SGR/AXPs among the WD class	30
1.8	A brief overview of 4U 0142+62	33
1.9	Motivation	34
1.10	Aims of the work	35
1.11	Structure of the thesis	36
2	OBSERVATIONAL PROPERTIES OF SGR/AXPs	37
2.1	General properties of SGR/AXP	37
2.2	Optical and Infrared Emission	39
2.3	Interstellar extinction determination	42
2.3.1	Extinction from infrared emission	42
2.3.2	Interstellar X-ray absorption and optical extinction	43
2.3.3	Comparison between the two methods	47
2.4	Estimated distance values	48

2.5	Soft X-rays	53
2.6	Hard X-rays	57
3	4U 0142+61: OBSERVATIONS AND PREVIOUS MODELS	58
3.1	Infrared and optical emission	58
3.1.1	Optical long-term variability	59
3.1.2	Optical periodic variability	60
3.1.3	Polarimetry	61
3.1.4	Presence of emission lines	61
3.2	X-ray emission	61
3.2.1	High-energy periodic variability	62
3.3	Complete SED of 4U 0142+61	64
3.4	Proposed emission models	65
3.4.1	Magnetar model	65
3.4.2	Accreting NS model	66
3.4.3	WD pulsar model	68
4	AN ACCRETION MODEL FOR ISOLATED WHITE DWARFS	71
4.1	Emission mechanisms	72
4.1.1	Post-shock region	75
4.1.2	Blackbody emission	80
4.1.3	Multi-temperature disk	81
4.2	Mass-radius relation	82
5	A MODEL FOR 4U 0142+61	84
5.1	Fitting 4U 0142+61 SED	84
5.1.1	Estimate of errors	86
5.2	Discussions	88
5.2.1	Post-shock region and hot spots	88
5.2.2	White-dwarf photosphere	92
5.2.3	Debris Disk	93

5.2.4	Optical pulsed fraction	94
5.3	Spin-down, propeller regime and the magnetic field	95
6	MERGER OF WHITE DWARFS	98
6.1	Post-merger configuration	100
6.2	Accretion onto the merger remnant	102
6.3	Magnetic isolated WDs	104
6.3.1	Relation between the effective temperature and the magnetic field	105
6.4	Spin period for magnetic isolated WDs	106
6.4.1	Period range for magnetic isolated WDs	106
7	CONCLUSIONS AND FUTURE PATHS	110
	BIBLIOGRAPHY	111
	APPENDIX A – PRINCIPLES OF PHOTOMETRY	127
A.1	Solid Angle	127
A.2	Specific intensity or brightness	128
A.3	Flux	128
A.4	Radiative transfer	129
A.4.1	Emission	129
A.4.2	Absorption	130
A.4.3	Radiative transfer equation	130
A.4.4	Optical depth	131
A.5	Blackbody radiation	132
A.6	Relation between flux and apparent magnitude	133
A.7	Photometric Systems	133
A.7.1	Sensitivity function	134
A.8	Interstellar extinction	135
	APPENDIX B – MAGNETIC FIELD FOR SGR/AXPS IN THE AC- CRETING WD MODEL	136

1 Introduction

This thesis aims to study two X-rays pulsar classes, the Soft Gamma Repeaters (SGR) and the Anomalous X-ray Pulsars (AXP), and specially the object 4U 0142+61. Even though those two classes were initially considered distinct, today it is widely accepted that they have a common phenomenology. Therefore, we treat them as the same class, which we shall succinctly call SGR/AXP. In this context, our purpose is to verify whether the emission of AXP 4U 0142+61 is consistent with an accreting white-dwarf (WD) scenario rather than the most accepted neutron star (NS) origin. We also pursue how this model can be used to explain the emission of other SGR/AXPs. Throughout this introduction, we present an overview about the SGR/AXP class, the current proposed models and the object 4U 0142+61 .

1.1 Degenerate stars

Degenerate stars (NSs and WDs) are extremely dense, usually endpoints of stellar evolution. As stars, they need to compensate the gravitational collapse acting inwards by some outward internal pressure mechanism. Unlike main-sequence stars, that avoid this collapse by the energy released in the fusion of hydrogen, degenerate stars fight against gravity by the pressure of some degenerate Fermi gas. This degenerate gas is formed by electrons, for WDs, or neutrons, for NSs.

The first detected WD was Sirius B. In 1844, Friedrich Bessel was measuring the distance by parallax of Sirius (a.k.a. Sirius A) when he realized the star presents deviations from the straight line, which leads him to conclude that Sirius is, in fact, a binary system rather than a single star. His telescope, however, wasn't good enough to see the companion. Only in 1862, Sirius B was directly observed by Alvan Clark. At that time, new detailed observations showed that Sirius B has a mass of about $1M_{\odot}$ ($1M_{\odot} = 1.98 \times 10^{33}$ g) and is about 1000 times fainter than its companion. For this reason, the scientists of that time guessed that this new star was very cold and red. Conversely, new observations in 1915 showed that Sirius B is, in fact, hotter than Sirius A and emits a good part of its energy in ultraviolet. Due to that new data, the astronomers concluded that the new com-

panion has an extremely small radius for its mass, about $0.008 R_{\odot}$ ($1R_{\odot} = 6,95 \times 10^8$ m), which caused great surprise. We know that the reason WDs have small radii is because their density is about 10^4 greater compared to main-sequence stars. Usually, WDs have a mass close to the Sun (in fact, the average mass of an WD is about $0.6M_{\odot}$) and a radius close to the Earth (about $10^3 - 10^4$ km). Moreover, they are the evolutionary product of low and intermediate mass main-sequence stars, usually below 8 or 9 M_{\odot} (CARROLL; OSTLIE, 2007).

Conversely, NSs are the endpoint evolution of more massive main sequence stars (between 9 and 25 M_{\odot} ; above that mass the product is probably a stellar black hole). They can also be generated by the explosion or collapse of a very massive WD. The existence of NSs were predicted in 1934 by Walter Baade and Fritz Zwicky, two years after the discovery of the neutron particle by James Chadwick. Only in 1967, Jocelyn Bell found the first observational evidence of those stars, by observing the first radio pulsars. NSs have a canonical mass of 1.4 M_{\odot} and radius of about 10 km. Due to its tiny radius, few NSs photosphere were observed till now. They are normally discovered by other emission mechanisms, such as the X-ray release by X-ray Binaries or the radio signal emitted by radio pulsars.

1.2 Discovery of SGR/AXPs

In 1979, the first object of the SGR class, known as SGR 1806-20, was discovered (Mazets *et al.*, 1981). This detection occurred due to a sequence of gamma-ray explosions. Initially, the source SGR 1806-20 was identified as a Gamma Ray Burst (GRB). However, new explosions in 1983 (Laros *et al.*, 1987), which is not expected for GRB sources, transformed SGR 1806-20 into the the first object of a new class, the SGRs.

The first identified AXP was 1E 2259+586 (Fahlman; Gregory, 1981). At the beginning, AXP sources were considered to be X-ray binaries, in which a NS accretes matter from its companion, normally a main-sequence star. However, due to the lack of counterparts for the secondary and the softer X-ray spectrum, these sources were considered different from X-ray binaries. In addition, Koyama *et al.* (1987) showed that the X-ray luminosity was too high to be generated by the energy loss by rotation from a NS, excluding the possibility of those objects to be in other class, the X-ray pulsars. For those reasons, AXPs have also become a new class. Some reviews about the properties and discovery of SGR/AXPs are Mereghetti (2008), Turolla *et al.* (2015) and Kaspi & Beloborodov (2017).

Until today, the emission nature of SGR/AXP is still a reason for debate and several scenarios have been proposed to explain the observed spectra and properties of those objects. The most accepted scenario is the magnetar model.

1.3 Magnetar model

The magnetar model was first proposed by Duncan & Thompson (1992) and Thompson & Duncan (1995), being later developed by several other authors, such as Beloborodov & Thompson (2007), Rea *et al.* (2012) and Beloborodov (2013). In this model, SGR/AXP present a huge magnetic field (B), in the range of $10^{13} - 10^{15}$ G, and the quiescent X-ray emission is caused by the decaying of that field.

Such a magnetic field, however, is not measured directly. Even though the emission comes from a different mechanism, the magnetic field is inferred by the dipole model of pulsars. If the star has a magnetic dipole moment misaligned with the spin axis by an angle α , the energy per second emitted by the magnetic dipole in rotation \dot{E}_{dip} can be written as:

$$\dot{E}_{\text{dip}} = -\frac{2}{3c^3}\mu^2\Omega^4\sin^2\alpha; \quad (1.1)$$

where $\mu = B_d R^3$ is the magnetic moment, c is the speed of light and Ω is the angular velocity. Assuming that the SGR/AXP can be explained as a pulsed rotation-powered, the brightness in X-rays can be expressed as originating from the rotation loss:

$$\dot{E}_{\text{rot}} = -4\pi^2 I \frac{\dot{P}}{P^3}; \quad (1.2)$$

where I is the moment of inertial, P is the spin period and \dot{P} is the spin derivative. Thus, the magnitude field, B_d , is inferred from observational quantities. In this case, R is the radius of the star:

$$B_d = \left(\frac{3c^3 I}{8\pi^2 R^6} P \dot{P} \right)^{1/2}. \quad (1.3)$$

The magnitude required to explain pulsars in the magnetar model is about 10^{14} G, greater than critical value imposed by quantum mechanics ($= 4.4 \times 10^{13}$ G). If the magnetar model is correct, such objects will be responsible for expanding the knowledge about NSs and its evolution (Mereghetti, 2008). Moreover, their magnificent magnetic fields, unseen elsewhere, is a great laboratory for physics.

However, this model present some limitations, such as the difficult to explain the decaying of the low-B (10^{12} G) sources (e.g. SGR 0418+5729) and the hardship to fit the spectra using components with physical meanings, specially for the optical emission. Thus, those obstacles have increased the interest for alternative scenarios in the past few years.

1.4 Alternative models

The most accepted alternative model invokes accreting NSs and was proposed by van Paradijs *et al.* (1995) and Alpar (2001). Moreover, there are models using quark stars (Ouyed *et al.*, 2011) and WD pulsars (Malheiro *et al.*, 2012a; Coelho; Malheiro, 2014).

The accreting NS model states that the X-ray emission is consequence of in-falling gas reaching the isolated NS. The origin of that gas could be the leftover of the common-envelope phase (van Paradijs *et al.*, 1995) or due to some fallback disk formed after the supernova event (Alpar, 2001). The magnetic field is in the range of $10^{12} - 10^{13}$ G.

Quarks stars, theoretical type of degenerate stars, would be possible from the evolution of a NS that have the density of the nucleus increased by accretion or spin-down. In this scenario, the object would have magnetic fields of the order of 10^{15} G (Ouyed *et al.*, 2011), also above the quantum limit.

The last model uses a very massive, rapid and magnetic WD pulsar to explain the emission (Malheiro *et al.*, 2012a; Coelho; Malheiro, 2014). Similar WDs has already been observed in recent years, as can be seen in Ferrario *et al.* (2015). Also, the low-B SGRs exhibit similar properties to the known WD pulsars (Coelho; Malheiro, 2012). WDs have a radii about 10^3 times larger than NSs, thus manifesting a new scale for the moment of inertia, density and rotational energy of these sources. For that reason, this model is capable of predict the luminosity with smaller values of magnetic field, in the range of 10^8 G.

1.5 Observational properties of SGR/AXPs

All SGR/AXPs present a quiescent soft X-ray emission with a 2 – 10 keV luminosity in the range of $10^{29} - 10^{35}$ erg.s⁻¹, period of 2 – 12 s and spin-down of 10^{-15} to 10^{-10} s.s⁻¹. Most SGR/AXP present outburst events, in which the luminosity can reach 10^{43} erg.s⁻¹. Some of them have exhibited giant flares, gigantic eruptions with energy values that can reach 10^{47} erg.s⁻¹. All the 23 confirmed SGR/AXP and 6 candidates are catalogued in Olausen & Kaspi (2014) or in its online version¹, in which it is possible to find several other properties. In this section, we quickly present the most important properties of SGR/AXPs and the relation between them and other NS and WD classes. A thorough overview and some discussions about the observational properties of SGR/AXP are presented in chapter 2.

¹<http://www.physics.mcgill.ca/~pulsar/magnetar/main.html>

1.5.1 Optical and infrared emissions

The infrared and optical emissions are essential to understand the nature of the SGR/AXP, since no emission is expected on those wavelengths coming from an isolated NS. For that reason, the spectrum and pulsed profile in those wavelengths may hold important clues about its emission mechanisms.

It is possible to find optical or infrared counterparts in at least 7 sources (tab. 1.1). Furthermore, there are 5 other objects with suggested counterpart CXOU J010043.1-721134; SGR 1627-41; 1RXS J170849.0-400910; 1E 1841-045 and SGR 1900+14.

TABLE 1.1 – SGR/AXPs with confirmed optical or infrared counterparts. OPT = optical; NIR = near-infrared; MIR = mid-infrared. Reference: Olausen & Kaspi (2014).

Name	OPT	NIR	MIR	OPT Pulsation
4U 0142+61	yes	yes	yes	yes
SGR 0501+4516	yes	yes	-	yes
1E 1048.1-5937	yes	yes	-	yes
1E 1547.0-5408	-	yes	-	-
SGR 1806-20	-	yes	-	-
XTE J1810-197	-	yes	-	-
1E 2259+586	-	yes	yes	-

1.5.2 Hard X-ray emission

The hard X-ray emission for some SGR/AXPs was first presented by Kuiper *et al.* (2006). The discovery of emission in this range of energy also represented a big step towards the understanding of nature of those sources, since all the emission scenarios must present models that predicts the existence of two distinct X-ray components, the soft and hard X-rays. According to Olausen & Kaspi (2014), the 9 sources with hard X-rays are: 4U 0142+61, SGR 0501+4516, 1E 1547.0-5408, 1RXS J170849.0-400910, SGR J1745-2900, SGR 1806-20, 1E 1841-045, SGR 1900+14 and 1E 2259+586.

1.6 SGR/AXPs among the NS class

The different types of NSs can emit due to thermal, rotation-powered or magnetic field origin. All of them can be understood as constituents of the same species, where the evolution of the magnetic field and internal composition are still a mystery. In this way, the study of the different classes is essential to understand the complete picture and evolution of NSs (Harding, 2013).

Rotation-Powered Pulsars, Rotation Radio Transients (RRAT) and milliseconds pulsars (MS) get the energy primarily from rotation. Magnetars emit from the decaying of the magnetic field whereas isolated NSs (INS) release energy due to thermal processes. Central Compact Objects (CCO) are sources of X-rays within supernova remnants. Furthermore, we have the accreting binaries with NSs, such as the High-Mass X-ray Binaries (HMXB) and Low-Mass X-ray Binaries (LMXB).

The magnetic field for each of the classes of NSs is estimated differently. For RPPs, magnetars, INS and CCOs, the magnetic field is calculated from equation presented in section 1.3. For accreting X-ray pulsars, the cyclotron lines along with equation 1.4 give a good estimate of the magnetic field B_{cyc} on the surface, in G, where E_c is the cyclotron line energy.

$$B_{cyc} \sim \left(\frac{E_c}{11.6eV} \right) 10^{12}. \quad (1.4)$$

For LMXB, the estimate of the field B_A , in G, is calculated from equation 1.5 and takes into account that the magnetic pressure is balanced by the pressure generated by the accretion,

$$B_A \sim 10^{12} P_{eq} \left(\frac{\dot{M}}{10^{-9} M_{\odot} yr^{-1}} \right), \quad (1.5)$$

where P_{eq} (in s) is the equilibrium spin period of the NS and \dot{M} is the mass accretion rate. Figure 1.1 shows the distribution of period and magnetic field for some types of NSs and SGR/AXPs such as magnetars. Also, in Figure 1.2, we can see the distribution of the period and spin-down for NSs. It is possible to notice that in both cases magnetars do have similar values and are on the edges of the distribution for NSs.

1.7 SGR/AXPs among the WD class

For the WD pulsar model, the magnitude of the magnetic field for SGR/AXPs is considerably smaller than the magnetar model (Malheiro *et al.*, 2012a, e.g.). The magnetic field is about $10^8 - 10^{10}$ G. The upper limit is larger than magnetic fields of the most magnetic isolate WDs, which varies from 10^3 up to 10^9 G (Ferrario *et al.*, 2015), but sufficiently close to be consistent. Figure 1.3 presents the distribution of period and magnetic field for SGR/AXPs for two models: WD pulsars and magnetar. For the pulsar WD model, the SGR/AXPs have period and magnetic fields compared to other WDs.

Once the WD pulsar model is the most similar model to the proposal of this thesis,

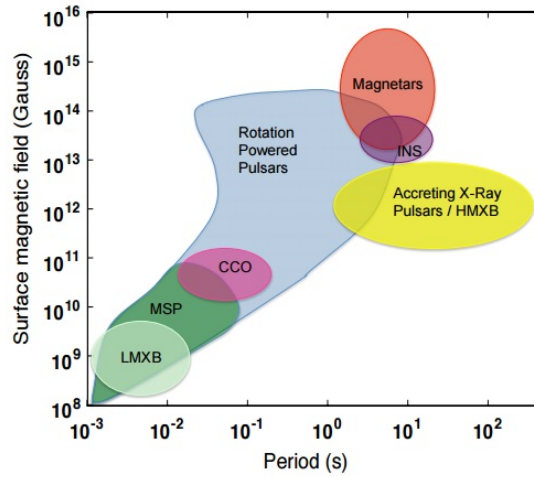


FIGURE 1.1 – Periods and magnetic field magnitude for different classes for NSs. LMXB = Low-Mass X-ray Binaries; CCO = Central Compact Objects; MSP = Milliseconds Pulsars; HMXB = High-Mass X-ray Binaries; INS = Isolated NSs. This section contains a small definition of those classes. Reference: Harding (2013).

it is worth taking a further look in the properties on the SGR/AXPs in this model. In Table 1.2 we can observe some properties of the SGR/AXPs in this scenario. Due to the small period, they need to be massive.

In this work, we study a new WD scenario for those sources. Some properties are similar to the WD pulsar model, such as the high masses required by the small periods. Conversely, the magnetic fields do not need to be the same.

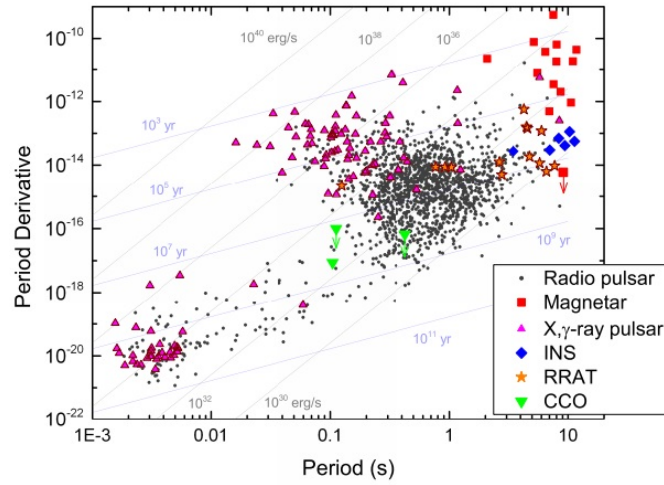


FIGURE 1.2 – Period versus period derivative. RRAT = Rotating Radio Transients. Reference: Harding (2013).

TABLE 1.2 – SGR/AXPs properties such as WD pulsars. P = period in s; \dot{P} = period derivative in $10^{-11} \text{ s.s}^{-1}$; R = WD radius in 10^8 cm ; M = WD mass in M_{\odot} ; B_{min} and B_{max} = minimum and maximum limiting magnetic field in 10^9 and 10^{10} G , respectively. Reference: Coelho (2017)

Name	P	\dot{P}	R_{max}	R_{min}	$M(R_{max})$	$M(R_{min})$	B_{min}	B_{max}
1E 2259	6.98	0.048	4.76	1.04	1.25	1.39	0.182	0.284
SGR 0418	9.08	0.0004	5.53	1.05	1.15	1.39	0.014	0.029
4U 0142	8.69	0.203	5.39	1.05	1.17	1.39	0.316	0.645
J010043.1	8.02	1.88	5.16	1.05	1.20	1.39	1.02	1.89
SGR 0501	5.76	0.582	4.25	1.04	1.30	1.39	0.705	0.903
SGR 0526	8.05	3.80	5.17	1.05	1.20	1.39	1.44	2.69
1E 1048.1	6.46	2.25	4.55	1.04	1.27	1.39	1.30	1.87
1E 1547.0	2.07	4.77	2.24	0.96	1.46	1.39	3.94	1.80
PSR J1622	4.33	1.70	3.58	1.03	1.37	1.39	1.44	1.37
SGR 1627	2.59	1.90	2.59	0.99	1.44	1.39	2.23	1.21
J164710.2	10.61	< 0.04	6.00	1.05	1.08	1.39	< 0.12	< 0.315
J170849.0	11.00	1.91	6.12	1.05	1.07	1.39	0.824	2.22
J171405.7	3.83	6.40	3.32	1.02	1.39	1.39	3.04	2.53
J1745	3.76	0.661	3.28	1.02	1.40	1.39	0.991	0.807
SGR 1806	7.55	49.5	4.98	1.05	1.22	1.39	5.47	9.43
J1810	5.54	0.777	4.16	1.04	1.32	1.39	0.832	1.02
J1822.3	8.44	0.0306	5.31	1.05	1.18	1.39	0.125	0.247
SGR 1833	7.57	0.35	5.00	1.05	1.22	1.39	0.459	0.794
J1834.9	2.48	0.796	2.52	0.98	1.45	1.39	1.47	0.772
1E 1841	11.78	3.93	6.34	1.05	1.04	1.39	1.13	3.29
SGR 1900	5.20	9.2	4.00	1.04	1.33	1.39	2.97	3.43

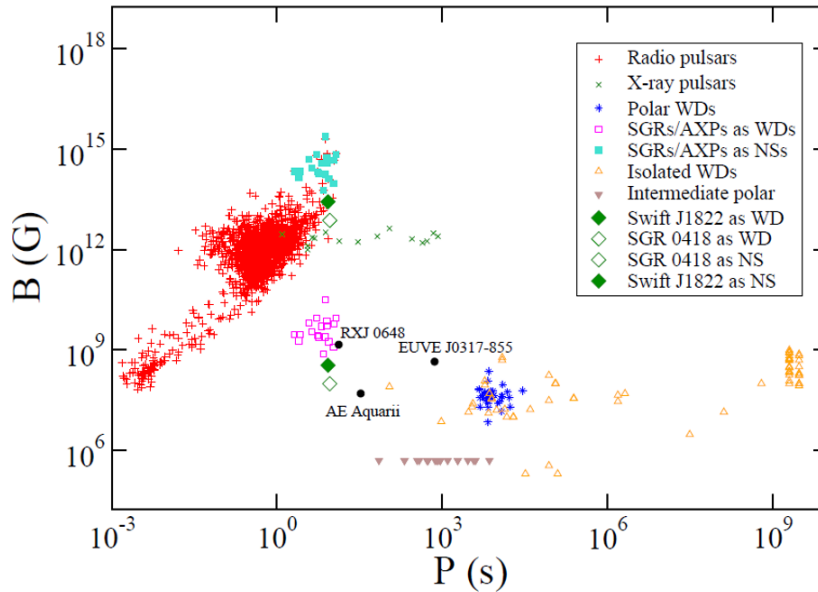


FIGURE 1.3 – Period versus magnetic field for some classes of NSs and WDs. Reference: Malheiro & Coelho (2013)

1.8 A brief overview of 4U 0142+62

4U 0142+61 is an AXP reported for the first time by the UHURU catalogue (Bradt; McClintock, 1983). This object presents quiescent emission in a broad energy range, from mid-infrared (Wang *et al.*, 2006) to hard X-rays (Kuiper *et al.*, 2006), in addition to some gamma-ray outburst events. And, for that reason, it is the most studied SGR/AXP. Its period is 8.68 s and the spin-down is around $2.0 \times 10^{-12} \text{ s.s}^{-1}$ (Olausen; Kaspi, 2014). The luminosity in soft and hard X-rays are estimated as $2.8 \times 10^{35} \text{ erg.s}^{-1}$ and $0.68 \times 10^{35} \text{ erg.s}^{-1}$ (Enoto *et al.*, 2011), respectively.

In the magnetar model, the infrared emission of 4U 0142+61 is interpreted as a passive fallback disk (Wang *et al.*, 2006), the hard and soft X-ray emissions were adjusted by Hascoët *et al.* (2014), using the model proposed by Beloborodov (2013), in which the emission is caused by the production of e^-e^+ pairs close to the NS surface and the soft X-ray emission requires a combination of two modified black bodies, one of those representing the emission of the photosphere and the other one, a hot spot. The optical emission is modelled as a power-law, without physical meaning.

In the accreting NS model, the debris disk is responsible for the infrared and optical emissions (Ertan *et al.*, 2007) and serves as a reservoir of matter for the accretion. The hard X-rays are caused by the accreting structure and the soft X-ray, by a polar cap in the NS surface (Trümper *et al.*, 2013; Zezas *et al.*, 2015). Even though this accreting model succeed to model all the spectral range, the radius of the soft X-rays region is 18 km,

larger than the canonical radius expected for a NS.

In the WD pulsar scenario, the X-ray emission is caused by a pulsar-like emission (Malheiro *et al.*, 2012a) and the optical/infrared data is explained by the presence of the photosphere of the WD and a disk (Rueda *et al.*, 2013). However, the spectra of the soft/hard X-rays is not modelled thus this model is still incomplete. A more careful overview about the properties and the fit of previous models for 4U 0142+61 is presented in the chapter 3.

1.9 Motivation

All the current models fail to explain the emission of 4U 0142+61, as stated in Section 1.8. That problem is not exclusive of 4U 0142+61, since no scenario presents a complete model for the SGR/AXPs class. In addition, the most accepted scenario, the magnetar model, needs huge values of magnetic field for most objects and lacks an explanation the existence of the low-B sources. In this context, the need for improving the current models or proposing new ones is evident.

For that reason, we propose that the persistent emission of 4U 0142+61 comes from an accreting isolated WD surrounded by a debris disk, having gaseous and dusty regions. The optical/infrared emission is consequence of the WD photosphere and the debris disk, the hard X-rays are emitted by the accretion column and the soft X-rays are caused by hot spots in the surface of the WD. This new scenario is inspired by the periodic flux modulation and by the presence of the infrared emission. The presence of disk surrounding isolated NSs is rare. In fact, apart from the SGR/AXP class, in which only 1E 2259+586 and 4U 0142+61 have mid-IR (Kaplan *et al.*, 2009; Wang *et al.*, 2006), only three isolated NSs have detected mid-IR, the radio pulsars Crab, Vela and Geminga (Sandberg; Sollerman, 2009; Danilenko *et al.*, 2011). Thus, mid-IR appears in about 0.3% of all isolated NSs. On the other hand, the presence of mid-IR in white dwarfs is quite common. Debes *et al.* (2011) found that about 7% of all isolated white dwarfs presents an excess of mid-IR detected by *WISE*.

4U 0142+61 is isolated and have a non-confirmed emission feature in $\sim 9 \mu m$, probably due to silicate (Wang *et al.*, 2008). Thus, the mid-IR excess is probably caused by a disk. The presence of disks around isolated NSs are still question for debate. Protoplanetary disk is one possible origin of the planetary system around the NS PSR B1257+12 (Wolszczan; Frail, 1992; Miller; Hamilton, 2001). Also, fallback disks are raised as one possibility to explain the observed break index smaller than 3 (Menou *et al.*, 2001). However, any isolated NS have confirmed debris disk. On the other hand, at least 27% of white dwarfs presents traces of high elements that only can be explained by the accretion of material

in planetary discs (Koester *et al.*, 2014), which reinforces the WD origin for 4U 0142+61.

Moreover, there are known WDs with similar properties, such as those in Table 1.3. EUVE J0317-855, such as the WD in our model, is an isolated, fast and massive WD, probably the product of the merger of two less massive WDs (Ferrario *et al.*, 1997).

TABLE 1.3 – Properties of similar WDs. References: Beskrovnaya & Ikhsanov (2015), Vennes *et al.* (2003), Mereghetti *et al.* (2011).

Name	AE Aquarii	EUVE J0317-855	RXJ 0648.0-4418
Distance (pc)	100	650	27
Radius (km)	7000	3000	3000
Temperature (K)	16000	50000	25000
Period (s)	33.08	725	13.2
Magnetic field (G)	5×10^7	4.5×10^8	1.45×10^9

During this thesis we only model the quiescent emission. Therefore, we do not discuss the responsible mechanism for the glitches and bursts (Gavriil *et al.*, 2011; Dib; Kaspi, 2014; Archibald *et al.*, 2017). There are, however, some clues about their origins in the WD accretion model. For the bursts, the increase in luminosity could be generated by thermonuclear runways of carbon (Gasques *et al.*, 2005). In fact, thermonuclear reaction are seen in some classes of accreting objects, such as in the NS X-ray busters (Ayasli; Joss, 1982; Lewin *et al.*, 1993) and WD Recurrent novae (Webbink *et al.*, 1987; Warner, 2003).

The glitches in SGR/AXPs presents a decrease in the spin/spin-down, which can be joined by a detected increase in the luminosity or not (Dib; Kaspi, 2014). Those glitches could have the same phenomenology of those proposed by the WD pulsar model (Usov, 1994; Malheiro *et al.*, 2012b). In this case, a near-Chandrasekhar WD can present sudden changes in the spin, thereby decreasing the centrifugal forces of the core. Thus, gravity would put the WD in a less oblate shape, which would lead to a change in the gravitational energy and consequent release of energy.

1.10 Aims of the work

The goals of this thesis are:

- to make a detailed survey of the most important properties of SGR/AXPs sources;
- to estimate new distances for some SGR/AXPs;
- to verify if it is possible to fit the entire quiescent spectral energy distribution (SED) of 4U 0142+61 with emission mechanisms consistent with an accretion scenario;

- to estimate the expected magnetic field value 4U 0142+61 using the spin-down and other relevant parameter.

1.11 Structure of the thesis

In Chapter 2, some observational properties of SGR/AXPs are tabulated and discussed. In Chapter 3, we present the most important aspects of the emission of 4U 0142+61 and discuss the proposed models. In Chapter 4, we present the accretion model we use to fit the SED of 4U 0142+61. In Chapter 5, we fit the data of 4U 0142+61 and estimate the strength of the magnetic field based on the spin-down value. In Chapter 6, we discuss the merger scenario and its connection to the class of isolated magnetic WDs. Finally, we present our conclusion and further perspectives in the Chapter 7.

2 Observational properties of SGR/AXPs

In this chapter we present some of the observational properties of SGR/AXPs. We discuss the observed emission of the sources, from infrared to hard X-rays. We also discuss the extinction and distance values. Most of the information and properties were taken from the McGill magnetar catalog (Olausen; Kaspi, 2014) whereas others we found in specific papers about each object.

2.1 General properties of SGR/AXP

In Table 2.1, we present all SGR/AXP along with some of their properties, such as position (right ascension and declination), period and spin-down. We use the right ascension and declination to estimate the extinction and distance. The period derivative and the period are important to estimate the magnetic field. Also, we present the energy ranges in which each object has detected emission. The last 6 objects are candidates whereas the other 23 have already been confirmed.

During the next sections of this chapter we do not consider the candidates in our discussions. Also, only Table 2.1 presents the complete names of the objects: in the following tables, we use only abbreviations of their names.

TABLE 2.1 – Position, period, period derivative, observed energy ranges of SGR/AXPs. Reference: Olausen & Kaspi (2014). RA = right ascension, DEC = declination, P = period in s, \dot{P} = period derivative in 10^{-11} s.s $^{-1}$, H = hard X-rays, O = optical/infrared, R = radio, ? = unconfirmed in this energy range.

Name	RA, DEC (J2000)	P	\dot{P}	Bands
CXOU J010043.1-721134	01h00m43.14s,-72°11'33.8"	8.02	1.88	O?
4U 0142+61	01h46m22.407s,+61°45'03.19"	8.68	0.20	H O
SGR 0418+5729	04h18m33.867s,+57°32'22.91"	9.07	0.0004	-
SGR 0501+4516	05h01m06.76s,+45°16'33.92"	5.76	0.59	H O
SGR 0526-66	05h26m00.89s,-66°04'36.3"	8.05	3.8	-
1E 1048.1-5937	10h50m07.14s,-59°53'21.4"	6.45	2.25	H O
1E 1547.0-5408	15h50m54.124s,-54°18'24.11"	2.07	4.77	H O?R
PSR J1622-4950	16h22m44.89s,-49°50'52.7"	4.32	1.7	R
SGR 1627-41	16h35m51.844s,-47°35'23.31"	2.59	1.9	-
CXOU J164710.2-455216	16h47m10.20s,-45°52'16.90"	10.6	<0.04	-
1RXS J170849.0-400910	17h08m46.87s,-40°08'52.44"	11.0	1.94	H O?
CXOU J171405.7-381031	17h14m05.74s,-38°10'30.9"	3.82	6.4	-
SGR J1745-2900	17h45m40.164s,-29°00'29.82"	3.76	1.38	R
SGR 1806-20	18h08m39.337s,-20°24'39.85"	7.54	49.5	O
XTE J1810-197	18h09m51.087s,-19°43'51.93"	5.54	0.77	O R
Swift J1822.3-1606	18h22m18.00s,-16°04'26.8"	8.43	0.0021	-
SGR 1833-0832	18h33m44.37s,-08°31'07.5"	7.56	0.35	-
Swift J1834.9-0846	18h34m52.118s,-08°45'56.02"	2.48	0.79	-
1E 1841-045	18h41m19.343s,-04°56'11.16"	11.8	4.09	-
3XMM J185246.6+003317	18h52m46.67s,+00°33'17.8"	11.5	<0.014	-
SGR 1900+14	19h07m14.33s,+09°19'20.1"	5.19	9.2	H O?
SGR 1935+2154	19h34m55.598s,+21°53'47.79"	3.24	1.43	-
1E 2259+586	23h01m08.295s,+58°52'44.45"	6.97	0.048	H O
PSR J1846-0258	18h46m24.94s,-02°58'30.1"	0.32	0.7	H
SGR 0755-2933	07h55m42.48s,-29°33'49.2"	-	-	-
SGR 1801-23	18h00m59s,-22°56'48"	-	-	-
SGR 1808-20	18h08m11.2s,-20°38'49"	-	-	-
AX J1818.8-1559	18h18m51.38s,-15°59'22.62"	-	-	-
AX J1845.0 0258	18h44m54.68s,-02°56'53.1"	6.97	-	-
SGR 2013+34	20h13m56.9s,+34°19'48"	-	-	-

2.2 Optical and Infrared Emission

Table 2.2 presents the magnitudes (observed or limits) for the optical bands, which are imperative to understanding the nature of SGR/AXP. Table 2.3 presents the near-infrared magnitudes and limits and Table 2.4 presents the mid-infrared flux and limits for 5 AXPs. Only AXPs 4U 0142+61 and 1E 2259+586 have detected mid-infrared flux.

TABLE 2.2 – Optical Johnson magnitudes or limit magnitudes for SGR/AXPs. Some observations were not made in the Johnson photometric system. In this case, the relative band is written along with the magnitude. We only present the higher (less bright) limit. For the observed magnitudes, we present the minimum and maximum observed values for the Johnson bands. Reference: Olausen & Kaspi (2014)

Name	I	R	V	B	U
CXOU J010043	$F_{814} > 25.9$	-	$F_{606} > 26.2$	$F_{439} > 25.6$	$F_{300} > 24.2$
4U 0142	23.44-23.97	24.89-24.56	25.31-25.62	28.1	$u' > 25.8$
SGR 0418	$i' > 25.1$	$r > 24$	$F_{606} > 28.6$		
SGR 0501	23.3	> 23.0	-	$g' > 26.9$	$u' > 24.7$
SGR 0526	$F_{814} > 26.7$	-	$F_{547} > 26.6$	$F_{380} > 24.7$	$F_{300} > 25.0$
1E 1048.1	24.9-26.2	$r' > 25.6$	> 25.5	> 25.5	> 25.7
1E 1547.0	-	-	> 20.4	> 20.7	> 20.3
1RXS J170849	> 25.1	> 26.3	-	-	-
SGR 1806	-	$Rc > 21.5$	-	-	-
XTE J1810	> 24.30	$Rc > 21.5$	> 22.5	-	-
Swift J1822	$z' > 22.2$	-	-	-	-
SGR 1833	$z' > 24.9$	-	> 21.4	> 21.3	> 22.3
Swift J1834	> 21.6	-	-	-	-
SGR 1900	> 21.0				
SGR 1935	$i' > 24$	$Rc > 21.5$	> 19.8	> 21.1	> 20.6
1E 2259	> 25.6	> 26.4	-	-	-
SGR 2013	> 20.6	> 19	> 20.2	> 21.8	> 21.2

Notes: F_{814} =F814W; F_{606} =F606W; F_{439} =F439W; F_{300} =F300W; F_{547} =F547M; F_{380} =F380W.

TABLE 2.3 – Near-Infrared magnitudes or limiting magnitudes for SGR/AXPs. Some observations were not made in J, H or K_s bands, specifically. In this case, the relative band is written along with the magnitude. We only present the higher (less bright) limits. For the observed magnitudes, we present the minimum and maximum observed values for the Johnson bands. Reference: Olausen & Kaspi (2014)

Name	K_s	H	J
4U 0142	19.83-20.15	20.52-22.18	21.96-22.18
SGR 0418	> 19.6	-	$F_{110W} > 27.4$
SGR 0501	19.2	-	-
1E 1048.1	19.-21.5	$F_{160W}=22.70$	21.7-23.4
1E 1547.0	> 21.7	-	-
PSR J1622	> 20.7	-	-
SGR 1627	> 20.0	> 19.5	> 21.5
CXOU J16470.2	> 20.3	-	-
1RXS J170849.0	> 19.02	> 20.29	> 25.1
SGR 1806	19.32-20.2	> 19.5	> 21.2
XTE J1810	20.81-21.89	21.48-22.55	22.92-23.89
Swift J1822.3	$K > 17.3$	> 18.3	> 19.3
SGR 1833	> 22.4	-	-
Swift J1834.9	> 19.5	-	-
1E 1841	19.6	> 21.54	> 22.1
SGR 1900	$K=19.68$	-	-
SGR 1935	> 15.4	> 16.0	> 16.6
1E 2259	20.41-21.7	-	> 23.8
AX J1845.0	-	> 21	-
SGR 2013	> 18.3	> 18.5	> 19.3

TABLE 2.4 – Mid-Infrared fluxes or limiting fluxes for 5 AXPs. The fluxes are presented in μJy . Reference: Olausen & Kaspi (2014).

Name	$F_{4.5\mu m}$	$F_{8.0\mu m}$	$F_{24\mu m}$
4U 0142	32.1	59.8	< 38
1E 1048.1	< 5.2	< 21.8	< 39
1RXS J170849.0	< 120	< 170	< 590
XTE J1810	< 23	< 130	< 880
1E 2259	6.3	< 20	-

From Tables 2.2, 2.4 and 2.3 we can understand why 4U 0142+61 is the most studied object of the SGR/AXP class. 4U 0142+61 is the only object with detected emission from mid-infrared up to optical. In the optical range, only 4U 0142+61 has detected emission in more than one band, which reinforces its importance among the SGR/AXP class.

Moreover, 4U 0142+61, SGR 0501+4516 and 1E 1048.1-5937, the only three sources with confirmed optical emission, present periodic variability in this energy range. From those objects, we can estimate the pulsed fraction (PF) in a specific band by equation 2.1, where F_{max} and F_{min} represents the maximum and minimum detected flux.

$$PF = \frac{F_{max} - F_{min}}{F_{max} + F_{min}}. \quad (2.1)$$

According to Dhillon *et al.* (2005), the i' band of 4U 0142+61 has 23.7 ± 0.1 mag and pulsed fraction of $58 \pm 16\%$. Figure 2.1 shows the pulsed profile of 4U 0142+61 (Dhillon *et al.*, 2005).

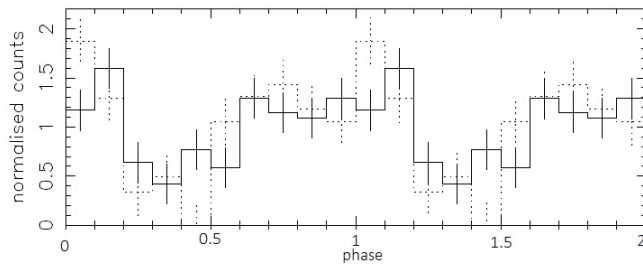


FIGURE 2.1 – Flux variation of 4U 0142+61 on Sep-10-2007 (dotted line) and Sep-12-2007 (solid line) relative to its phase for the i' band. Reference: Dhillon *et al.* (2005)

For SGR 0501+4516, $i' = 24.4 \pm 0.1$ mag and pulsed fraction of $80 \pm 20\%$. The Figure 2.2 shows the pulsed profile for this band.

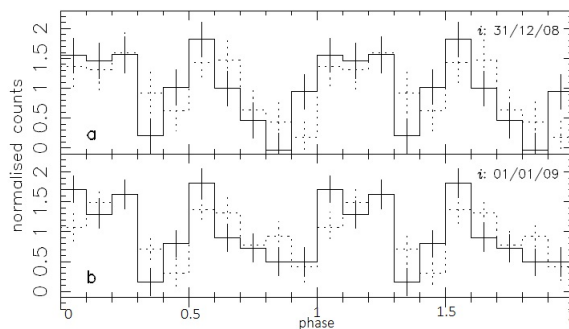


FIGURE 2.2 – Phase diagram of SGR 0501+4516 relative to its phase for the i' band flux. the upper profile is from Dec-31-08 and the bottom profile is from Jan-01-09. The solid and dotted lines represents the same data reduced by two different techniques. Reference: Dhillon *et al.* (2011)

According to Dhillon *et al.* (2009), the i' band of 1E 1048.1-5937 presents 25.3 ± 0.2 mag and pulsed fraction of $52 \pm 15\%$. The pulsed profile is shown in the Figure 2.3.

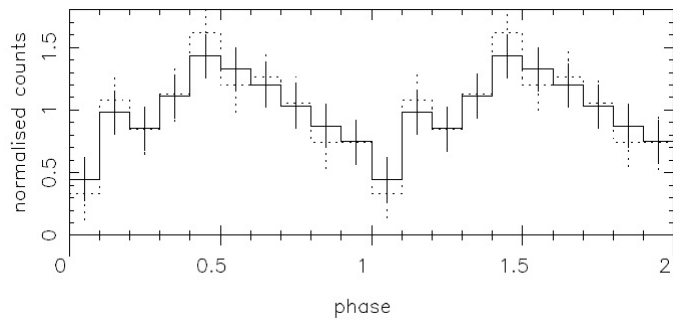


FIGURE 2.3 – Flux variation of 1E 1048.1-5937 from Jun-09-2007 relative to its phase for the i' band. The solid and dotted lines represents the same data reduced by two different techniques. Reference: Dhillon *et al.* (2009)

2.3 Interstellar extinction determination

In this section, we present the two possible methodologies to estimate the extinction of SGR/AXPs. The first method uses the amount of dust in the line of sight of the object to estimate the extinction whereas the second method relates the extinction with the photoelectric absorption. We also compare both methods, discussing the advantages of each.

2.3.1 Extinction from infrared emission

The Galactic extinction calculator, NASA/IPAC (2018), presents the estimates of extinction by two references. In one of them, Schlegel *et al.* (1998), the extinction is calculated from the amount of dust observed in the Galaxy in the far-infrared bands. These results were obtained from the COBE/DIRBE and IRAS/ISSA missions. However, the most recommended value is based on Schlafly & Finkbeiner (2011), which is a calibration of the method presented in Schlegel *et al.* (1998). Schlafly & Finkbeiner (2011) used the data collected in SDSS. The values of temperature, metallicity and gravity were measured using several methods for 500.000 stars. Thus, Schlafly & Finkbeiner (2011) compares the observed spectrum of those stars with the expected value in the absence of extinction.

In both references, the extinction in the Galaxy is integrated along the line of sight and the final result is proportional to the amount of dust. In this case, the further away the object is, the more reliable that extinction value will be.

To estimate $A(\lambda)$ by this method, we use NASA/IPAC (2018) and the coordinates from Table 2.1.

2.3.2 Interstellar X-ray absorption and optical extinction

The absorption of the interstellar medium (IM) in X-rays has a more complex phenomenology than the optical/infrared extinction. Such absorption is caused by the contribution of three components: gas, molecules and grains. The cross section σ_{IM} of the absorption is shown in equation 2.2.

$$\sigma_{IM} = \sigma_{gas} + \sigma_{molecules} + \sigma_{dust}. \quad (2.2)$$

To estimate σ_{IM} we can use the numeric approximation of Morrison & McCammon (1983). The figure 2.4 shows the relation between the cross section and the energy. The absorption is mainly caused by the gas whereas the influence of the grains is small.

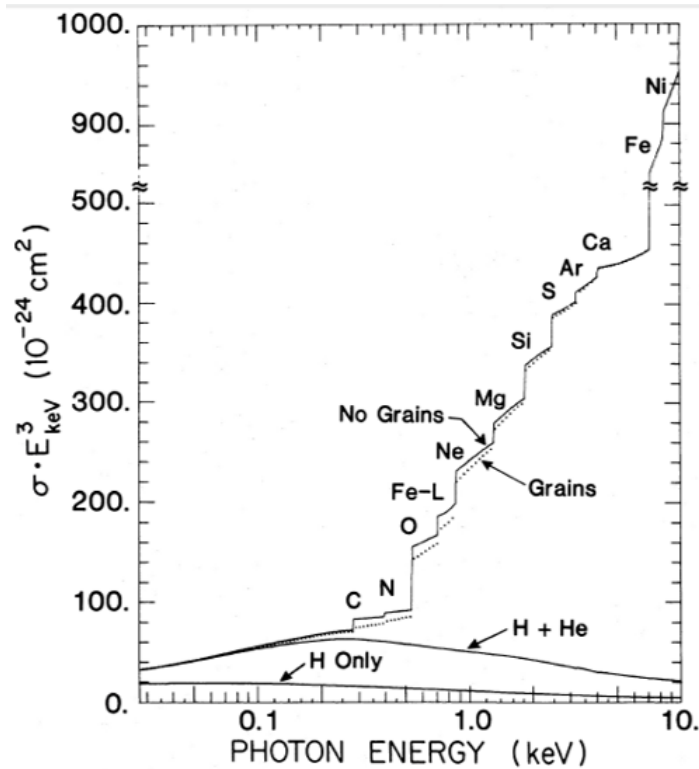


FIGURE 2.4 – Photoelectric absorption cross section as a function of energy. The solid line is for relative abundances with all elements in the gas phase and in neutral atomic form. The dotted line shows the effect of condensing the fraction of each element. The contributions of only hydrogen and only hydrogen + helium to the total cross section are also shown. Reference: Morrison & McCammon (1983).

The observed X-ray spectrum $I(E)$ can be calculated by equation 2.3, where $I_0(E)$ is the spectrum without absorption, N_H is the columnar density of hydrogen and E is the energy value (Wilms *et al.*, 2000).

$$I(E) = I_0(E) \exp(-\sigma_{IM}(E) N_H). \quad (2.3)$$

Also, we can relate the extinction in the optical and infrared bands with the absorption in X-rays. Zhu *et al.* (2017) shows that the relationship between gas and dust masses in the IM is relatively constant. Thus, since the amount of gas in the IM and the value of N_H are closely connected, then the value of A_λ is related to N_H .

Table 2.5 shows the estimate relationship between N_H and A_V by different references. We chose to use Zhu *et al.* (2017) because it is the most recent reference and presents an intermediate value compared to other references.

TABLE 2.5 – Several relations between N_H and A_V

$\frac{N_H}{A_V}$ (10^{21} H.cm $^{-2}$.mag $^{-1}$)	Reference:
2.08 ± 0.02	Zhu <i>et al.</i> (2017)
2.87 ± 0.3	Foight <i>et al.</i> (2016)
2.08 ± 0.30	Valencic & Smith (2015)
2.20 ± 0.4	Watson (2011)
2.21 ± 0.9	Güver & Özel (2009)
1.79 ± 0.03	Predehl & Schmitt (1995)
2.19 ± 0.52	Ryter <i>et al.</i> (1975)
2.22 ± 0.14	Gorenstein (1975)
1.85	Reina & Tarenghi (1973)

To find the value of extinction A in a given band a , we can use equation 2.4 (Schlafly; Finkbeiner, 2011). Note we must know the value of $E(B-V)$ (which is $A(B)-A(V)$).

$$A(a) = R(a) \times E(B - V). \quad (2.4)$$

From Zhu *et al.* (2017) and considering $R(V) = 3.1$, such a value can be calculated from the equation 2.5. In this way, the extinction value depends only on the columnar hydrogen density.

$$N_H = (6.448 \pm 0.062) \times 10^{21} E(B - V). \quad (2.5)$$

The value of R for each band can be found in Table 2.6. The value of $R(a)$ for the infrared and SDSS bands were taken from Yuan *et al.* (2013). For R_v , we consider the standard value of 3.1. $R(a)$ for the Johnson-Cousin bands (except R_V) were taken from the best trinomial fit of the relation between $R(a)$ (SDSS and infrared) and the central wavelength of each band (see. tables A.1, A.2 and A.3 for the central wavelengths).

N_H has a fixed value for each source. However, we usually do not know its value. Thus, N_H is a free parameter in the fit of the X-ray spectra. The X-ray SED is, in most cases, fitted with the sum of empirical models (such as a blackbody and a power-law or two blackbodies) and each sum normally has distinct N_H .

TABLE 2.6 – Values of $R(a)$ for some photometric bands. References: Yuan *et al.* (2013).

Band	R(a)
U	4.23
B	3.59
V	3.1
R	2.01
I	1.26
J	0.72
H	0.46
K_s	0.306
u	4.35
g	3.31
r	2.32
i	1.72
z	1.28

Table 2.7 shows N_H for the two most common empirical models for SGR/AXPs: two blackbodies (BB+BB) and blackbody+power-law (BB+PL) models.

The 4 AXPs presented in the article Durant & van Kerkwijk (2006b) have their interstellar extinction measured in an independent way, using individual absorption edges of metals. Thus, the value of N_H is estimated regardless the empirical model, which we also presented in Table 2.7 in the column named Edges.

TABLE 2.7 – N_H values for some SGR/AXP using different models. The values in parenthesis are the reduced χ^2 for each model. BB= blackbody, PL= power-law; HPL= high power-law; SPL= soft power-law.

Name	BB+BB	BB+PL	Edges	Reference:
CXOU J010043	$0.063_{0.016}^{0.020}$ (1.14)	$0.091_{0.038}^{0.079}$ (1.75)		(1)
4U 0142	0.64 ± 0.01 (1.12) ^a	1.12 ± 0.02 (1.44) ^b	0.64 ± 0.07	(2)(3)
SGR 0418	$0.11_{0.01}^{0.02}$ (1.16) ^c			(4)
SGR 0501		0.88 ± 0.01 (1.15)		(5)
SGR 0526	0.23 ± 0.025 (1.06)	$0.604_{0.059}^{0.058}$ (0.99)		(6)
1E 1048.1	0.14 ± 0.04 (0.96)	0.97 ± 0.01 (1.07)	0.87 ± 0.57	(3)(7)(8)
1E 1547.0		3.46 ± 0.03 (0.97)		(9)
PSR J1622	$5.4_{1.4}^{1.6}$ (0.7) ^d	$10.5_{2.1}^{2.5}$ (0.7) ^e		(10)
SGR 1627	10 (0.58) ^f	10 (0.69) ^g		(11)
CXOU J164710	2.4 (1.18)	2.39 ± 0.05 (0.99)		(12) (13)
1RXS J170849	0.9 ± 0.1 (1.10)	1.42 ± 0.15 (1.00)	1.4 ± 0.4	(3)(14)
CXOU J171405		$3.95_{0.14}^{0.15}$ (1.09) ^h		(15)
SGR 1806	$7.8_{0.9}^{1.2}$ (1.02) ⁱ	$8.0_{1.1}^{2.0}$ (1.02) ^j		(16)
XTE J1810	0.63 ± 0.05 (1.0)	1.05 ± 0.05 (1.0)		(17)
Swift J1822	0.453 (1.07) ^k			(18)
Swift J18234		24^l		(19)
1E 1841	2.34 ± 0.08 (1.12)	$2.54_{0.13}^{0.15}$ (1.11)		(20)
3XMM	1.36 ± 0.05 (1.10) ^m			(21)
SGR 1900	1.82 ± 0.06 (1.32)	2.12 ± 0.08 (1.24)		(22)
SGR 1935		1.6 ± 0.2 (1.02)		(23)
1E 2259	0.568 ± 0.003 (1.11)	1.012 ± 0.007 (1.02)	1.13 ± 0.33	(3)(24)

Notes: a: The BB+BB N_H value is for a 2BB+HPL in the 0.4-70 keV range; b: The BB+PL N_H value is for a BB+SPL+HPL in the 0.4-70 keV range; c: The BB+BB N_H value is for a single BB; d: The BB+BB N_H value is for a single BB; e: The BB+PL N_H is for a single PL; f: The BB+BB N_H value is for a single BB; g: The BB+PL N_H value is for a single PL; h: The BB+PL N_H is for a single PL; i: The BB+BB N_H value is for a 2BB+HPL to fit the soft and hard X-rays; j: The BB+PL N_H is for BB+SPL+HPL to fit the soft and hard X-rays; k: The BB+BB N_H value is for a single BB; l The BB+PL N_H is for a single PL; m: This BB+BB N_H was taken during a post outburst tail;

References: (1) Tiengo *et al.* (2008); (2) Enoto *et al.* (2011); (3) Durant & van Kerkwijk (2006b); (4) Esposito *et al.* (2010); (5) Camero *et al.* (2014); (6) Park *et al.* (2012); (7) Oosterbroek *et al.* (1998); (8) Tam *et al.* (2008); (9) Bernardini *et al.* (2011); (10) Anderson *et al.* (2012); (11) An *et al.* (2012); (12) Rodríguez Castillo *et al.* (2014); (13) An *et al.* (2013); (14) Israel *et al.* (2001); (15) Sato *et al.* (2010); (16) Nakagawa *et al.* (2009); (17) Gotthelf *et al.* (2004); (18) Scholz *et al.* (2012); (19) Younes *et al.* (2012); (20) Morii *et al.* (2003); (21) Zhou *et al.* (2014); (22) Mereghetti *et al.* (2006); (23) Israel *et al.* (2016); (24) Zhu *et al.* (2008);

2.3.3 Comparison between the two methods

The values obtained for each method are not equal since one is integrated across the line of sight and another refers only to the dust between Earth and object. For convenience, we only compare the V-band. The values of extinction using the two methods for the SGR/AXP are presented in Table 2.8. We used the N_H from Table 2.7 for the model with smaller reduced χ^2 .

TABLE 2.8 – Extinction in the V band for SGR/AXP. If the reduced χ^2 is the same for both methods, the value outside the parenthesis is for the BB+BB model and the value in the parenthesis is for the BB+PL model.

Name	from (1)	from (2)	from N_H
CXOU J010043	0.10	0.20	0.30
4U 0142	4.99	5.73	3.07
SGR 0418	2.35	2.92	0.52
SGR 0501	3.55	4.28	4.23
SGR 0526	0.21	0.25	2.90
1E 1048.1	3.88	4.35	0.67
1E 1547.0	44.90	55.44	16.63
PSR J1622	54.13	68.82	25.96 (50.48)
SGR 1627	125.64	152.93	57.69
CXOU J164710	31.756	38.041	11.29
1RXS J170849	55.549	71.656	6.82
CXOU J171405	33.465	36.126	18.99
SGR 1806	50.566	57.709	37.50 (38.46)
XTE J1810	70.489	86.718	3.02 (5.04)
Swift J1822	13.048	13.384	2.17
Swift J18234	111.008	105.008	115.38
3XMM	72.005	65.154	6.138
1E 1841	54.335	65.693	12.21
SGR 1900	11.578	14.144	10.19
1E 2259	3.905	4.564	4.86

References: (1) Schlegel *et al.* (1998); (2) Schlafly & Finkbeiner (2011)

The extinction obtained from X-ray data fitting is smaller for all references, with the exception of CXOU J010043.1-721134, SGR 0526-66, 1E 2259+586 and Swift J1834.9-0846. CXOU J010043.1-721134 is in the Small Magellanic Cloud (SMC) and SGR 0526-66 is in the Large Magellanic Cloud (LMC). Thus, the extinction of those two sources have to account the Galactic extinction in the line of sight and the extinction caused by the SMC and LMC dwarf galaxies, respectively. Once the first method only accounts for the Galactic extinction, it is expect for those sources to have a larger extinction.

For 1E 2259+586, the reason is more blur. Its expected distance is about 3.2 kpc, along with the Supernova Remnant (SNR) CTB 109. For this distance, the expected extinction

the V band is about 2.7 (Green *et al.*, 2018). This extinction value is the same predicted by the BB+BB model, which might be a better representation of the real picture despite the worse reduced χ^2 compared to the BB+PL model. Other possibility is that the presence of the SNR increases the extinction of 1E 2259+586.

For Swift J1834.9-0846, its estimated N_H is 10-100 times larger than N_H for the other sources. There are two possible explanations for this: (i) the model used to fit this sources is incorrect and the value of N_H is overestimated; (ii) the object is surrounded by a dense gas cloud that is not taken into account in the extinction calculator from NASA/IPAC (2018).

The first method from NASA/IPAC (2018) makes an extensive study of the interstellar dust distribution in the Galaxy. However, it presents two main difficulties: (i) it integrates the amount of dust along the entire line of sight, so that the closer the object is, the more overestimated is the extinction; (ii) due to the difficulty of modeling the distribution of dust near the Galactic disk, such method presents unreliable results for Galactic latitude values $b < 5^\circ$ (which is the case for many SGR/AXPs) (NASA/IPAC, 2018).

The second method, which calculates the extinction from the columnar density of hydrogen, presents a unique value for each source since it considers the value of N_H to adjust the spectrum in X-rays. In this way, it does not depend on the distance or position in which the object lies. On the other hand, the value of N_H is closely linked to the chosen emission model. Thus, the extinction calculated from N_H may have no physical meaning if the emission model were incorrect.

Despite its limitations, we chose to use the second method to estimate the extinction, which requires a value of N_H . In this case, the chosen value of N_H will be discussed each time the estimate of extinction were required.

2.4 Estimated distance values

It is common to find distinct distance values for the same source. In Table 2.9, we present the most important distance estimates for all SGR/AXP along with their proposed associations (Olausen; Kaspi, 2014) .

Some sources have extremely uncertain values of distance, such as SGR 0418+5729. van der Horst *et al.* (2010) associated this SGR with the Perseus Arm and estimated a distance of ~ 2 kpc. Thus, such a SGR would be one of the closest and a strongest candidate to have relatively bright optical and infrared counterpart. However, this value is adopted because the object is in the direction of the Perseus arm, so that its distance can be quite different if it was located in a different region but in the same direction.

TABLE 2.9 – Estimated distances for the SGR/AXPs. SMC = Small Magellanic Cloud; LMC = Large Magellanic Cloud; MSC = massive star cluster; SNR = supernova remnant; ? = unconfirmed association. Reference: online version of Olausen & Kaspi (2014).

Name	Distance (kpc)	Association
CXOU J010043	62.4 ± 1.4	SMC
4U 0142	3.6 ± 0.4	-
SGR 0418	~ 2	Perseus Arm
SGR 0501	~ 2	Perseus Arm; SNR HB 9 ?
SGR 0526	53.6 ± 1.2	LMC
1E 1048.1	$2.7 \pm 1.0 / 9.0 \pm 1.7$	GSH 288.3-0.5-28?
1E 1547.0	9 / 4-5	SNR G327.24-0.13
PSR J1622	~ 9	SNR G333.9+0.0
SGR 1627	5.8 / 11.0 ± 0.3	SNR G337.0-0.1
CXOU J164710	2-5.5 / $5_{1.0}^{0.5} / 3.9 \pm 0.7$	Westerlund 1 (MSC)
1RXS J170849	3.8 ± 0.5	-
CXOU J171405	$10.2 \pm 3.5 / 7 \pm 2 / 13.2$	SNR CTB 37B
SGR J1745	8.3 ± 0.3	Galactic Center
SGR 1806	$15.1_{1.3}^{1.8} / 6.4-9.8 / 8.7_{1.5}^{1.8} / 9.4-18.6$	MSC
XTE J1810	3.3 / $3.1 \pm 0.5 / 3.1-4$	-
Swift J1822	1.6 ± 0.3	M17 (HII region)
Swift J1834	4.2 ± 0.3	SNR W41
3XMM J185246	~ 7.1	-
1E 1841	$8.5_{1.0}^{1.5}$	SNR Kes 73
SGR 1900	12-15 / 12.5 ± 1.7	MSC
1E 2259	$7.5 \pm 1.0 / 4.0 \pm 0.8 / 3.2 \pm 0.2$	SNR CTB 109

Most objects have their distance by the association with other object with known distance, such as a SNR. Other objects have radio emission and estimated distance from the dispersion measure, such as the AXP 1E 1547.0-5408 (Camilo *et al.*, 2007). However, some objects do not have neither any proposed association nor radio emission. For those cases, there are other methods to estimate the distance using the optical extinction.

For instance, Durant & van Kerkwijk (2006a) surveyed the distribution of red clump, an Helium burning giant, along the line of sight for some AXPs. All the red clump stars present the same intrinsic color and magnitude. Figure 2.5 shows the color-magnitude diagram for two different lines of sight. Red clumps are the stars in the red strip. If all of the red clumps stars were in the same distance with the same extinction they would be almost at the same point. If the distance were different and without any extinction effect, they would move only in the y-axis whereas if their extinction were different but the distance were the same, they would move in both axis. If we search how the strips moved in the color-magnitude diagram we get a good relation of how extinction varies along the distance, for an specific direction. Thus, knowing the estimated value of extinction for the SGR/AXPs, it is possible to estimate their distances.

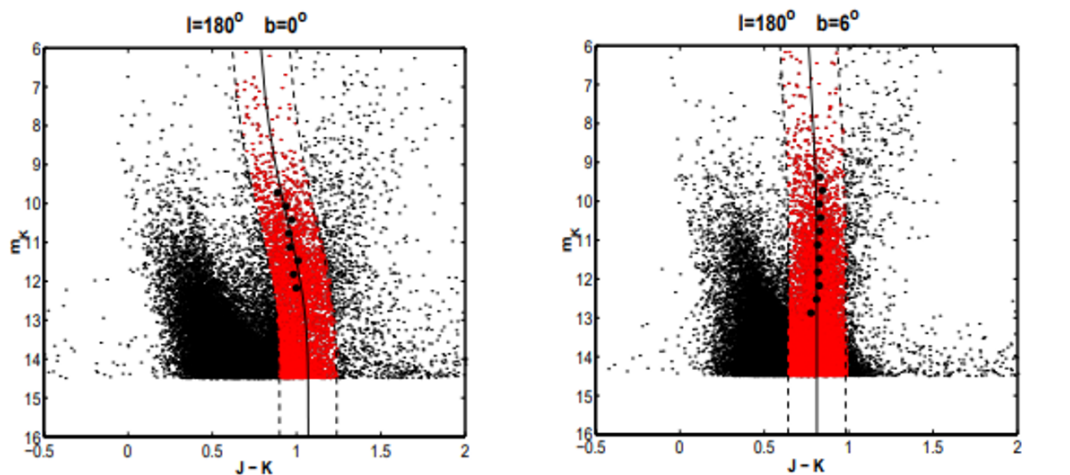


FIGURE 2.5 – Color-magnitude diagrams for two lines of sight for Galactic coordinates. Extinction causes a slight broadening in the K-giants strip for in-plane regions. The black dots is the position of the red clumps. The solid line shows the best fitted trace. The dashed lines show the limits for the red clump giants extraction within a width of 0.4 mag. Reference: : López-Corredoira *et al.* (2002).

Using a similar methodology it is possible to create 3D extinction maps. For instance, the Galactic reddening 3D map (Green *et al.*, 2018), which has an online¹ distance calculator, uses the photometry of 800 million stars (hundreds per line of sight) to estimate their spectral types and distance. This 3D map of extinction covers 75 % of the sky and presents good agreement with the 2D extinction map of Schlafly & Finkbeiner (2011) for the region with $b \neq 0^\circ$. We were able to apply this method for 8 SGR/AXPs. We excluded the SGR/AXPs lying in the Galactic plane ($|b| \leq 0.1^\circ$) in order to guarantee that the 3D and 2D extinction maps are the same and, therefore, the extinction law in a specific direction is confirmed by two different methods.

Furthermore, 3 AXP that are not covered by the 3D reddening map have an estimated distance- A_v relation estimated by the red clumps star model (Durant; van Kerkwijk, 2006a). Thus, we can also estimate the distance for those 3 AXP using the values of N_H for the BB+BB, BB+PL models. Moreover, we considered the N_H/A_V relation by Zhu *et al.* (2017) to estimate A_v whereas Durant & van Kerkwijk (2006a) considered the relation from Predehl & Schmitt (1995) (see Tab. 2.5). This way, even if we consider the same N_H , our estimated distance will be smaller than the presented by Durant & van Kerkwijk (2006a).

The error bars for the 3D map takes into account only the error in the extinction-distance relation, once its error is always greater or equal to the error associated with $E(B-V)$. For the red clumps method, we consider the same methodology of Durant & van Kerkwijk (2006b) to estimate the error bars. Discussions about the new estimates of

¹<http://argonaut.skymaps.info/>

TABLE 2.10 – Distance estimates for some SGR/AXP using the extinction. The 3D map uses the Galactic reddening 3D map by Green *et al.* (2018) and the red clump uses the extinction laws in the specific line of sight of the AXPs by Durant & van Kerkwijk (2006b).

Name	BB+BB	BB+PL	Edges	Method
4U 0142	$2.57_{0.59}^{0.30}$	$11.96_{4.69}^{\infty}$	$2.57_{0.59}^{0.30}$	3D map
SGR 0418	$0.22_{0.08}^{0.02}$	-	-	3D map
SGR 0501	-	≥ 4	-	3D map
Swift J1822.3	1.76 ± 0.02	-	-	3D map
SGR 1900	$6.79_{0.08}^{0.06}$	7.27 ± 0.07	-	3D map
SGR 1935	-	$7.38_{0.45}^{1.13}$	-	3D map
1E 2259	$3.11_{0.04}^{0.43}$	∞	∞	3D map
1E 1048	≤ 2.4	8.6 ± 1.6	8.35 ± 1.4	Red Clumps
1RXS J170849	2.3 ± 0.3	3.8 ± 0.5	3.8 ± 0.5	Red Clumps
1E 1841	≥ 5	≥ 5	≥ 5	Red Clumps

distance for the SGR/AXPs are given below.

For 4U 0142+61, we find a distance of $2.57_{0.59}^{0.30}$ kpc for both the BB+BB and edge N_H values and $11.96_{4.69}^{\infty}$ kpc for the BB+PL. 4U 0142+61 has not any claim of association. Even though the BB+BB has the small χ^2 and agrees with the estimate from the edge for metals, we cannot point a preferable model based on the distance of some known association.

Since the discovery of SGR 0418+5729, this SGR was thought to be in the Perseus Arm, with a estimate distance of 2 kpc (van der Horst *et al.*, 2010). SGR 0418+5729 also is a low-B source in the magnetar paradigm. This low-B SGR is consider a magnetar for two main reason: (i) the emission of SGR-like bursts; (ii) L_x greater than the loss of rotational energy. The loss of rotational energy (\dot{E}_{rot} , in erg.s^{-1}) for a neutron star can be described by the equation 2.6, considering $I = 10^{45} \text{ g.s}^{-1}$ (Malheiro *et al.*, 2012b). For a regular rotation powered NS, we must have $\dot{E}_{rot} > L_x$. For SGR/AXPs, we observe the opposite. For SGR 0418+5729 we have $\dot{E}_{rot} = 2.11 \times 10^{29} \text{ erg.s}^{-1}$. For 2 kpc, L_x in 2-10 keV is $9 \times 10^{29} \text{ erg.s}^{-1}$. Therefore, $\dot{E}_{rot} < L_x$ for 2 kpc.

$$\dot{E}_{rot} = -3.95 \times 10^{46} \frac{\dot{P}}{P^3}. \quad (2.6)$$

However, for a distance 10 times smaller, the value of L_x decreases 100 times. In this way, the new value of L_x in the same range is $\sim 9 \times 10^{27} \text{ erg.s}^{-1}$. For this new estimate, we have $\dot{E}_{rot} > L_x$. Thus, except for the SGR-like burst, this SGR could be explained by a regular rotation powered model.

Moreover, SGR 0418+5729 is the closest and less extinguished SGR/AXP and has no optical/infrared counterpart. The magnitude limits for SGR 0418+5729 and this new

estimate of distance exclude any possibility of a WD model for this object.

SGR 0501+4516 was also thought to be at the Perseus arm, with a estimated distance of 2 kpc (Lin *et al.*, 2011). However, according to the 3D extinction map of Green *et al.* (2018), the extinction of this SGR agrees with a distance greater than 4 kpc. Thus, we consider a distance of 4 kpc for any further analysis of SGR 0501+4516 in this thesis, even though this is only a inferior limit.

Swift J1822.3-1606 has a estimate distance of 1.76 ± 0.02 kpc using the N_H for single BB model. This values agrees with the prior estimate of 1.6 ± 0.3 kpc due to the association with the HII region M17 (Scholz *et al.*, 2012).

For SGR 1900+14, we have two distance estimate, each one for a different model. The values are $6.79_{0.08}^{0.06}$, for the BB+BB model, and 7.27 ± 0.07 , for the BB+PL model. Both of them do not agree with the prior estimate of 12.5 ± 1.7 based on the distance of the massive star cluster thought to be associated with this SGR (Davies *et al.*, 2009). Moreover, the difference of those estimates is not irrelevant. Thus, based on this new analysis, it very unlikely that SGR 1900+14 is associated with this star cluster.

SGR 1935+2154 is thought to be associated with SNR G57.2+0.8, which has an expected distance of 9.1 kpc (Pavlović *et al.*, 2013). Moreover, Surnis *et al.* (2016) uses the HII spectra to estimate a distance of 11.7 ± 2.8 kpc. The estimate $7.38_{0.45}^{1.13}$ kpc is smaller than of the two prior estimates but sufficiently close. Thus, considering all estimates the best distance is about 8.5 kpc.

1E 2259+586 is associated with the SNR CTB 109, which has an estimate distance of 3.2 ± 0.2 kpc (Kothes; Foster, 2012). This distance agrees with the estimate for the BB+BB model of $3.11_{0.04}^{0.43}$. For the BB+PL N_H , the 3D map cannot estimate the distance once the total Galactic extinction in this line of sight is smaller than the predicted value. Thus, even though the edge N_H agrees better with BB+PL model, the distance estimate points out to the BB+BB model.

1E 1048.1-5937 have not its line of sight mapped by Green *et al.* (2018). We use the relation between distance and A_v from Durant & van Kerkwijk (2006a) to estimate the distance from the BB+BB model. 1E 1048.1-5937 has two previous and distinct distance estimates. Gaensler *et al.* (2005) associates this AXP with the stellar wind bubble GSH 288.3-0.5-28, which has a distance of 2.7 ± 1.0 kpc. This distance agrees with the upper limit for the BB+BB model. However, for the BB+PL N_H , the distance is 8.6 ± 1.6 kpc. Thus, if the association if the wind bubble were confirmed the BB+BB would be more likely.

1RXS J170849.0-400910 do not have any proposed association and do not have its line of sight mapped by Green *et al.* (2018). We use the relation between distance and A_v from Durant & van Kerkwijk (2006a) to estimate the distance of 2.3 ± 0.3 kpc for the BB+BB

model. It is important to highlight that the BB+PL has a smaller χ^2 . Thus, the BB+PL model is more likely to be correct, which leads the estimate distance of 3.8 ± 0.5 kpc.

At last, the AXP 1E 1841-045 do not have its line of sight mapped by Green *et al.* (2018) and only have a inferior limit of 5 kpc from the the relation between distance and A_v from Durant & van Kerkwijk (2006a). However, this AXP has association with a SNR of estimate distance of $8.5_{1.0}^{1.5}$ kpc, which is consistent with the derived inferior limit for both models.

2.5 Soft X-rays

Excluding a few candidates, all SGR/AXPs have soft X-rays emission. Thus, to understand and present some of the most important characteristics of the energy range is essential. The following Tables shows the compiled information about the temperature of the emission, radius of the emitting region, luminosity and pulsed fraction. We compile those parameters for the two most studied models (BB+BB and BB+PL) separately. In appendix B, we use the soft X-rays properties from Tables 2.11 and 2.12 to estimate the magnetic field for SGR/AXPs.

At last, Table 2.13 presents the soft X-rays pulsed fraction of SGR/AXPs. The pulsed fraction is estimated by equation 2.1.

For Table 2.13 the average pulsed fraction of SGR/AXPs is about 33%. For the objects with only one peak, this value is about 43% and for those with two peaks, this value is about 22%. In this analysis, we consider that 1RXS J170849.0-400910 has two peaks. Also, we can observe that sources with 1 peak have a smaller χ^2 for 1PL or PL+BB models (with the exception of 1E 1048.1-5937). Conversely, the objects with two peaks have a smaller χ^2 for 1BB or BB+BB models (with the exception of SGR 0501+4516).

TABLE 2.11 – Temperature, radius and luminosity of the soft X-rays considering the BB+PL fit emission of SGR/AXPs. kT = temperature of the blackbody fit in keV, R of the blackbody emission in km; Γ = power-law index; L_x = luminosity in 2-10 keV in erg.s^{-1} , D = distance in kpc.

Name	kT	R	Γ	L_x	D	Reference:
CXOU J0100	0.34	9.67	2	6.69	62.4	(1)
4U 0142	0.41	17.54	4.0	134.41	11.96	(2)
SGR 0501	0.50	0.624	3.84	0.396	4	(3)
SGR 0526	0.44	6.432	2.5	28.05	53.6	(4)
1E 1048.1	0.56	1.79	3.14	4.51	8.6	(5)
1E 1547.0	0.43	0.7	4.0	0.13	4.5	(6)
PSR J1622	-	-	5.4	35.4	9	(7)
SGR 1647	0.5	1.2	0.6	1.14	11	(8)
CXOU J164710.2	0.59	0.14	3.86	0.045	3.9	(9)
1RXS J170849.0	0.46	3.04	2.62	20.82	3.8	(10)
CXOU J171405.7	-	-	3.45	5.6	13.2	(11)
SGR 1806	0.55	5.39	1.6	16.3	8.7	(12)
1E 1841	0.44	6.67	2	21.94	8.7	(13)
SGR 1900	0.47	1.94	1.9	3.03	7.27	(14)
SGR 1935	0.48	1.31	2.1	1.61	7.38	(15)
1E 2259	0.37	3.58	3.75	1.73	3.2	(16)

References: (1) Tiengo *et al.* (2008); (2) Rea *et al.* (2007); (3) Camero *et al.* (2014); (4) Park *et al.* (2012); (5) Tam *et al.* (2008); (6) Bernardini *et al.* (2011); (7) Anderson *et al.* (2012); (8) Esposito *et al.* (2009); (9) An *et al.* (2013); (10) Israel *et al.* (2001); (12) Olausen & Kaspi (2014); (13) Morii *et al.* (2003); (14) Mereghetti *et al.* (2006); (15) Israel *et al.* (2016); (16) Zhu *et al.* (2008);

TABLE 2.12 – Temperature, radius and luminosity of the soft X-rays considering the BB+BB fit emission of SGR/AXPs. kT_1 = temperature of the hottest blackbody fit in keV, R_1 = radius of the hottest blackbody fit in km, kT_2 = temperature of the coolest blackbody fit in keV, R_2 = radius of the coolest blackbody fit in km, L_x = luminosity in 2-10 keV in 10^{35} erg.s $^{-1}$, D = distance in kpc.

Name	kT_1	R_1	kT_2	R_2	L_x	D	Reference:
CXOU J010043.1	0.68	1.77	0.3	12.58	6.92	62.4	(1)
4U 0142	0.63	1.64	0.337	9.42	5.29	2.57	(2)
SGR 0418	0.32	0.0088	-	-	1.27×10^{-6}	0.22	(3)
SGR 0526	1.01	1.07	0.39	10.40	20.03	53.6	(4)
1E 1048.1	1.25	0.08	0.58	0.62	0.46	2.4	(5)
PSR J1622	0.5	0.37	-	-	0.11	9	(6)
SGR 1627	0.85	0.24	-	-	0.30	11	(7)
1RXS J170849.0	1.54	0.14	0.5	2.11	2.64	2.4	(8)
SGR 1806	2.7	0.06	0.54	3.1	6.17	8.7	(9)
Swift J1822.3	0.12	5.5	-	-	4.06×10^{-6}	1.76	(11)
1E 1841	1.5	0.44	0.47	6.92	20.73	8.7	(12)
SGR 1900	1.9	0.10	0.53	1.67	2.54	6.79	(13)
1E 2259	0.77	0.51	0.362	4.45	1.46	3.11	(14)

References: (1) Tiengo *et al.* (2008); (2) Enoto *et al.* (2011); (3) Rea *et al.* (2013); (4) Park *et al.* (2012); (5) Oosterbroek *et al.* (1998); (6) Anderson *et al.* (2012); (7) An *et al.* (2012); (8) Israel *et al.* (2001); (9) Nakagawa *et al.* (2009); (10) Scholz *et al.* (2012); (11) Morii *et al.* (2003); (12) Mereghetti *et al.* (2006); (13) Zhu *et al.* (2008);

TABLE 2.13 – Soft X-rays pulsed profile of some SGR/AXPs. The column model refers to the model with smaller χ^2 . If the difference between χ^2 for both models is smaller than 0.1, we consider that both models represents equally the data.

Nome	Pulsed Fraction	Energy	Peaks	Model	Reference:
CXOU J0100	$32 \pm 3\%$	0.2-6	2	2BB	(1)
4U 0142	$9.6 \pm 2.0\%$	2.5-10	2	2BB	(2)
SGR 0418	$29\% \pm 3\%$ (rms)	2.5-10	2	1BB	(3)
SGR 0501	$45 \pm 6\%$	0.3-12	2	BB+PL	(4)
SGR 0526	$13.6\% \pm 0.9\%$	0.65-12	2	Both	(5)
1E 1048	$54 \pm 12\%$	6-10	1	2BB	(6)
1E 1547	$12 \pm 1\%$ (rms) / $< 14\%$	2-10	1	BB+PL	(7) (8)
SGR 1627	$24 \pm 3\%$	2-12	2	1BB/1PL	(9)
CXOU J1647	$97 \pm 5\%$	0.5-4	1	BB+PL	(10)
1RXS J1708	$30-40\%^a$	0.3-10	1-2 ^b	Both	(11)
CXOU J17145	$\sim 31\%$	1-10	1	BB+PL	(12)
SGR 1806	$8 \pm 2\%$	0.2-12	1	Both	(13)
XTE J1810	$34 \pm 2\%$	1.5-5	1	Both	(14)
Swift J1822	$48 \pm 8\%$ (3)	2-10	2	1BB	(15)
Swift J1834	$60\% \pm 15\%$	2-10	1	1PL	(16)
1E 1841	$18.9 \pm 2.6\%$	0.6-7	2	Both	(17)
SGR 1900	$16.7 \pm 0.5\%$	0.8-10	1	Both	(18)
1E 2259	$23 \pm 5\%$ (rms)	2-10	2	Both	(19)

Notes: a: from $\sim 40\%$ for 0.3 keV to $\sim 30\%$ for 10 keV b: 1 peak for the range 0.3-6 keV and 2 peaks for the range 6-10 keV; (1) Tiengo *et al.* (2008); (2) Göhler *et al.* (2005); (3) Esposito *et al.* (2010); (4) Camero *et al.* (2014); (5) Tiengo *et al.* (2009); (6) Oosterbroek *et al.* (1998); (7) Bernardini *et al.* (2011); (8) Gelfand & Gaensler (2007); (9) Esposito *et al.* (2009); (10) Rodríguez Castillo *et al.* (2014); (11) Israel *et al.* (2001); (12) Sato *et al.* (2010); (13) Nakagawa *et al.* (2009); (14) Alford & Halpern (2016); (15) Scholz *et al.* (2012); (16) Younes *et al.* (2012); (17) Morii *et al.* (2003); (18) Mereghetti *et al.* (2006); (19) Zhu *et al.* (2008).

2.6 Hard X-rays

The first hard X-ray emission from SGR/AXPs was discovered by Kuiper *et al.* (2006). For those sources it is widely accepted that the range of hard X-rays emission is from 10 up to a few hundred keV. Below 10 keV, we consider the emission as soft X-rays.

The hard component is not just the tail of the soft X-rays, but a new component. That way, the proposed models must present two different high energy emission components. In Table 2.14, we present some properties of that emission for the objects that present hard X-rays emission.

TABLE 2.14 – Hard X-rays emission properties of SGR/AXP in the 15-60 keV range. The second column shows the energy range of the observations. f_h/f_s is the relation between the hard-tail component and soft component X-ray luminosity. The Cutoff energy was take from Olausen & Kaspi (2014). All other information are from Enoto *et al.* (2010).

Name	Cutoff	f_h/f_s	model
4U 0142	279^{+65}_{-41}	0.20 ± 0.04	A
SGR 0501	> 100	$0.58^{0.15}_{0.13}$	B
1E 1547.0	> 200	2.8 ± 0.1	C
1RXS J170849.0	> 300	$0.48^{0.08}_{0.07}$	A
SGR 1806	> 160	$9.1^{2.1}_{1.3}$	C
1E 1841	> 140	$1.44^{0.05}_{0.04}$	A
SGR 1900	> 100	$2.5^{0.6}_{0.5}$	C
1E 2259	-	< 0.2	A

Notes: A: Comptonized blackbody plus high power-law; B: blackbody and the Comptonized blackbody plus high power-law; C: blackbody plus high power-law;

In Table 2.14, the cutoff is the energy from which the object is not observed anymore. f_h/f_s is the ratio between the hard and soft components for the models in the last column.

The fluxes in Table 2.14 are not standardized for the same model, such as we did for the soft X-rays. Therefore, we must compare them with caution. For instance, the ratio between the hard and soft fluxes can vary if we consider different models from those presented in Table 2.14. We can, however, observe that the ratio between those two fluxes is, at most, one order of magnitude different from 1 for all sources.

In this way, the hard X-ray and soft X-ray fluxes are similar and, therefore, the emission mechanisms for those two energy ranges are probably different but connected. If we consider an accretion paradigm, the values of the hard and soft X-ray being in the same order of magnitude are easily explained. In section 4.1, we discuss more thoroughly the relation between the hard and soft emission.

3 4U 0142+61: observations and previous models

In this chapter, we present a complete overview of the observations of 4U 0142+61 . We discuss the set of data we chose to build the complete SED of 4U 0142+61. We also present the most important derived properties of 4U 0142+61 in previous models.

3.1 Infrared and optical emission

The near-infrared (NIR) K-band flux was measured for the first time in 1999 using the Keck telescope by Hulleman *et al.* (2004). After that, several NIR observations were performed. Even though most of them are in the K band, data in J, H bands have been taken using CFHT, Subaru and Gemini. Meanwhile, the mid-infrared (MIR) Spitzer in 4.5 and 8.0 μm was measured by Wang *et al.* (2006).

The optical emission of 4U 0142+61 was discovered by Hulleman *et al.* (2000), and complementary observations were performed by Hulleman *et al.* (2004), Dhillon *et al.* (2005), Morii *et al.* (2005) and Muñoz-Darias *et al.* (2016), who also present the first optical spectra of 4U 0142+61. All of these optical data are displayed in Figure 3.1.

Based on previous optical measurements (Hulleman *et al.*, 2000; Hulleman *et al.*, 2004, e.g), Durant & van Kerkwijk (2006c) and Wang *et al.* (2006) pointed out that the optical and infrared emissions seemed no to be connected and, therefore, they probably were caused by distinct emission components. However, the new set of data from Muñoz-Darias *et al.* (2016) fits smoothly with the infrared emission (see Fig. 3.1), demystifying the need for different emission origins.

To estimate $F_E d_E$ we proceed as follows. From equation A.5, we can get the relation $F_E d_E = F_\lambda d_\lambda$. Thus, we only need to estimate F_λ . The flux F_λ were calculate by using the magnitudes and equation A.25. The zero-flux magnitude e_0 were taken from Tables A.1, A.2 and A.3, depending on the photometric system. After that, we multiply F_λ by the central wavelength (λ_0) of each band (also taken from Tables A.1, A.2 and A.3), getting

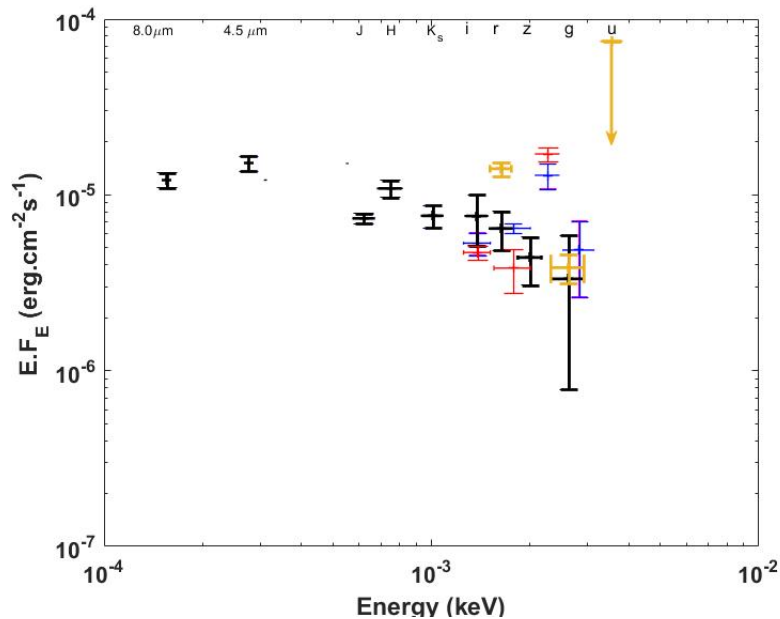


FIGURE 3.1 – Optical and infrared SED of 4U 0142+61 . The black crosses are from Wang *et al.* (2006, mid-infrared), Durant & van Kerkwijk (2006c, Gemini near-infrared) and Muñoz-Darias *et al.* (2016, optical); the orange crosses are from Dhillon *et al.* (2005); the blue crosses are from Hulleman *et al.* (2000), Hulleman *et al.* (2004); and the red crosses are from Morii *et al.* (2005).

$F_{\lambda}d\lambda$, which gives $F_E dE$. All magnitudes were corrected by extinction. To estimate the optical and NIR extinction, we use the equation 2.5 and $R(\lambda)$ from Table 2.6.

In the following subsections we discuss some observational properties of the optical and infrared emissions.

3.1.1 Optical long-term variability

Long-term variability is the variation of the average flux over secular time, in contrast with the short-time pulsed variation, which is presented below. Hulleman *et al.* (2004) pointed to a variability in the infrared emission. Durant & van Kerkwijk (2006c) stated that the source presents a long-term variability in the optical and NIR (see Fig. 3.2), with none or low correlations between different bands. From Figure 3.2, the variability of the K band is more evident than the R and I bands. Durant & van Kerkwijk (2006c) found out that the K band presents a decrease of one a magnitude in a timescale of days. This long-term variability was discarded by Muñoz-Darias *et al.* (2016). The main goal of the authors was to perform a detailed calibration of the data, which allowed them to have more precise and reliable data. They do not detect any significant variability in any optical band (g, r, i and z) over a period of 12 years.

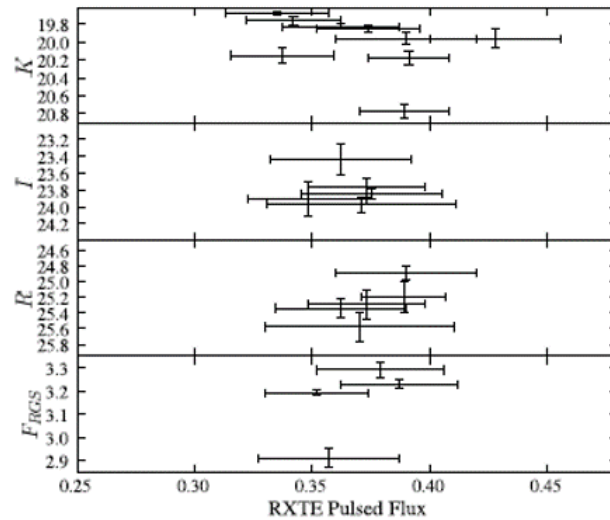


FIGURE 3.2 – Comparison between the long-term variability for the R, I and K bands as well as the soft x-ray emission. Reference: Durant & van Kerkwijk (2006c).

3.1.2 Optical periodic variability

4U 0142+61 also has optical periodic variability (see sec. 2.2). This periodic variability was discovered by Kern & Martin (2002) in the R band and has a period of 8.68 s, equal to the inferred spin. Peak-to-trough pulsed fraction of 27_{-6}^{+8} % is calculated using the equation 2.1, where F_{max} and F_{min} represents the maximum and minimum flux detected in the pulsed emission. The pulsed profile is displayed in Figure 3.3.

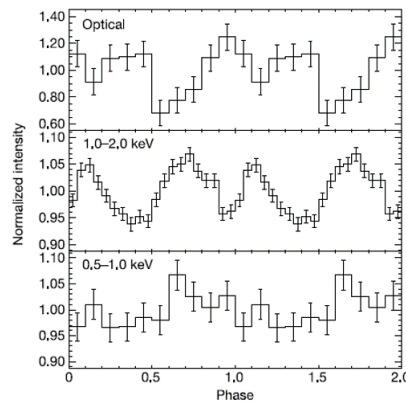


FIGURE 3.3 – The top panel is the pulsed profile in the R band. The middle and bottom panel are the 1.0 – 2.0 keV and 0.5 – 1.0 keV soft X-ray pulsed profile by Chandra. Reference: Kern & Martin (2002).

Kern & Martin (2002) also attempt to the fact that the optical pulsed fraction is 10 times larger than the soft X-ray, which weakens the possibility that the optical emission comes from a passive disk reprocessing light from the soft X-rays emission. Later Dhillon *et al.* (2005) also studied the pulsed fraction and profile in the i' band for 4U 0142+61, which we presented in the section 2.2.

Morii *et al.* (2009) searched for NIR periodic variability in the K' band. They didn't find any significant signal for that and presented an upper limit for the rms pulsed fraction of 17 % (90 % confidence level).

3.1.3 Polarimetry

Wang *et al.* (2012) searched for the presence of circular polarization in the I band. They found a degree of circular polarization (V) of $1.1 \pm 2.0\%$ or $|V| < 4.3\%$ (90% confidence level). The degree of linear polarization (P) is $1.0 \pm 3.4\%$ or $|P| < 5.6\%$ (90% confidence level) for the same band (Wang *et al.*, 2015). These values of polarization suggest that the emission mechanism of 4U 0142+61 is different from those presented by radio pulsars.

3.1.4 Presence of emission lines

The observations of Muñoz-Darias *et al.* (2016) set that 4U 0142+61 is consistent with a featureless continuum optical emission and the equivalent width upper limit for the emission line of $H\alpha$ is 25 \AA . Figure 3.4 shows the absence of any observed emission line for the optical emission.

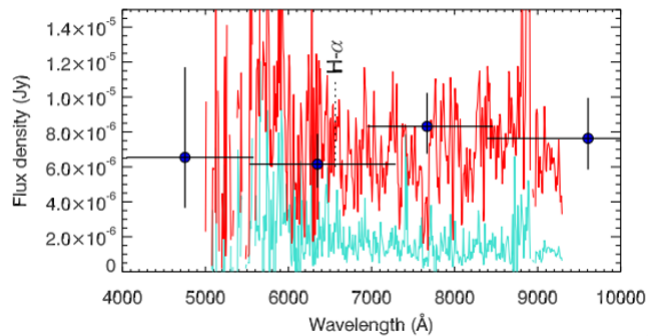


FIGURE 3.4 – Optical spectrum of 4U 0142+61 (in red) and the spectrum of errors (in blue). The blue dots are the photometric values of SDSS bands. The dotted line marks the wavelength where we should see the $H\alpha$ lines. All the data were corrected by extinction ($E(B-V)=1.5$). Reference: Muñoz-Darias *et al.* (2016).

3.2 X-ray emission

The 4U 0142+61 soft X-ray spectrum was observed by several telescopes in the past decades, e.g., White *et al.* (1996, ASCA), Juett *et al.* (2002, Chandra), Göhler *et al.* (2005, XMM-Newton) and Enoto *et al.* (2011, Suzaku). The 4U 0142+61 X-ray quiescent spectrum is featureless, discarding the presence of cyclotron lines for magnetic fields in

the range of $1.9 - 9.8 \times 10^{14}$ G (Juett *et al.*, 2002). Moreover, the soft and hard X-rays components are stable over time.

Meanwhile, its hard X-ray emission was discovered by Kuiper *et al.* (2006, INTEGRAL) in the 20 – 300 keV range and was also observed by other telescopes, such as Tendulkar *et al.* (2015, NuSTAR) in the 3 – 79 keV. A review of the high-energy observations of 4U 0142+61 can be found in den Hartog *et al.* (2008) and Enoto *et al.* (2017).

3.2.1 High-energy periodic variability

4U 0142+61 present periodic variability in both soft and hard X-rays. The pulsed profile for different energy ranges is presented in Figure 3.5. Figure 3.5 clearly shows that the pulsed profile is different for each energy range. Moreover, neither the pulsed fraction nor the shape of the pulsed profile change over time. From the pulsed profile, it is possible to estimate the fraction of the pulsed emission for the unpulsed and pulsed components, which is shown in the Figure 3.6.

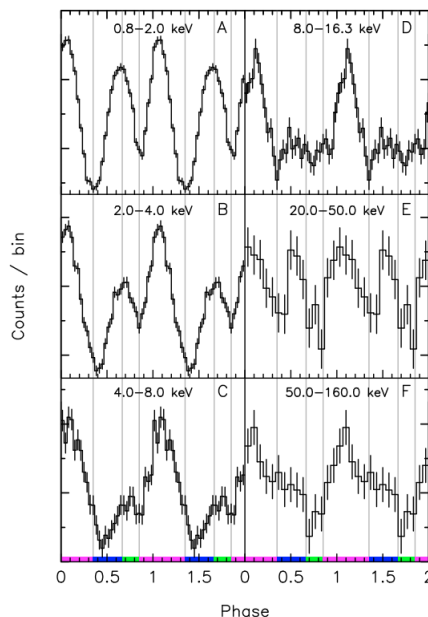


FIGURE 3.5 – 4U 0142+61 pulse profiles from soft to hard X-rays. In panels A, B and C, pulse profiles in the energy ranges 0.8-2.0 keV, 2.0-4.0 keV and 4.0-8.0 keV are the sums of the *XMM-Newton*. Panel D presents the *RXTE-PCA* pulse profile in the energy band 8.0-16.3 keV taken from Kuiper *et al.* (2006). In panels E and F *INTEGRAL* pulse profiles are shown in the energy ranges 20-50 keV and 50-160 keV. Phase interval blue (Ph. I) is the secondary pulsed from *INTEGRAL* profile, green (Ph. II) is the DC level from *INTEGRAL* profile and pink (Ph. III) is the main pulsed from *INTEGRAL* profile.

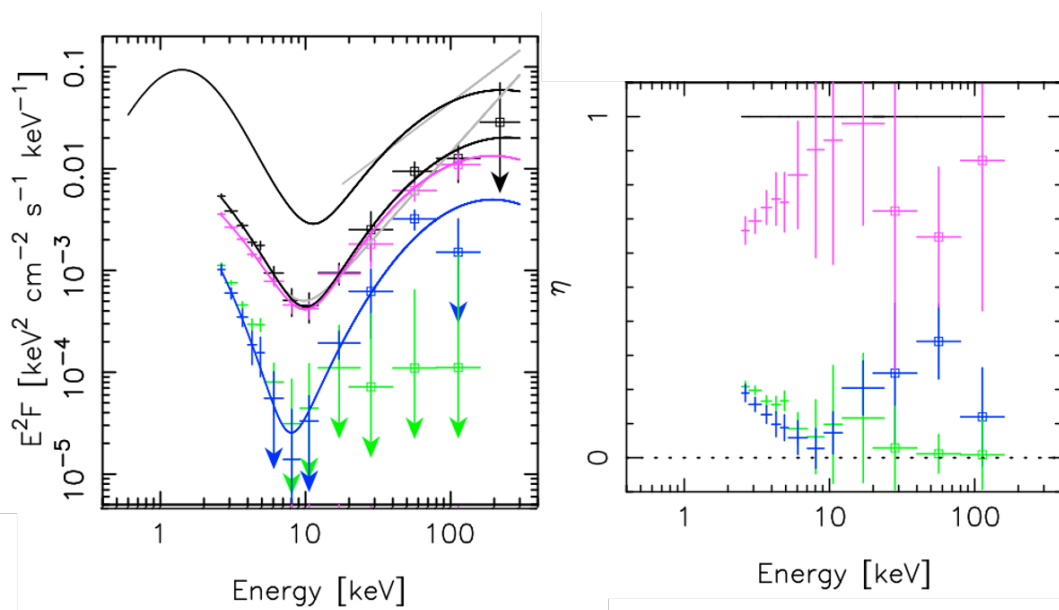


FIGURE 3.6 – *left panel*: the phase-resolved pulsed-emission spectra and fits of INTEGRAL (square symbols) and RXTE-PCA (without markers) are presented. Black is the total-pulsed spectrum, the colored lines are from the same phases from fig 3.5 and the grey is the best power-law fit for the INTEGRAL total-spectrum and the power-law fit for the total-pulsed spectrum. The arrows indicate the flux measurements with a significance less than 1.5σ . For comparison the INTEGRAL/XMM-Newton-B total-spectrum fit is shown in black. *Right panel*: η is defined as the fraction of the pulsed emission in a selected phase interval Ph I, Ph II or Ph III of the total-pulsed emission, i.e. the sum equals unity.

3.3 Complete SED of 4U 0142+61

In section 5.1 we fit the SED of 4U 0142+61 using the accreting WD model presented in chapter 4. For this, we chose a set of data for each energy range to build the complete SED.

For the optical range, we picked out the Gran Telescopio Canarias (GTC) optical data from Muñoz-Darias *et al.* (2016) (see Table 3.1), because they comprise a quasi-simultaneous data set in all optical bands (except from the faint and never observed *u* band), have a homogeneous reduction, a careful differential photometry calibration, and are also consistent with previous measurements. For the NIR, we selected the Gemini J, H and K_s observations from Durant & van Kerkwijk (2006c) (see Table 3.1), because they provide a smoother SED when combined with the GTC optical data and the MIR Spitzer data in 4.5 and 8.0 μm from Wang *et al.* (2006).

TABLE 3.1 – Optical and near-infrared data used in the 4U 0142+61 modelling. The errors in parenthesis represent the zero-point error and were also considered in the fitting procedure.

Band	$A(\lambda)$	Observed Mag.	Date	Reference
g	3.28	$27.37 \pm 0.25(0.58)$	2013-08-09	1
r	2.30	$25.79 \pm 0.07(0.26)$	2013-08-09	1
i	1.70	$24.55 \pm 0.05(0.22)$	2013-08-09	1
z	1.27	$23.76 \pm 0.07(0.28)$	2013-08-09	1
J	0.71	21.97 ± 0.16	2004-11-02	2
H	0.46	20.69 ± 0.12	2004-11-02	2
K_s	0.30	19.96 ± 0.07	2004-11-02	2

References:

- (1) Muñoz-Darias *et al.* (2016)
- (2) Durant & van Kerkwijk (2006c)

For the soft X-rays, we decided to use the data from Suzaku Enoto *et al.* (2010)¹, which is deconvolved from the instrumental response. To compare with the model, the soft X-rays data must be corrected by the interstellar extinction. We adopt N_H estimated by the metal edges models (see sec. 2.3.2) value of $6.4 \times 10^{21} \text{ cm}^{-2}$. To properly cover the hard X-range, we used the data from Wang *et al.* (2014, INTEGRAL, 18 – 500 keV)². Figure 3.7 presents the complete SED of 4U 0142+61 .

The comparison between the dereddened optical emission from Muñoz-Darias *et al.* (2016) and the deabsorbed X-rays data shows that is very unlikely that the optical emission is a tail of the X-ray emission. This suggests that the soft/hard X-rays and optical/infrared

¹Observations taken in 2007-08-13 04:04:13 (seq. number 402013010). Kindly provided by the authors.

²Observations taken from 2003.12 up to 2011.7. The fluxes and error bars from 18-250 keV were taken from Fig.4 of the refereed article of whereas the 250-500 keV data were kindly provided by the authors.

emissions have different origins.

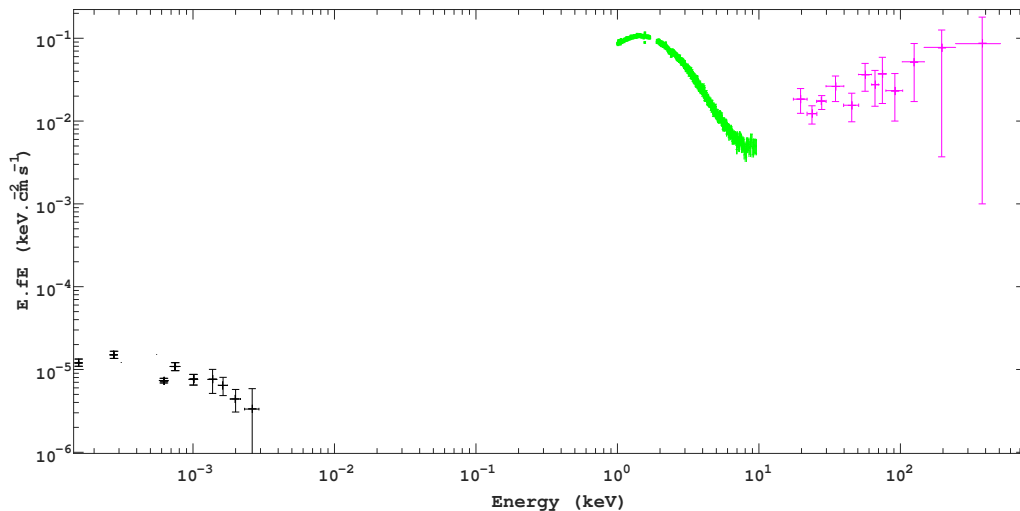


FIGURE 3.7 – Derreddened and deabsorbed SED of 4U 0142+61. The black crosses are from Wang *et al.* (2006, mid-infrared), Durant & van Kerkwijk (2006c, near-infrared) and Muñoz-Darias *et al.* (2016, optical); green crosses are soft X-rays from Enoto *et al.* (2010, Suzaku); and the magenta crosses are the 2003.12 data from Wang *et al.* (2014, INTEGRAL).

3.4 Proposed emission models

3.4.1 Magnetar model

The most accepted scenario is the magnetar model, that was first proposed by Duncan & Thompson (1992). In this model, the SGR/AXPs presents a huge magnetic field (B), in the range of $10^{13} - 10^{15}$ G, and their persistent X-ray luminosity, as well as the bursts and flares typical of these sources (Mazets *et al.*, 1979; Hurley *et al.*, 1999a; Hurley *et al.*, 1999b), are believed to be powered by the decay of their ultra strong magnetic fields.

The hard and soft X-ray emissions were fitted by Hascoët *et al.* (2014), using the model proposed by Beloborodov (2013). Specifically, the hard X-rays emission is caused by the production of e^-e^+ pairs close to the neutron star surface and the soft X-ray emission requires a combination of two modified black bodies, one of them representing the emission of the photosphere and the other one, a hot spot. The Figure 3.8 shows the fit for this energy range.

In the magnetar paradigm, Wang *et al.* (2006) showed that the infrared emission (near and mid) of 4U 0142+61 is well fitted by a passive fallback disk (Fig. 3.9), which emits the reprocessed X-ray that came out from the NS. This fallback disk is formed by debris and gas of the supernova that did not get away from the NS yet due to the short life time

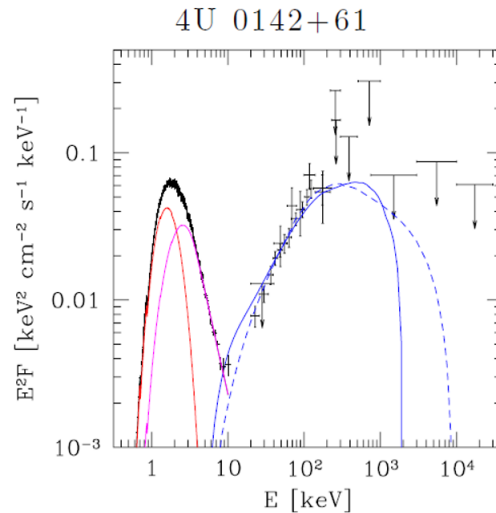


FIGURE 3.8 – Magnetar fit to high-energy emission of 4U 0142+61 from Hascoët *et al.* (2014). The fit is composed by the cold blackbody (red), the hot (modified) blackbody (magenta), and the coronal outflow emission (blue). The dashed blue curve shows the best fit of the hard component obtained when only the phase-averaged spectrum is considered and the phase-resolved data are neglected. The data and model in the figure are not corrected for interstellar absorption. Reference: Hascoët *et al.* (2014).

of the source as NS. This disk is expected to be mostly passive, however, a small amount of matter can fall in the NS occasionally.

The optical emission was modelled as a power-law by Wang *et al.* (2006) (see Figure 3.9), initially thought to be of magnetospheric origin. However, the proposed fit of Hascoët *et al.* (2014) does not cover the optical range and, therefore, the magnetar model lacks an explanation for its origin.

Another magnetospheric proposal had been raised to explain the optical SED of 4U 0142+61. For instance, Eichler *et al.* (2002) pointed out that the optical and infrared can be caused by coherent emission from the magnetosphere, possibly by synchrotron emission. However, Wang *et al.* (2015) discarded this model because the linear polarization for the I-band is too faint.

3.4.2 Accreting NS model

The NS accreting scenario was raised by van Paradijs *et al.* (1995) and Alpar (2001). The general behavior of accretion is modelled as follows: the accreting matter comes from a disk and falls into the NS until the shock happens and the hard X-rays are produced by bulk-motion Comptonization. If this shock happens relatively far from the NSs most of this energy escapes. However, if it happens very closely of the NS surface, part of this emission is absorbed by the NS and re-emitted in the soft X-ray energy range. The

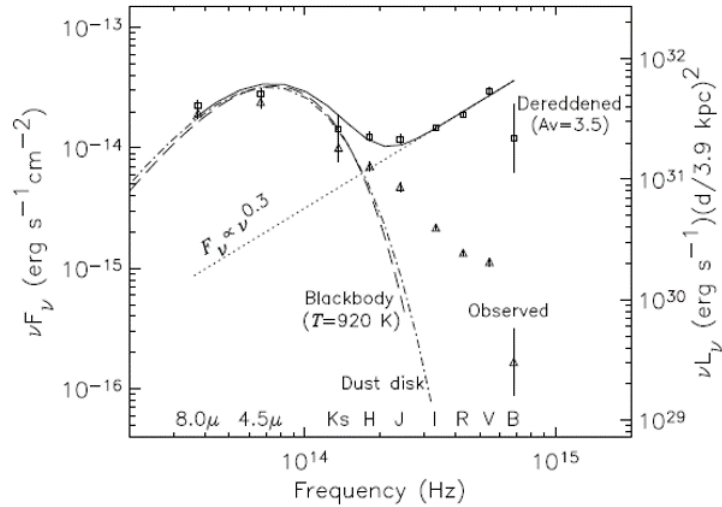


FIGURE 3.9 – Optical/infrared SED of 4U 0142+61 . The dot-dashed line represents the dust disk model, the dashed line is a blackbody component and the dotted line is a power-law. The triangles are the observed data and the squares are the deabsorbed data for $A_v = 3.5$. The considered distance was 3.9 kpc. Reference: Wang *et al.* (2006).

model uses two spots to explain the pulsed emission. The first soft X-ray spot is modelled by thermal Comptonization and the second one, by a thermal blackbody. Figure 3.10 presents a fit of 4U 0142+61 in this model (Zezas *et al.*, 2015). Moreover, Trümper *et al.* (2013) fitted pulsed profiles at all X-ray energies.

In this model, the optical and infrared emission comes from a disk and acts as a reservoir of matter for the accretion. The disk was never modelled jointly with the X-rays. Conversely, previous works have already discussed the fit of an accretion disk. Hulleman *et al.* (2000) and Perna *et al.* (2000) discarded the NS accretion disk hypotheses for 4U 0142+61 because the expected flux by this scenario is greater than the observed. However, they use the irradiation efficiency as a fixed parameter.

Ertan *et al.* (2007) used this efficiency as a free parameters to help fit the data. Ertan *et al.* (2007) fitted the infrared and optical emission using viscous energy dissipation provoked by the mass transfer through the disk and irradiation by the X-ray luminosity. They pointed out that the emission could be entirely explained by dissipation of the X-rays. However, this hypothesis is unlikely once the disk properties are in agreement with a accretion scenario. They explain that the pulsed component of the emission can be caused by magnetospheric emission powered by a disk-shell dynamo. However, further calculations about that optical pulse are not shown. Figure 3.11 shows the optical/infrared fitted spectra.

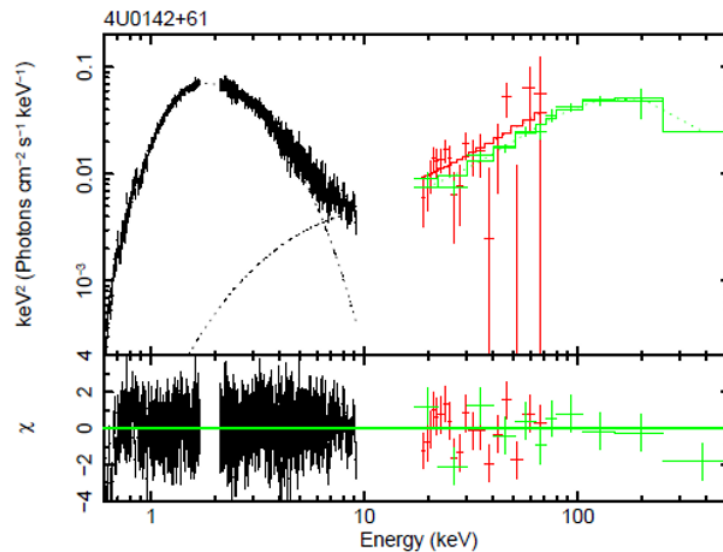


FIGURE 3.10 – *Suzaku* (black and red) and INTEGRAL (green) corrected from instrumental response spectra of 4U 0142+61 fitted with the XSPEC thermal and bulk Comptonization models. Reference: Zezas *et al.* (2015).

3.4.3 WD pulsar model

In the WD pulsar scenario, the X-ray emission is caused by a pulsar-like emission (Malheiro *et al.*, 2012a) and the optical/infrared data is explained by the WD photosphere and by a disk (Rueda *et al.*, 2013). This WD pulsar model have been used to explain the emission of other objects, such as AR Scorpii (Geng *et al.*, 2016), however, no attempt to fit the X-ray emission 4U 0142+61 in this model was presented up to date.

The possibility to fit the optical/infrared data such as a generic WD was raised by several articles about the optical emission of 4U 0142+61. Hulleman *et al.* (2000) tried to explain the optical data in a WD context. They were able to fit the optical flux as Rayleigh-Jeans tail of a blackbody with $T \sim 4 \times 10^5$ K and radius varying from 0.011 to 0.017 R_{\odot} (for a distance of 5 kpc). Hulleman *et al.* (2004) discarded it due to the struggle to explain the long-term optical variability and the excess of the predicted B-band flux. However, the presence of a long-term variability were questioned by Muñoz-Darias *et al.* (2016) (see sec. 3.1). Moreover, the excess in the B-band could be adjusted by some absorption at the electron cyclotron frequency for the magnetic field of the order of 10^8 G (Hulleman *et al.*, 2004).

Kern & Martin (2002) present the optical periodic variability for the first time (see sec. 3.1) and cite the presence of variability in other three isolated high magnetic WDs: Feige 7, PG 1031+234 and RE J0317-853. In this high magnetic WD scenario, variability in the surface temperature can be caused by surface variation on the magnetic field strength.

The first endeavor to fit 4U 0142+61 in the specific WD pulsar model was performed

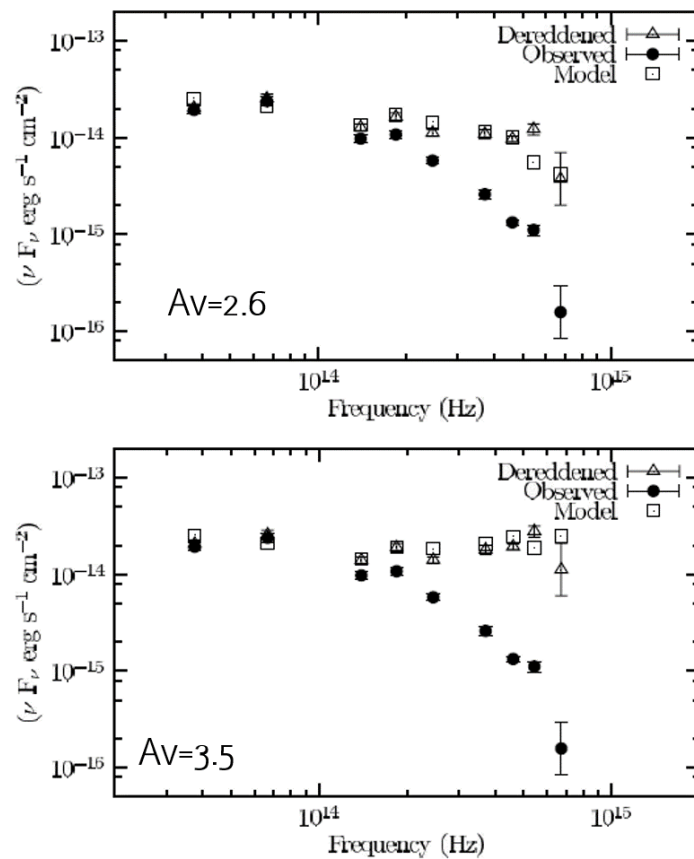


FIGURE 3.11 – fit of 4U 0142+61 in the irradiated-disk (Ertan *et al.*, 2007). Circles are the absorbed data (taken from Hulleman *et al.* (2000), Hulleman *et al.* (2004), Morii *et al.* (2005), Durant & van Kerkwijk (2006c), and triangles are data dereddened ($A_V = 3.5, 2.6$). Squares are the irradiated-disk model energy flux. Reference: Ertan *et al.* (2007).

by Rueda *et al.* (2013), which presents a model for the optical and infrared persistent emission in a double degenerated WD merger. The variability is not modeled. On that model, the optical emission would be caused by WD surface and the infrared, by a disk. For that reason, the infrared data is modelled as a multi-temperature blackbody and the optical data as a simple blackbody model. The parameters obtained for that models are $R_{WD} = 0.006 R_{\odot}$ and $T_{eff} = 131,000$ K for the WD photosphere. The disk was fitted following a debris disk recipe (see sec. 4.1.3), resulting in $R_{in} = 0.97 R_{\odot}$ and $R_{out} = 51.1 R_{\odot}$ for the internal and external disks, respectively. The Figure 3.12 shows the fitted optical/infrared SED.

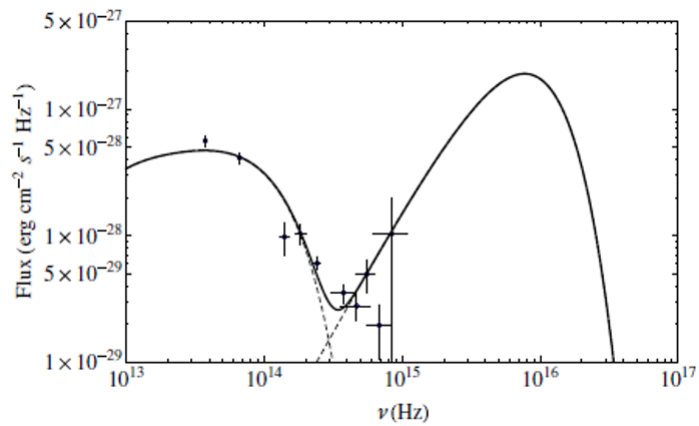


FIGURE 3.12 – Fit of 4U 0142+61 in WD pulsar model presented by Rueda *et al.* (2013). The data is from Hulleman *et al.* (2000), Hulleman *et al.* (2004), Morii *et al.* (2005), Dhillon *et al.* (2005), Durant & van Kerkwijk (2006c), Morii *et al.* (2009). The dashed lines are the disk and photosphere components and the bold line is the sum of both components. The observed data are de-reddened ($A_v = 3.5$) and the considered distance was 3.6 kpc. Reference: Rueda *et al.* (2013).

The WD pulsar model is able to explain the optical and infrared average data. However, the model did not attempt to fit neither the pulsed emission nor the X-rays. Thus, this scenario lacks in completeness.

4 An accretion model for isolated white dwarfs

In this chapter, we describe the scenario and the quantitative model used to explain the emission of 4U 0142+61 as an isolated WD. This model takes all quiescent emission of 4U 0142+61 into account. The optical/infrared range is described by the WD photosphere and a debris disk, the hard X-rays are emitted by the accretion column and the soft X-rays, by a hot spot.

For the disk, we use the same model to fit disks around isolated WDs, which is formed by a dusty external region and a gaseous internal region. Even though only the dusty region is observed in most WDs, the presence of the gaseous region has already been confirmed for some objects, such as HE 1349-2305 (Melis *et al.*, 2012).

For the X-rays, we use the theory for Cataclysmic Variables (CVs) to fit the X-ray SED of SGR/AXPs in an accreting WD prescription. The reason is explained as follows. In a simple approximation, equation 4.1 gives the gravitational potential energy released by the accretion of an amount m of mass onto the surface of the WD of mass M_{WD} and radius R_{WD} (Frank *et al.*, 2002).

$$\Delta E_{acc} = \frac{GM_{WD}m}{R_{WD}}. \quad (4.1)$$

In equation 4.1, G is the gravitational constant. If we derive eq. 4.1:

$$\frac{d\Delta E_{acc}}{dt} = \frac{GM_{WD}}{R_{WD}} \frac{dm}{dt}$$

We can estimate the accretion rate $\dot{M} = dm/dt$ using equation 4.2 (Frank *et al.*, 2002).

$$\dot{M} = \frac{L_X R_{WD}}{GM_{WD}} \quad (4.2)$$

Thus, if we consider the average mass for an WD (Ferrario *et al.*, 2015, $0.663 M_{\odot}$), the expected \dot{M} for 4U 0142+61 ($\sim 10^{17} \text{ g.s}^{-1}$) is compatible with the accretion rate for CVs

(Patterson; Raymond, 1985). Moreover, the X-ray emission of 4U 0142+61 is pulsed, which is consistent with magnetic accretion. In this case, the in-falling matter follows the magnetic lines and only a fraction of the surface of the WD is heated. Thus, we use the theory for magnetic CVs to model the X-ray emission of 4U 0142+61. This magnetic CV class has two sub-classes: Polars, which have the strongest magnetic fields, and Intermediate Polars (IPs), which have weaker fields.

In the following sections, we discuss all the emission mechanisms we used to fit the spectral energy distribution of 4U 0142+61. Firstly, we present an overview of the proposed model, which is based on accreting WD in binaries. Then, we detailed the expressions and parameters of each emission component. After that, we discuss each of them separately. We finish this chapter presenting the spin-down theory for accreting WDs.

4.1 Emission mechanisms

Depending on the nature of the WD, different types of radiative processes can dominate the release of energy from accretion (Lamb; Masters, 1979). When the value of the magnetic field (B) is smaller than $6 \times 10^6 (L_f/10^{36} \text{erg.s}^{-1})^{2/5}$, where $L_f = L_X/f$ and f is the percentage of the source's surface occupied by the accretion, the bremsstrahlung emission dominates. At this regime, the density of the accreting region is high and the ions and electrons can exchange energy in a speed larger than the electrons can lose energy. The post shock region can achieve a single temperature and can be treated as a single fluid. On the other hand, when the value of the magnetic field (B) is greater than $6 \times 10^6 (L_f/10^{36} \text{erg.s}^{-1})^{2/5}$, the cyclotron emission in the optical and UV dominates. At that regime, the electrons lose energy more quickly than the ions can exchange energy with them and the fluid need to be modelled as two separated fluids.

An schematic model of accretion spectra for two different values of L_f can be observed in Figure 4.1. Even though the cyclotron emission dominates in both curves it is clear how the bremsstrahlung emission is more prominent for larger values of L_f and, consequently, larger values of density for the accretion region (Lamb; Masters, 1979).

In Figure 4.1, it is also possible to note the presence of a soft X-ray blackbody component. Part of the emission (bremsstrahlung or cyclotron) that comes inwards the surface is absorbed and reflected, forming a blackbody component. In general, the value of L_{bb} is smaller but almost equal to $L_{cyc} + L_{brem}$, where L is the luminosity and the suffixes bb , cyc and $brem$ represents the blackbody, cyclotron and bremsstrahlung processes, respectively (Frank *et al.*, 2002). These values are closer because half of the emission produced by the bremsstrahlung and cyclotron processes is emitted inwards and reaches the WD surface.

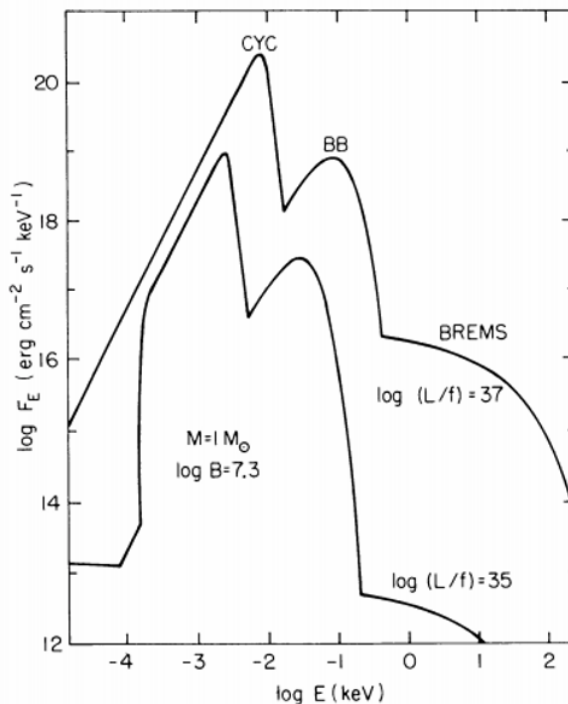


FIGURE 4.1 — X-ray and UV spectrum produced by two different accretion rates onto a $1M_{\odot}$ degenerate white dwarf having a magnetic field of $B = 2 \times 10^7$ Gauss. Reference: Lamb & Masters (1979).

However, there are a few systems, such as EU UMa and DP Leo, where the blackbody component is dominant and $L_{bb} > L_{cyc} + L_{brem}$ (Ramsay; Cropper, 2004). For several years, the cause of this discrepancy between $L_{cyc} + L_{brem}$ and L_{bb} for some objects was a question for debate. One of the first hypothesis stated that nuclear burning could be responsible for that difference. However, steady nuclear burning can only occur for luminosities below $2 \times 10^{32} f \text{ erg.s}^{-1}$ or above $4 \times 10^{37} f \text{ erg.s}^{-1}$, which is not the case for most accreting WD that present higher blackbody component. Later, the presence of blobs of in-falling matter reaching the surface without suffering shock was raised. That way, part of the accreted flow do not contribute for the bremsstrahlung/cyclotron emission in the post shock region but is absorbed and re-emitted such as blackbody (Frank *et al.*, 2002; Wickramasinghe; Ferrario, 2000).

4U X-ray SED, which presents two components, bears some resemblance to IPs SED, but is shifted to higher energies. This shift can be caused by a more massive WD, since the characteristic temperature of the accretion emission increases with the WED mass (Aizu, 1973). Hence, in this thesis, we verify if accretion over a massive WD can explain 4U emission.

Thus, we model 4U 0142+61 as follows. The optical and infrared emissions are be modelled as a sum of the photosphere (blackbody) and a dusty disk (multi-temperature blackbody). This dusty disk is optically thick and the temperature of its inner radius is

close to the grain sublimation temperature, which is about 1500 K for silicates. Conversely, the internal gaseous disk is optically thin and its emission can be neglected. The inner radius of the gaseous disk is equal to the magnetosphere radius. For that point on, the matter flows into the WD surface following the magnetic field lines and the debris disk ceases to exist.

Close to the WD photosphere, the in-falling flow of matter suffers a shock, forming an extremely hot region, the so called post-shock region that emits bremsstrahlung. About half of that energy reaches the WD surface, where it is absorbed and reflected, forming a hot spot. Also, part of the accretion flow can penetrate direct into the photosphere in the form of blobs - no shock is formed. Once the high-energy emission for 4U 0142+61 is pulsed, with two peaks per phase, the most plausible option is that we see the emission from two different accreting regions. This shock+spot region is represented in Figure 4.2. The hot post-shock region emits hard X-rays whereas the hot spot, caused by the reprocessed hard X-rays emission onto the surface, is responsible for the soft X-rays emission.

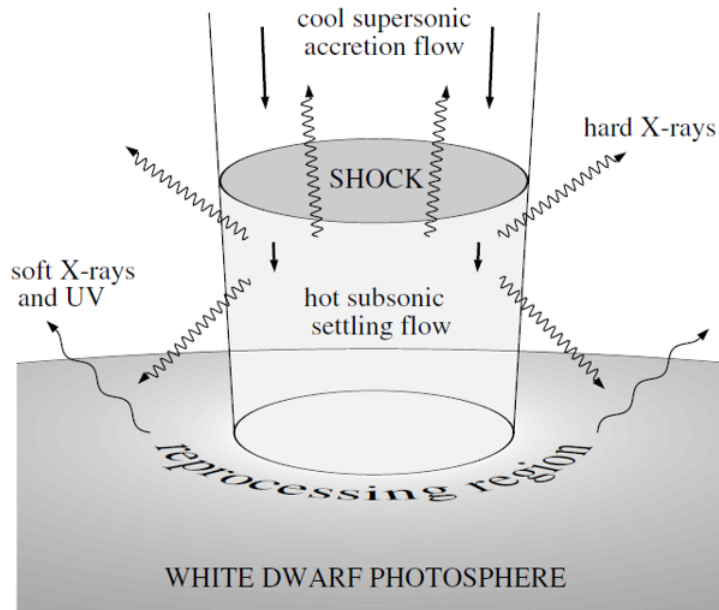


FIGURE 4.2 – Accretion column geometry for a magnetized WD. Reference: Frank *et al.* (2002).

To sum up, the optical and infrared emissions come from the disk and the WD photosphere, which emits as a blackbody. The soft X-rays are due to the hot spots, that also have a blackbody radiation. And the hard X-ray is due to the bremsstrahlung formed in the accretion column. This can be expressed by:

$$F_{total} = F_{disk} + F_{wd} + F_{spot} + F_{brem}. \quad (4.3)$$

In the following sections, we explain each term of equation 4.3. For all terms, we

expand all parameters and state whether they were left fixed or free during the fit. We used a distance of 2.57 kpc (see sec. 2.4) in all calculations. First, we talk about the emission from the accretion column (F_{brem}). After, we discuss the blackbody flux emitted by the photosphere of the WD (F_{wd}). In the end, we describe the emission from the disk (F_{disk}).

4.1.1 Post-shock region

We assume that the post-shock region emits thermal bremsstrahlung. According to Mewe *et al.* (1986), the bremsstrahlung emitted power (in $\text{erg.cm}^{-3}.\text{s}^{-1}.\text{\AA}$) is,

$$P(\lambda, T_{brem}) = 2.051 \times 10^{-22} g_{ff} n_e^2 \lambda^{-1} T_{brem}^{-0.5} \exp\left(\frac{-143.9}{\lambda T_{brem}}\right). \quad (4.4)$$

The parameters n_e , T_{brem} , λ and g_{ff} are the electrons number density, the temperature of the bremsstrahlung emission, the wavelength, and the Gaunt factor respectively. It is necessary to apply the relativistic correction A, given by equation 4.5 (RYBICKI; LIGHTMAN, 1979),

$$A = \begin{cases} 1 & , \text{ for } T_{brem} \leq 9.1 \text{ keV} \\ 1 + 4.4 \times 10^{-10} T & , \text{ for } T_{brem} > 9.1 \text{ keV.} \end{cases} \quad (4.5)$$

The electrons number density (n_e), in cm^{-3} , of the post-shock region can be calculated by (Frank *et al.*, 2002):

$$n_e = 5.9 \times 10^{14} \left(\frac{\dot{M}}{10^{16}}\right) \left(\frac{M_{wd}}{M_{\odot}}\right)^{-1/2} \times \left(\frac{R_{wd}}{10^9}\right)^{-3/2} \left(\frac{f}{10^{-2}}\right)^{-1}; \quad (4.6)$$

and the upper limit of H, in cm, is (Frank *et al.*, 2002):

$$H = 9 \times 10^8 \left(\frac{\dot{M}}{10^{16}}\right)^{-1} \left(\frac{M_{wd}}{M_{\odot}}\right)^{3/2} \times \left(\frac{R_{wd}}{10^9}\right)^{1/2} \left(\frac{f}{10^{-2}}\right). \quad (4.7)$$

For temperatures above ~ 100 keV, we can consider a non-relativistic g_{ff} (Karzas; Latter, 1961; Sutherland, 1998). However, for higher temperatures (which is the case of our fit), we must take into account the relativistic g_{ff} . Thus, we adopt g_{ff} from Nozawa *et al.* (1998), Itoh *et al.* (2000), van Hoof *et al.* (2015). Figure 4.3 shows the comparison between the relativistic and non-relativistic g_{ff} for different values of temperature.

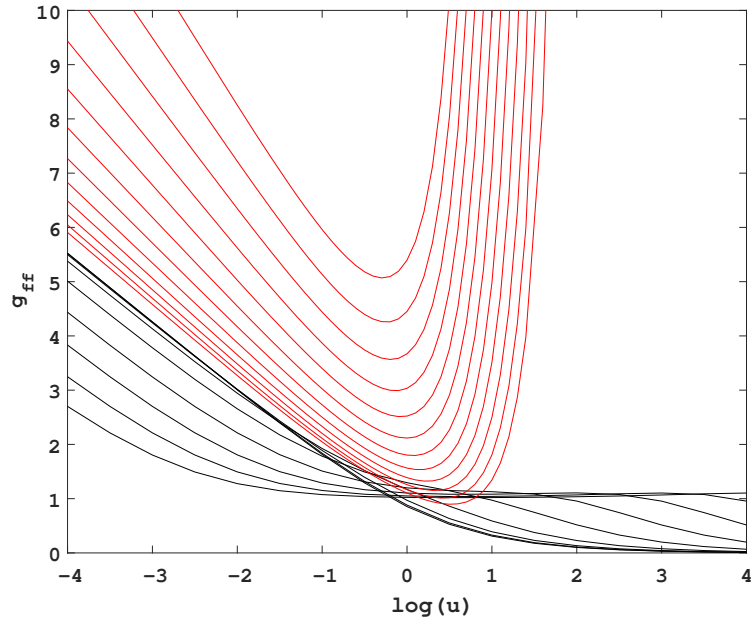


FIGURE 4.3 – Log plot of the Gaunt factor as a function of $u = \frac{h\nu}{kT}$. Each curve represents a different value of temperature normalized as $\gamma^2 = \frac{Z^2 Ry}{kT}$, where $Ry=13.6$ eV and Z is the ion charge. The black lines are the non-relativistic g_{ff} and varies from -4 (upper curve) up to 4 (lower curve). The red lines are the relativistic g_{ff} and varies from -3.4 (upper curve) up to -2.3 (lower curve). Reference: Sutherland (1998), Nozawa *et al.* (1998).

To estimate g_{ff} , it is also necessary to evaluate the ion charge of the in-falling matter, which depends on its chemical composition. Hence we need to define the disk material. 4U 0142+61 in the WD accreting model probably is the product of the merger of two CO WDs (see sec. 6.1). Thus, we consider that the in-falling matter is mainly composed by carbon (Lorén-Aguilar *et al.*, 2009) to estimate g_{ff} .

To estimate the bremsstrahlung emission from the accretion column, we assume that it is optically thin and cylindrical, with a height H and radius R_{brem} . Equation 4.8 gives the flux of the bremsstrahlung emission. Some of their parameters and its values are discussed below.

$$F_{brem}(n_e, R_{brem}, H, T_{brem}, d) = \frac{HP(\lambda, T_{brem})}{4} \left(\frac{R_{brem}}{d} \right)^2. \quad (4.8)$$

Moreover, we can define the emission measure (EM) by relation 4.9:

$$EM = \int n_e^2 dV. \quad (4.9)$$

Thus, the flux F_{brem} can be represented by:

$$F_{brem}(EM, T_{brem}, d) = F_{brem}(n_e, R_{brem}, H, T_{brem}, d). \quad (4.10)$$

This way, the free parameters in the fit are only EM and T_{brem} . The parameters H, n_e and R_{brem} are derived by their relations (eqs. 4.7, 4.6 and 4.21, respectively) and equation 4.9. Furthermore, by T_{brem} and equations 4.19 and 4.21, we can estimate R_{WD} and M_{WD} .

4.1.1.1 Gas-dynamics theory

The parameters from the accretion column, such as temperature, velocity and density of the particles are derived from the gas-dynamics theory, as well as, T_{brem} , H and n_e . For this reason, we present the basic equations to model the shock region. The flow of the steady accreted matter follows the three conservation laws of gas-dynamics, derived from the Navier-Stokes equation. Equation 4.11 is the continuity equation and represents the conservation of mass of the flow (Frank *et al.*, 2002).

$$\frac{1}{r^2} \frac{d}{dr} (r^2 \rho v) = 0. \quad (4.11)$$

The conservation of linear momentum is given by equation 4.12, where f_r is the external force.

$$f_r = \frac{GM\rho}{r^2}. \quad (4.12)$$

At last, the relation 4.13 represents the conservation of energy.

$$v \frac{dv}{dr} + \frac{1}{\rho} \frac{dP}{dr} + \frac{GM}{r^2} = 0. \quad (4.13)$$

Plus, we can define the sound speed (c_s) by equation 4.14, where the index x represents an adiabatic or isothermal flow. The value of c_s is different whether the flow is adiabatic or isothermal.

$$c_s = \left(\frac{dP}{d\rho} \right)_x^{1/2}. \quad (4.14)$$

In either way, the order of magnitude from c_s is the same. The relation 4.15 gives is

an numerical approximation for c_s in km.s^{-1} .

$$c_s \sim 10(T/10^4)^{1/2}. \quad (4.15)$$

Furthermore, c_s represents the speed at which pressure disturbances travel through the gas. Thus, c_s represents the stint of how fast the gas can react to pressure changes. If the pressure of the gas in a region L changes in a time-scale smaller than L/c_s , the flow will take time to adjust to such changes and the pressure distribution will contain some temporary steep changes. On the other hand, if the change occurs in a higher timescale the pressure gradient will remain small (Frank *et al.*, 2002).

Thus, for subsonic flows, moving slower than c_s , the gas can fit the pressure and behaves such as it were in hydrostatic equilibrium. Conversely, for supersonic flows, which moves faster than c_s , the gas cannot respond to pressure changes. For the latter possibility, the gas can suffer some discontinuity of the pressure distribution in order to adjust its value along the flow. This abrupt change in the properties of the flow is known as shock.

Figure 4.4 shows an schematic view of the shock region. The properties of the flow, such as speed, density and temperature, changes abruptly in a small region with the size of the mean free path (λ_d).

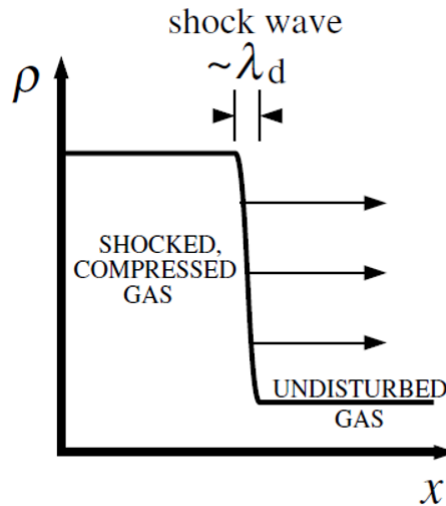


FIGURE 4.4 – The density of the flow is smaller upstream and changes abruptly after the shock. The shock wave has thickness of the order of the mean free path of the gas particles. Reference: Frank *et al.* (2002).

If we assume an adiabatic flow and a strong shock, we can solve the conservation laws for the shock region of the in-falling matter into an WD. We find the change in density (ρ), velocity (v) and temperature (T) due to the shock are given by equations 4.16, 4.17 and 4.18. The index 1 represents the upstream region whereas the index shock represents

the downstream (Frank *et al.*, 2002).

$$\rho_{shock} = 4\rho_1. \quad (4.16)$$

$$v_{shock} = \frac{1}{4}v_1. \quad (4.17)$$

$$T_{shock} = \frac{3}{8} \frac{GM_{WD}\mu \cdot m_H}{kR_{WD}} \quad (4.18)$$

In equation 4.18, G is the gravitational constant, m_H is the mass of atomic hydrogen, k is the Boltzmann constant, μ is the mean molecular weight of the in-falling gas, which we consider 1.714 for carbon in-falling matter (Lorén-Aguilar *et al.*, 2009).

Equation 4.18 gives the relation between M_{WD} , R_{WD} and T_{shock} and, for this reason, is a good way to estimate the temperature of the hard X-ray bremsstrahlung. Moreover, eq. 4.18 is identical to the relation presented by Aizu (1973) to estimate the post-shock temperature.

4.1.1.2 Temperature of the bremsstrahlung emission

The analytic equation 4.18 is the simplest estimate for T_{shock} . Since then, improvements on this formula were presented by several authors. In this thesis, we use equation 4.19 (Suleimanov *et al.*, 2016).

$$T_{shock} = \frac{3GM_{WD}m_H\mu}{8kR_{WD}} \left(1 - \frac{R_m}{R_{WD}}\right). \quad (4.19)$$

In equation 4.19, R_m is the magnetosphere radius, calculated by equation 4.20 (Ferrario *et al.*, 1989).

$$\frac{R_m}{R_{WD}} \simeq 13.4 \left[\frac{B(1 + 3 \sin^2 \beta)^{1/2}}{3 \times 10^7} \right]^{4/7} \left(\frac{f}{10^{-3}} \right)^{2/7} \left(\frac{M_{WD}}{M_\odot} \right)^{-8/21} \left(\frac{\dot{M}}{10^{16}} \right)^{-2/7}. \quad (4.20)$$

The parameter β represents the angle between the magnetic field lines and the axis of rotation.

Figure 4.5 shows an comparison of T_{shock} for equations 4.18 and 4.19 for several values of magnetic field. As we can observe, equation 4.19 presents a smaller value for T_{shock} .

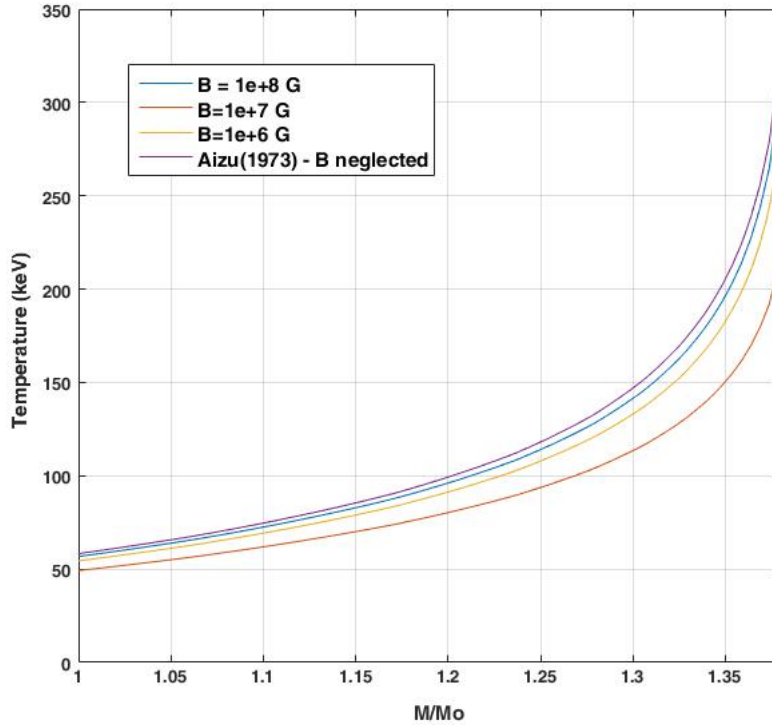


FIGURE 4.5 – Post-shock temperature as a function of the WDs mass for different magnetic fields. We consider $\dot{M} = 10^{16} \text{ g.s}^{-1}$ and $\mu = 0.613$.

We adopt the relation between T_{brem} and T_{shock} also from Suleimanov *et al.* (2016):

$$kT_{brem} = 0.64kT_{shock}. \quad (4.21)$$

4.1.2 Blackbody emission

The WD photosphere and the hot spots emit such as blackbody, where the intensity for a given wavelength λ and temperature T is the Planck function $B(\lambda, T)$ (see eq. A.23, from appendix). The emitting flux for the photosphere (F_{WD}) was calculated by eq. 4.22, where T_{WD} is the effective temperature of the photosphere and R_{WD} is the radius of the WD. F_{WD} is fitted simultaneously with F_{disk} and after the accretion column and hot spot. This way, R_{WD} , which is estimated by the hard X-ray temperature using equation 4.19 and the mass-radius relation from section 4.2, is a fixed parameter for this energy range whereas T_{WD} is a free parameter.

$$F_{WD}(\lambda, T_{WD}, R_{WD}, d) = \pi B(\lambda, T_{WD}) \left(\frac{R_{WD}}{d} \right)^2. \quad (4.22)$$

Meanwhile, the flux for each hot spot on the surface is given by equation 4.23, where

T_{spot} is the temperature of the spot and R_{spot} is the radius of the spot. For F_{spot} , all parameters are free, except the distance.

$$F_{spot}(\lambda, T_{spot}, R_{spot}, d) = \pi B(\lambda, T_{spot}) \left(\frac{R_{spot}}{d} \right)^2. \quad (4.23)$$

4.1.3 Multi-temperature disk

Debris disks around WDs are common for both young and old populations. For instance, several old cool metal-rich WDs have small disks around them, supposedly caused by tidal disruption of small bodies (Jura, 2003). These disks are optically thick and geometrically thin (Metzger *et al.*, 2012) and usually emit from mid-infrared to optical wavelengths. The inner and outer radii are around a fraction to a few R_{\odot} . In contrast, young hot WDs, such as those of the Helix planetary nebulae, have large disks, probably created by collision of Kuiper-Belt-like objects (Chu *et al.*, 2011). Those disks emit in the far and mid infrared and the radii are approximately a few AU (Chu *et al.*, 2011). In both cases, the WD accretes matter from the disk.

Once 4U 0142+61 emits in the mid-infrared to optical, we fit the data adopting the disk flux relation proposed by Chiang & Goldreich (1997) for disk around T Tauri stars. This same model was used by Jura (2003) to fit the disk of the cold WD G29-38 and by Rueda *et al.* (2013) to fit the infrared emission of 4U 0142+61 in the WD pulsar scenario of 4U 0142+61. The emitted flux from the debris disk is given by equation 4.24.

$$F_{disk}(\nu, T_{in}, T_{out}, T_{WD}, R_{WD}, d) = 12\pi^{1/3} \cos(i) \left(\frac{R_{WD}}{d} \right)^2 \left(\frac{2kT_{WD}}{3h\nu} \right)^{8/3} \left(\frac{h\nu^3}{c^2} \right) \times \int_{x_{in}}^{x_{out}} \frac{x^{5/3}}{e^x - 1} dx. \quad (4.24)$$

In this equation, $x = h\nu/kT$, where T is the debris disk temperature which ranges from T_{out} to T_{in} and T_{wd} is the WD effective temperature. This expression assumes that the temperature decays as $r^{-3/4}$. Thus, for T_{in} and T_{out} we can relate a radius value of R_{in} and R_{out} . Thus, a given value of T_{in} (T_{out}) corresponds to a value of R_{in} (R_{out}). For radii between R_{in} and R_m , the disk is gaseous and does not emit. In addition, we consider that the disk is face-on ($\cos(i) = 1$).

F_{disk} is fitted simultaneously with F_{wd} . We used the estimated value of R_{wd} from the hard X-rays. T_{wd} , T_{in} and T_{out} are free parameters in the fit.

4.2 Mass-radius relation

Nauenberg (1972) presents equation 4.25 for the mass-radius relation of WDs, where M_{ch} is about $1.44 M_{\odot}$ and is known as the limiting mass of Chandrasekhar (eq. 4.26). Also, μ_e is the mean molecular weight of electrons, which we considered 2 (Filho; Saraiva, 2000).

$$\frac{R}{R_{\odot}} = \frac{0.0225 \left[1 - \left(\frac{M}{M_{ch}}\right)^{4/3}\right]^{1/2}}{\mu_e \left(\frac{M}{M_{ch}}\right)^{1/3}}. \quad (4.25)$$

$$M_{ch} = \frac{5.816}{\mu_e^2} M_{\odot}. \quad (4.26)$$

Figure 4.6 shows the observed data of those parameters for a WD with carbon core and the mass-radius relation (eq. 4.25). We can see that, although it does not ideally represent all WDs, such a relation is capable of showing a good estimate for the radius of an specific mass.

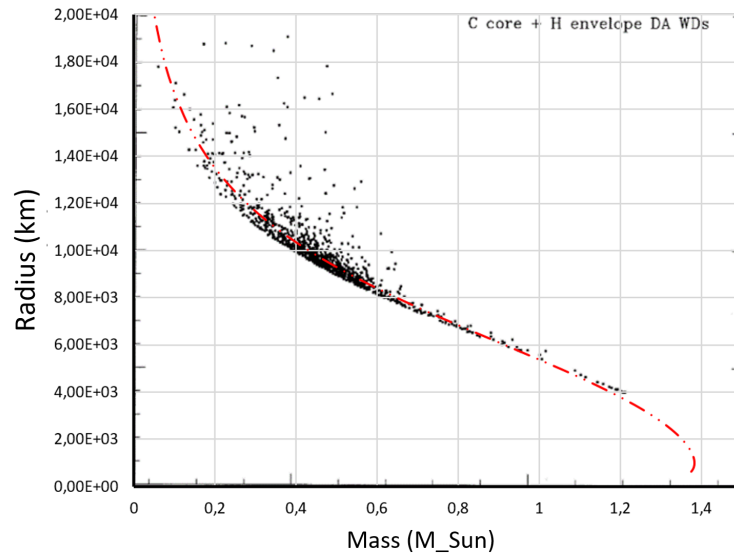


FIGURE 4.6 – The black dots from Madej *et al.* (2004) are from DA WDs with carbon nuclei. The red line is the mass radius relation from Nauenberg (1972).

Relation 4.25 neglects the effects of the general relativity and, for that reason, do not represent properly an WD closer to the Chandrasekhar limiting mass. Carvalho *et al.* (2018) present the mass-radius relation for the general relativity case. An comparison between the classical and the relativistic relation is shown in Figure 4.7. We can observe some differences: the highest mass for the general relativity case is slightly smaller, $\sim 1.41 M_{\odot}$ and the radius is smaller for a fixed mass.

For the maximum mass of the general relativity case ($1.4154 M_{\odot}$) the radius is 1021 km.

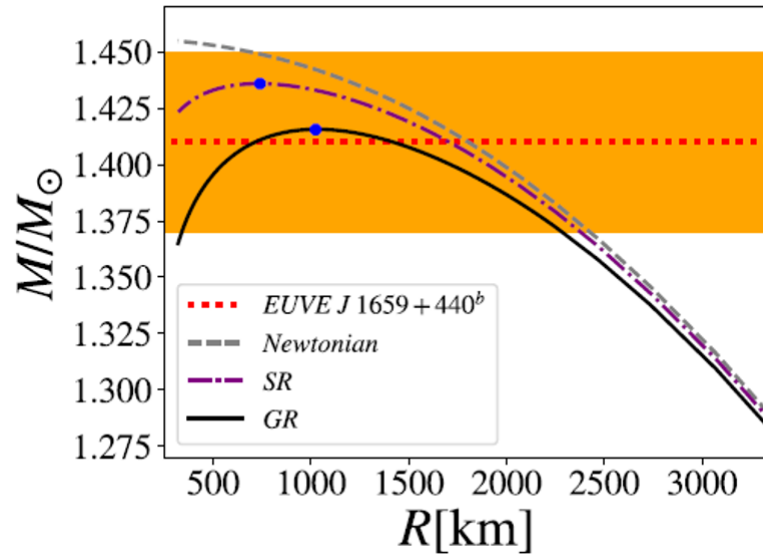


FIGURE 4.7 – Comparison for different mass-radius relations for high-mass WDs. The blue circles marks the maximum mass for each model. The red line represents the mass value for the most massive WD EUVE J1659+440 (Vennes *et al.*, 1997) and the orange strip is the uncertainty for this mass value. SR = special relativity, GR = general relativity.

Using the relation 4.25, the radius is 1200 km, 15% smaller. Therefore, for those near-Chandrasekhar regions, we adopt the General Relativistic radius from Carvalho *et al.* (2018).

5 A model for 4U 0142+61

In this chapter, we fit the SED of 4U 0142+61 with the accreting WD model, presented in Chapter 4. Each energy range is modelled as follows. Hard X-rays are fitted with a bremsstrahlung accretion column, the soft X-rays is modelled with two blackbodies and the optical/infrared emission is the sum of the debris disk and the WD photosphere. Moreover, we discuss the most important derived parameters and its consequences.

5.1 Fitting 4U 0142+61 SED

As the model parameters for each spectral region are not the same, we opted to fit spectral regions separately. Doing this, we could also constrain some parameters in a simpler way than doing an overall fitting. First, we fit the hard X-rays independently of other parts of the SED. After that, we fitted the soft X-rays considering the contribution of hard X-rays bremsstrahlung in this energy range. Finally, we fit the optical/infrared emission taking all the previously fitted components and parameters into account.

To fit the SED of 4U 0142+61 we use the data presented in Figure 3.7. All the fitted data is dereddened and deabsorbed (see Cap. 3 for more details). We have used Markov Chain Monte Carlo (MCMC) to estimate the parameters and their uncertainties, which we discuss more thoroughly in Section 5.1.1. The parameters of the fit and the resulting SED are shown in Table 5.1 and Figures 5.3 and 5.2.

The fit quality of the hard X-rays increases for high bremsstrahlung temperatures. Figure 5.1 shows the variation of χ^2 with T_{brem} .

By the equations 4.19 and 4.21 we can only reach the high bremsstrahlung temperatures for near-Chandrasekhar white dwarfs. For instance, we need a $1.36 M_{\odot}$ WD to get ~ 250 keV, which gives $\chi^2/dof = 1.05$. Also, the highest temperature we can reach for the limiting mass of $1.41 M_{\odot}$ and radius of 1021 km (Carvalho *et al.*, 2018) is 670.3 keV. Moreover, $1.41 M_{\odot}$ is the estimated mass of EUVE J1659+440, the highest value ever measured for a WD (Vennes *et al.*, 1997).

Thus, we fixed the temperature in 670.3 keV in order to guarantee the best fit for a

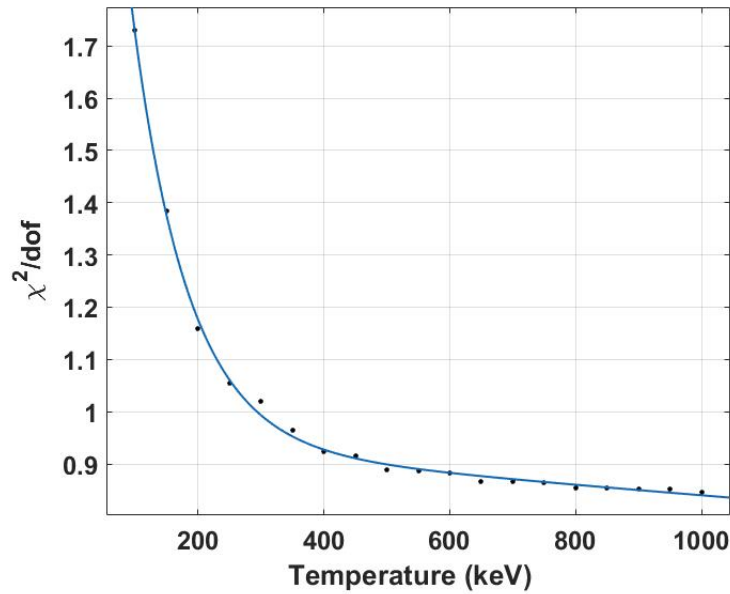


FIGURE 5.1 – Relation between T_{brem} and χ^2/dof . The black point are the minimum χ^2/dof for each bremsstrahlung temperature and the blue curve is the best fit of those points.

WD scenario. We fit the hard X-rays data using the equation 4.10. This equation fits the hard SED using solely EM (see eq. 4.9), which is a free parameter, T_{brem} (fixed at 670.3 keV) and d (fixed at 2.57 kpc). Thus, the only free parameter for the MCMC fitting of the hard X-rays fit is EM.

After modelling the hard X-rays, we find the best fit for soft X-rays. The bremsstrahlung component is also included in the fit the soft X-ray SED. To increase the quality of the fit, we use two black bodies components, which can have different temperatures and radii. The flux for each hot spot is given by Equation 4.23. In this case, T_{spot1} , R_{spot1} , T_{spot2} and R_{spot2} are free parameters and d is fixed. In Table 5.1, we present the parameters for hard and soft X-rays fit and Figure 5.2 shows the fitted model.

Using the parameters obtained in X-rays fits, we can derive the following quantities. First, we estimate L_s , L_h and L_X , which are the soft, hard and total bolometric luminosity due to accretion, respectively. Using this estimated L_X , we calculate \dot{M} (eq. 4.2). By Equation 4.9, we can relate EM with H , n_e and the area of the column. We consider the area of the column equal to the soft X-rays emitting area, which gives an average radius for R_{brem} of 9.45 km. Thus, we were able to estimate n_e using Equations 4.9, 4.6. Knowing EM, n_e and R_{brem} , we have the value of H , which is 28% of the upper limit given by equation 4.7.

To fit the optical and infrared emission, we use the WD photosphere blackbody and the debris disk. The flux of the WD photosphere and the disk are given by Equations 4.22

and 4.24, respectively. We use same values of R_{wd} derived from the bremsstrahlung fit. Moreover, we included the tail of the bremsstrahlung component in the fit despite its small influence in this energy range. We do not consider the presence of hot spots in the fit of the optical/infrared because its emission in this energy range is negligible. The best fit for the optical and infrared is presented in Table 5.1 and in Figure 5.2. The optical fit take into account only the data from Figure 3.7, which are represented by black crosses in Figure 5.2. We put the optical data from Hulleman *et al.* (2000), Hulleman *et al.* (2004) in Figure 5.2 to explicit that the fit is also close to this different set of data. Our model is able to fit consistently all observational data of 4U 0142+61. Figure 5.3 shows all fitted components along with the observed SED.

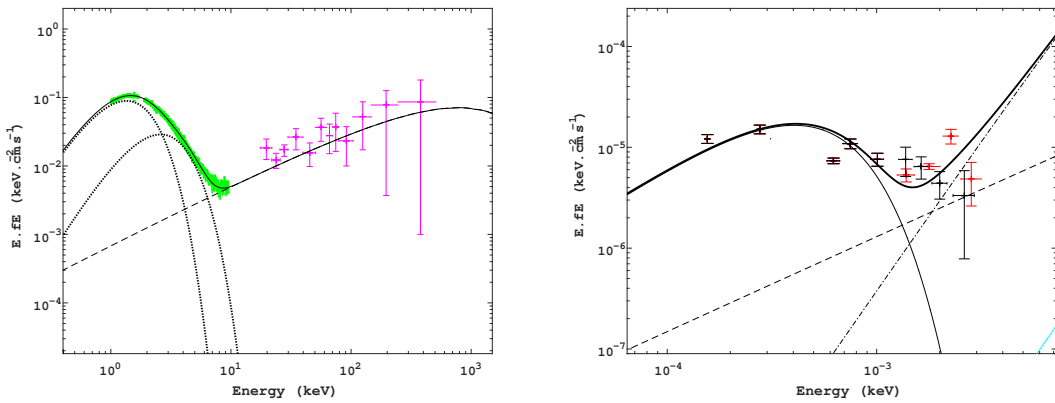


FIGURE 5.2 – *Left panel:* X-rays fit of 4U 0142+61. The dotted lines the blackbody components, the dashed line is the bremsstrahlung component and the bold black line is the total emission. The green and magenta crosses are the same from Fig. 3.7. *Right panel:* Optical/infrared fit of 4U 0142+61 the filled line is the disk component, the dot-dashed line is the blackbody emitted by the WD photosphere, the dashed line is the hard X-rays bremsstrahlung tail and the bold black line is the total emission. The black crosses are the same data from Fig. 3.7 and the red crosses are from Hulleman *et al.* (2000), Hulleman *et al.* (2004).

5.1.1 Estimate of errors

To find the probability distribution of parameters values we use the MCMC method from Goodman & Weare (2010). After that, we fit a Gaussian for each parameter probability distribution to estimate their expected value and uncertainties. The MCMC method was applied for each energy range separately. The expected values and errors for each fitted parameters are presented in Table 5.1.

For the hard X-rays, Figure 5.4 shows the distribution of EM for the fixed $T_{brem} = 670.3$ keV. For the soft X-rays, to get a more accurate error bar, we only consider combination with $\chi^2/dof < 1.3$. Figure 5.5 shows the scatter plot for the parameters. We can estimate the 1σ error by finding the best Gaussian for each parameter distribution.

TABLE 5.1 – Parameters of the fitting of 4U 0142+61 in the accreting white dwarf model. The fixed parameters were derived before the fit by independent methods. For the infrared/optical fit all the X-rays parameters are considered fixed, therefore, R_{wd} is not a fitted parameter for this range of energy. The 1σ uncertainties for the last digit for the fitted parameters are between parenthesis.

Parameter	Description	Value
X-rays		
FIXED PARAMETERS		
d (kpc)	distance of 4U 0142+61	2.57
N_H (10^{21} cm $^{-2}$)	columnar density of hydrogen	6.4
T_{brem} (keV)	temperature of the emission for the accretion column	670.3
FITTED PARAMETERS		
EM (10^{56})	emission measure	1.49 (40)
χ^2_{brem}/dof	reduced chi square for the hard X-rays	0.86
T_{spot1} (keV)	temperature of the spot 1	0.336 (11)
R_{spot1} (10^5 cm)	radius of the spot 1	9.49 (48)
T_{spot2} (keV)	temperature of the spot 2	0.632(32)
R_{spot2} (10^5 cm)	radius of the spot 2	1.62 (28)
χ^2/dof	reduced chi square for the soft X-rays	1.05
DERIVED PARAMETERS		
T_{shock} (keV)	temperature of the shock front	1047.3
M_{wd} (M_\odot)	mass of the white dwarf	1.41
R_{wd} (10^5 cm)	radius of the white dwarf	1.021
L_s (10^{35} erg.s $^{-1}$)	bolometric luminosity due to the soft blackbodies	2.03
L_h (10^{35} erg.s $^{-1}$)	bolometric luminosity due to bremsstrahlung	2.84
L_X (10^{35} erg.s $^{-1}$)	bolometric total accretion luminosity	4.86
\dot{M} (10^{17} g.s $^{-1}$)	accretion rate	2.66
R_{brem} (10^5 cm)	radius of the hard X-ray emission	9.62
H (10^4 cm)	height of the accretion column	4.47
n_e (10^{19} cm $^{-3}$)	electrons number density	3.38
Optical/Infrared		
FITTED PARAMETERS		
T_{wd} (10^5 K)	effective temperature of the white dwarf	2.87(28)
T_{in} (K)	inner temperature of the debris disk	1937(170)
T_{out} (K)	outer temperature of the debris disk	120(109)
DERIVED PARAMETERS		
R_{in} (R_\odot)	inner radius of the debris disk	1.14
R_{out} (R_\odot)	outer radius of the debris disk	47

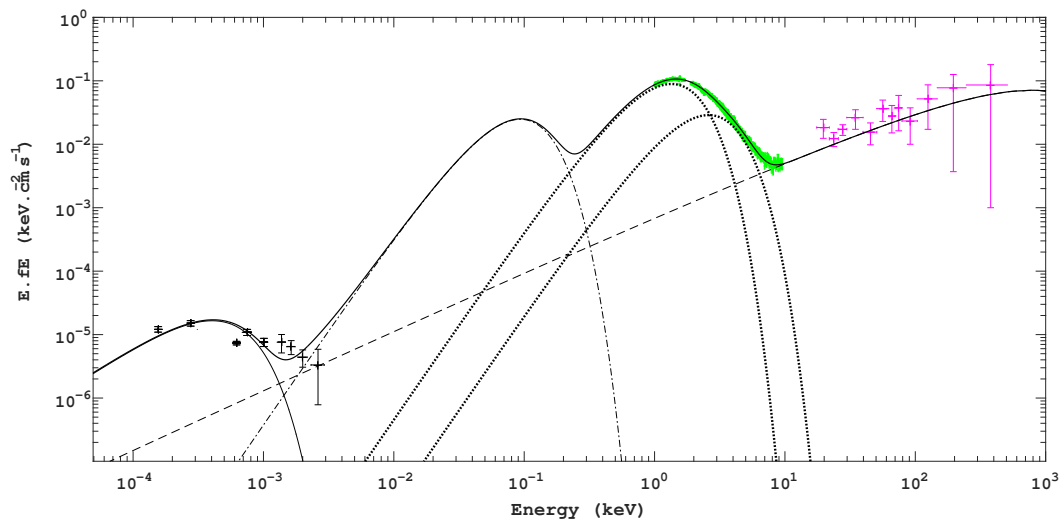


FIGURE 5.3 – Complete SED of 4U 0142+61 for the WD accreting model. The bold black curve is the complete fit; the filled curve is the disk component; the dot-dashed curve is the WD photosphere; the dotted curves are each one of the hot spots components; and the dashed curve is the bremsstrahlung component. The observational data of 4U 0142+61 is the same from Figure 3.7.

Finally, Figure 5.8 shows the scatter plot for the three fitted parameters of the optical/infrared energy range.

5.2 Discussions

5.2.1 Post-shock region and hot spots

Wang *et al.* (2014) tried for the first time to fit the hard X-rays of 4U 0142+61 with a bremsstrahlung component and found a poor fit, with a reduced χ^2 of 4.03. However, they used the XSPEC 12.6.0q, which uses a non-relativistic Gaunt factor derived from Karzas & Latter (1961) and Kellogg *et al.* (1975). Conversely, we used the relativistic Gaunt factor from Nozawa *et al.* (1998), which, depending on the energy range, can differ from the non-relativistic prescription by orders of magnitude (see Fig.4.3).

Moreover, we use a composition of carbon opposed to the 92.5% of hydrogen and 8.5% of helium and applied the relativistic correction for high temperatures. All those differences in the methodology allow us to fit consistently the data with a bremsstrahlung component and generate a natural the cutoff for the model of $\sim kT_{brem}$, in agreement with the observed cutoff of 279_{-41}^{+65} (Wang *et al.*, 2014; Olausen; Kaspi, 2014).

To fit the data, we use high values of temperature for the accretion structure. The kT_{brem} for our model is 670.3 keV, larger than kT_{brem} for any known cataclysmic variables.

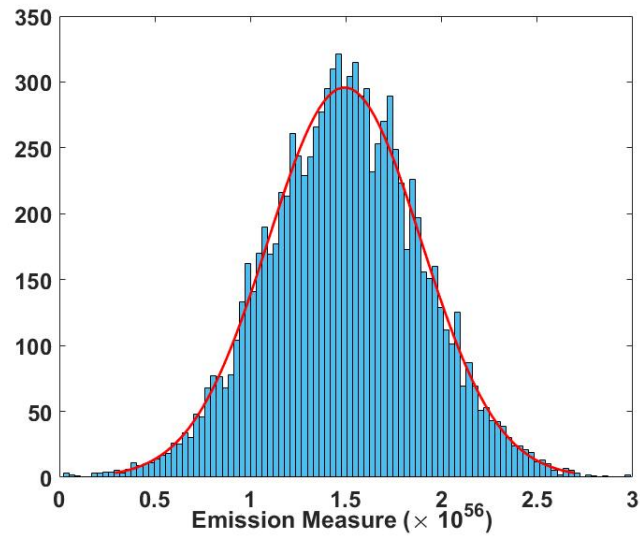


FIGURE 5.4 – Markov chain Monte Carlo distribution of EM for a fixed temperature of 670.3 keV. The blue bars are the histogram distribution of EM and the red line is the best Gaussian. The error in EM is the 1σ Gaussian.

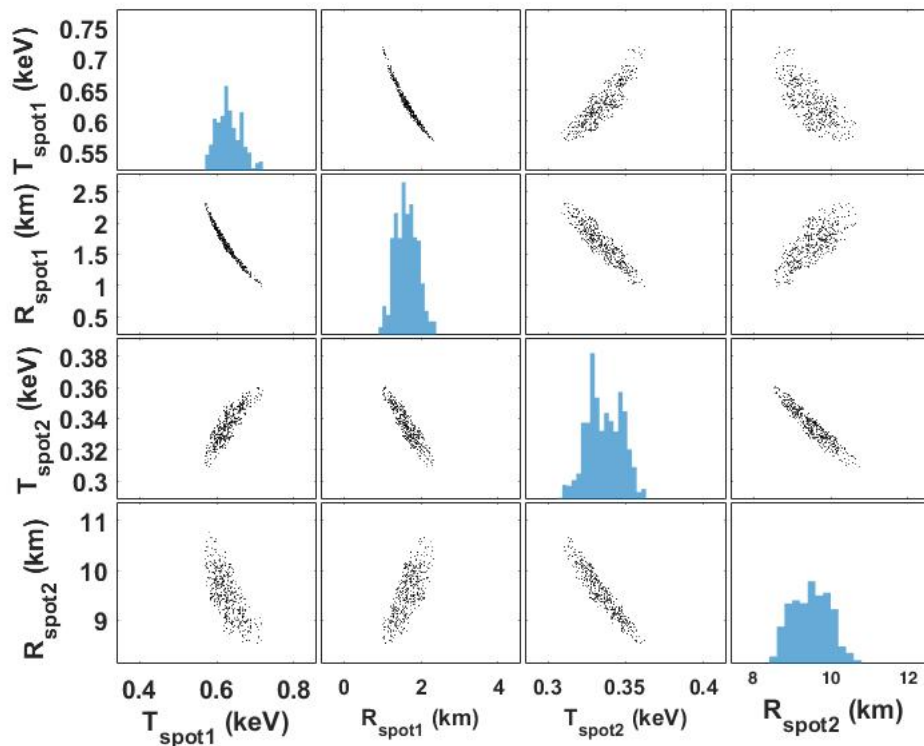


FIGURE 5.5 – Scatter distribution of the soft X-rays fitted parameters T_{spot1} , R_{spot1} , T_{spot2} and R_{spot2} .

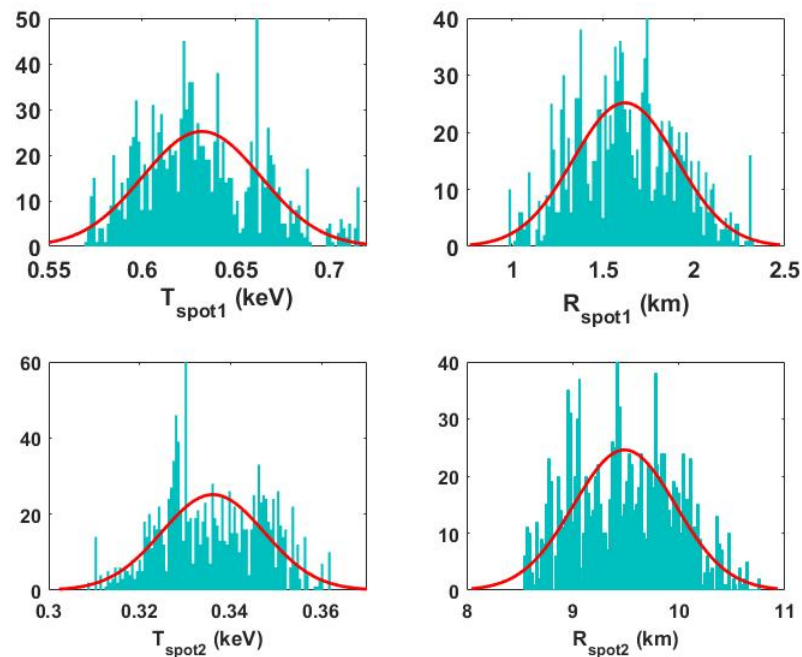


FIGURE 5.6 – Markov chain Monte Carlo distribution of the soft X-rays fitted parameters T_{spot1} , R_{spot1} , T_{spot2} and R_{spot2} . The blue region are the histogram distribution of each parameter and the red line is the best Gaussian. The error is the 1σ Gaussian

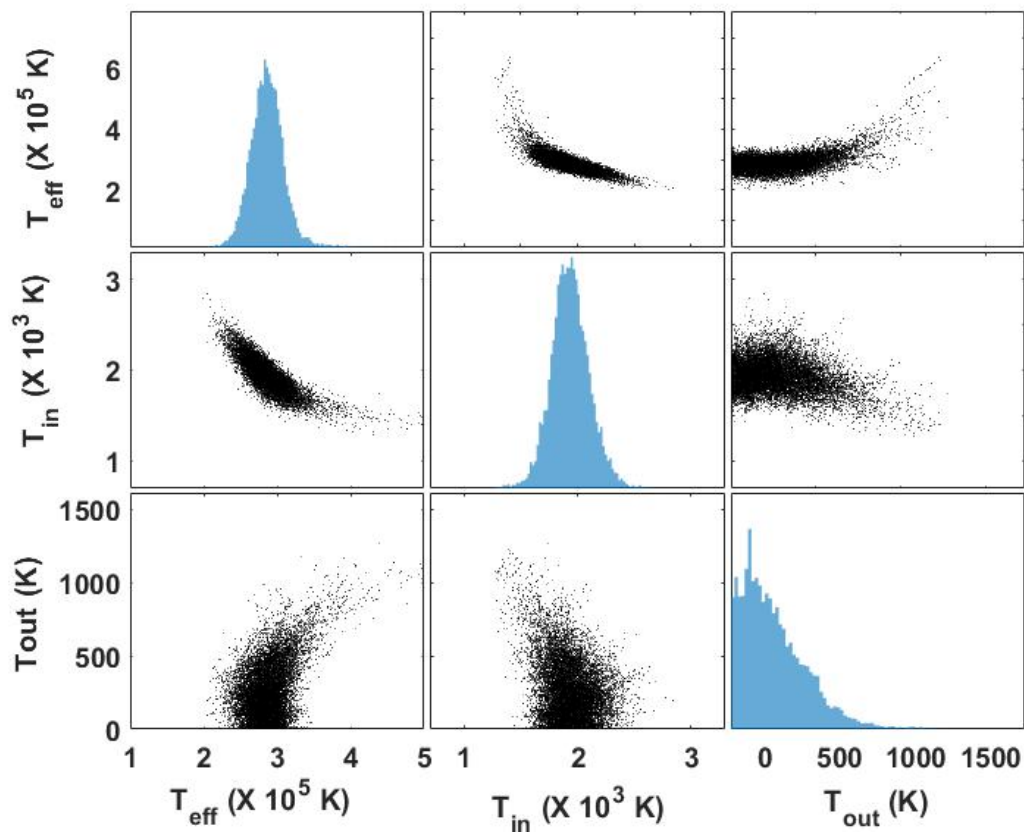


FIGURE 5.7 – Scatter distribution of the optical fitted parameters T_{wd} , T_{in} and T_{out} .

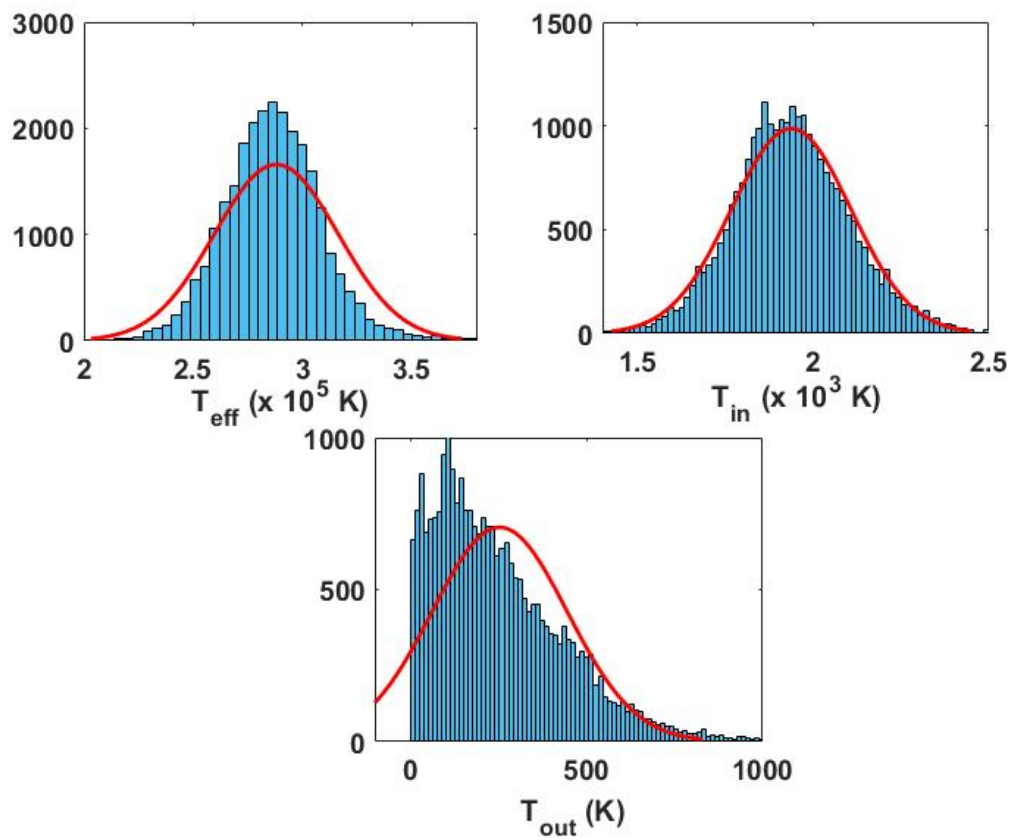


FIGURE 5.8 – Markov chain Monte Carlo distribution of the optical fitted parameters T_{wd} , T_{in} and T_{out} . The blue region are the histogram distribution of each parameter and the red line is the best Gaussian. The error is the 1σ Gaussian

The bremsstrahlung temperature of known accreting white dwarfs can reach a few tenths of keV, such as the Intermediate Polars (IPs) V709 CAS (94.5 keV) and NY Lup (78.8 keV) (Yuasa *et al.*, 2010). However, those higher values are theoretically possible for a massive WD (see eq. 4.19). Plus, an in-falling matter composed by carbon and oxygen increases the mean molecular weight, which also increases the temperature.

Furthermore, Belloni *et al.* (2019) have implemented a shock solution for accreting WDs. Their results show that shock temperature as high as 1000 keV can be found for massive WDs (see Fig. 5.9), which corroborates the temperature of our fitting.

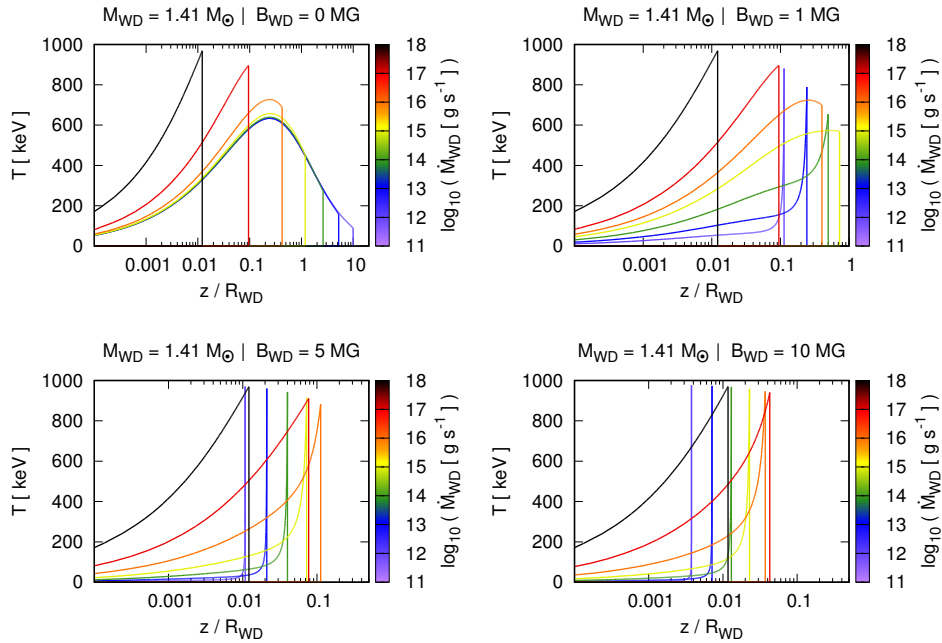


FIGURE 5.9 – Post-shock structure for a $1.41 M_{\odot}$ WD for 4 different magnetic field strengths. Reference: Belloni (2018).

5.2.2 White-dwarf photosphere

The temperatures of the WD photosphere for the model for 4U 0142+61 is very high ($T_{wd} = 287,000$ K). Werner & Rauch (2015) presented two extremely hot white dwarfs, H1504+65 ($T_{wd} = 200,000$ K and $M = 0.83 M_{\odot}$) and RXJ0439.8-6809 ($T_{wd} = 250,000$ K and $M = 0.86 M_{\odot}$). Both of them are colder than our models. However, supposing a blackbody emission for the photosphere, we also compared the emitted luminosity of those two sources with our model. The results are in Table 5.2 and show that the luminosity of the photosphere of 4U 0142+61 in our model is smaller than those two white dwarfs.

From the effective temperature we can estimate the age of the WD. The Mestel cooling law (Mestel, 1952) was the first to attempt such estimate. Hurley & Shara (2003) presented

TABLE 5.2 – Luminosity of photosphere

Parameter	4U 0142+61	RXJ0439.8	H1504
R_{wd} (km)	1021	10400	10400
T_{wd} (10^5 K)	2.87	2.5	2.0
$\log(L_{wd}/L_{\odot})$	1.12	2.5	2.9

an improved version of his cooling law (eq. 5.1):

$$L = \frac{bMZ^{0.4}}{(A(t + 0.1))^x}. \quad (5.1)$$

In this equation L is the bolometric luminosity of the WD photosphere (eq. A.24) in solar units, M is the WD mass in solar units, A is the average atomic number, t is the time and Z is the metallicity. The pair $(b; x)$ is dictated by equation 5.2:

$$(b; x) = \begin{cases} (300; 1.18) & , \text{ for } t < 9000 \text{ Myr} \\ (300(9000A)^{5.3}; 5.48) & , \text{ for } t > 9000 \text{ Myr}. \end{cases} \quad (5.2)$$

In general, the metallicity is considered to be ~ 0.02 . Different values were always neglected because heavy elements tends to sink from the surface (Hurley; Shara, 2003). However, depending on the mass of the progenitor of the WD, the amount of metals in the surface can change significantly. For instance, for a $8.0 M_{\odot}$ main-sequence star, Z is 0.02 and for $6.8 M_{\odot}$ Z is 0.0001. Rueda *et al.* (2013) uses $Z=0.001$ to estimate the age of 4U 0142+61 in the WD pulsar model.

We consider the core composition of 60% carbon and 40% oxygen, $t < 9000$ Myr and $Z = 0.001$ (Althaus *et al.*, 2010; Rueda *et al.*, 2013). This results in a cooling age of 31 kyr.

5.2.3 Debris Disk

The inner temperature of the debris disk is 1937 K (see Table 5.1), larger than the silicate sublimation temperature (T_s) of about 1300-1500 K (Lodders, 2003). However, this T_s is based on the solar abundance and is mainly used to model protoplanetary disk of young stars. Rafikov & Garmilla (2012) argues that those values of T_s provide underestimated values of T_{in} for disk around WDs once the composition and behavior of this disks are distinct from those around young stars. In fact, some WDs have T_{in} larger than 1500 K, such as HE 1349-2305 (Girven *et al.*, 2012) and GD 56 (Farihi *et al.*, 2009), both with $T_{in} = 1700$ K. Moreover, according to Rafikov & Garmilla (2012), T_{in} is larger for WD with higher accretion rates and T_{WD} , which justify the larger T_{in} of 4U 0142+61

compared to T_{in} for other isolated WDs.

Once we consider the debris disk opaque, we can estimate the minimum mass of the dusty region of the disk using the approach from Jura (2003). The surface area of the dusty region is $\sim 3.4 \times 10^{25} \text{ cm}^2$ for our model. Rafikov & Garmilla (2012) states that the particle size of debris disk around WD can varies from 0.03 to 30 cm. Thus, if we consider a 10 cm diameter particles, the opacity is 0.05 g.cm^{-2} at $15 \mu\text{m}$ (Ossenkopf *et al.*, 1992), resulting in a minimum is $\sim 10^{26} \text{ g}$.

In Chapter 6, we discuss the possible merger origin for 4U 0142+61 in our model. In this case, the mass of the disk just after the coalescence is $\sim 10^{32} \text{ g}$. The amount of mass for the age in our model depends on the evolution of accretion rate. If we consider that the accretion rate was always above the Eddington limit, we find that the mass of the disk is almost unchanged, once the cooling age is too short. Comparing both mass values, we find that the expected mass for the disk is 10^5 times larger than the minimum estimated mass of 10^{26} g .

5.2.4 Optical pulsed fraction

As discussed in Chapter 3, 4U 0142+61 have periodic variability in the X-rays and optical wavelengths. In this thesis, we only focused into explain the quiescent emission of this source. This way, we are only going to discuss the most probable origin of this pulsation whereas the fit of the pulsed profiles of Figures 3.3 and 3.5 are left for a further study. The nature of the pulsed emission for the X-ray wavelengths are easily explained by a geometric features, since the hot spots and accretion columns are eclipsed by the WD in every cycle of rotation. The cause for the optical pulsation, however, is more blur. In the magnetar model, this pulsation was thought to be magnetospheric (Kern; Martin, 2002), however, any component of the model presented by Hascoët *et al.* (2014) extends up to the optical range. The NS accreting model states that the pulsed fraction could be cause by outer gaps in the pulsar magnetosphere operating with a disk inside (Ertan; Cheng, 2004) and the WD pulsar model did not explain such feature in any of their articles.

For our model, the disk nor the WD photosphere do not have pulsed behavior. Therefore, the pulsed fraction of 4U 0142+61 must be explained by the tail of the bremsstrahlung component (see Fig. 5.2). This way, the expected pulsed fraction caused for our model is $\sim 20 \%$ for the I band whereas the observational pulsed fraction is this band is $27_{-6}^{+8} \%$ (Kern; Martin, 2002).

5.3 Spin-down, propeller regime and the magnetic field

4U 0142+61 is a fast white dwarf slowing down. Thus, for our model to be feasible we need to reproduce the observational spin-down for an accreting regime using realistic parameters. In this section, we estimate the possible magnitude of the magnetic field of 4U 0142+61 to reproduce the spin-down for an accreting regime.

The corotational radius is the disk position in which the particles rotational velocity is equal to stellar rotation. According to Ekşi *et al.* (2005), the corotational radius (R_c), given by eq. 5.3 must be larger than both R_{wd} and R_m for the system to be in the accretor region. In eq. 5.3, $\omega = 2\pi/T$ is the angular velocity. Fast white-dwarf rotators are candidates to be propellers. In fact, the nature of the intermediate polar AE Aqr is still a question for debate. Some authors argue that this fast spinner, with a 32 s period, is a propeller (Wynn *et al.*, 1997). Others defend that AE Aqr emission is consistent with an accreting regime (Kitaguchi *et al.*, 2014). Moreover, R_m must be larger than R_{wd} for the accretion to be magnetic and create spots.

$$R_c = \left(\frac{GM_{wd}}{\omega^2} \right)^{1/3}. \quad (5.3)$$

If we consider only the accretion of matter onto the WD, we would have spin-up. However, it is possible for the WD to spin-down in the accretor regime if other spin-down mechanisms compensate that increase due to accretion. In fact, some cataclysmic variables are known to be slowing down, such as the IPs FO Aqr, PQ Gem, V 1223 Sgr and AE Aqr. This spin-down effect can be driven by some mechanisms such as the coupling between the magnetic field and the disk or the misalignment of the magnetic field with the rotation axis.

García-Berro *et al.* (2012) argues that the alignment of the magnetic field onto the spin axis can be the main cause of the spin-down for merger remnants. That spin-down effect, calculated by equation 5.4, is more prominent on white dwarfs that are the product of a merger of two white dwarfs with different masses, once the misalignment between the magnetic field and the spin axis is larger in that case (García-Berro *et al.*, 2012). The parameters μ (G.cm³) and I (g.cm²) are the magnetic moment and the moment of inertia.

$$\dot{\Omega}_{mag} = \frac{2\Omega^3 \mu^2}{3Ic^3} \sin^2 \beta. \quad (5.4)$$

The sum of accretion and coupling spin change can be calculated by equation 5.5 Warner (2003). $n(\omega_s)$ can be obtained in Wang (1987), where $\omega_s = R_m/R_c$. In this case,

the equation consider for both the components, the coupling between the magnetic field and the disk and the matter falling into to the central remnant. In this model, it is possible to spin-down if the relation between the magnetosphere radius and the corotational radius is in the range of 0.975 to 1.0 (Wang, 1987).

$$\dot{\Omega}_{coup} + \dot{\Omega}_{acc} = \frac{2\pi\dot{M}R_c^2}{PI}n(\omega_s). \quad (5.5)$$

Finally, 4U 0142+61 can present a propeller behavior in its early years, specially if the accretion rate was not high. Equation 5.6 represents the propeller spin-down contribution (Alpar, 2001).

$$\dot{\Omega}_{prop} = -\frac{\mu^2}{IR_m^3}. \quad (5.6)$$

The total spin-down is given by the eq. 5.7.

$$\dot{P} = \frac{-P^2}{2\pi}(\dot{\Omega}_{prop} + \dot{\Omega}_{acc} + \dot{\Omega}_{mag}). \quad (5.7)$$

The propeller regime causes a high spin-down that is capable to reproduce the observed spin-down of $2 \times 10^{-12} \text{ s.s}^{-1}$. However, our main hypothesis is that the object presents accretion. Thus, 4U 0142+61 must have $R_c > R_m > R_{wd}$ and a spin-down in the order of $10^{-12} \text{ s.s}^{-1}$ for our model to be plausible.

Moreover, the inferred value of magnetic field to reproduce the spin-down must be consistent a single-temperature bremsstrahlung scenario. Depending on the nature of the white dwarf and its accretion structure, different types of radiative processes could be predominant (Lamb; Masters, 1979). For bremsstrahlung dominate instead of cyclotron emission, the magnetic field (B) has to be smaller than $6 \times 10^6 (L_f/10^{36} \text{ erg.s}^{-1})^{2/5}$, where L_f is L_X divided by f . Considering R_{spot1} , R_{spot2} and R_{wd} , we have $f \sim 8.85 \times 10^{-5}$, which gives an upper limit for B of $1.87 \times 10^8 \text{ G}$.

If we consider I in the order of 10^{48} g.cm^2 and $\beta = 90^\circ$ (rotation and magnetic lines are completely misaligned, which gives the highest spin-down for this case), we have an \dot{P}_{mag} of $4.45 \times 10^{-17} \text{ s.s}^{-1}$ much smaller than the observed spin-down of 4U 0142+61. Therefore, P_{mag} is not able to reproduce the spin-down and can be neglected.

Thus, we need to reproduce the spin-down solely by equation 5.5, which gives $0.975 < R_m/R_c < 1$. This way, if we reproduce the spin-down by eq. 5.5, we will also prove the assumption that $R_c \sim R_m$ we use to estimate T_{shock} by eq. 4.19. For $\beta = 90^\circ$ we must have $B = 3.91 \times 10^7 \text{ G}$ to reach the $2 \times 10^{-12} \text{ s.s}^{-1}$. Conversely, if we consider $\beta = 0^\circ$, we must have $B = 7.82 \times 10^7 \text{ G}$. Thus, the magnetic field range in the WD accreting model is

$3.91 \times 10^7 < B < 7.82 \times 10^7$ G. Those values are consistent with the upper limit imposed by the bremsstrahlung emission. Moreover, this spin-down requires $R_m/R_c = 0.995$, which is extremely close but still consistent with the criteria to be in the accreting regime.

Moreover, we can compare our evaluation of B with measured values of magnetic WDs. The magnetic WDs are separated in two main classes: the cataclysmic variables (CVs) and the isolated WDs. Moreover, the magnetic CVs can be polar or IPs. For polars the magnetic field varies from 7 MG (V2301Oph) up to 160 MG (AR UMa). Meanwhile IPs have magnetic field of ~ 5 -20 MG, with the highest value of ~ 30 MG for V405Aur (Ferrario *et al.*, 2015). For isolated WDs, the magnetic field can range from 10^3 G to 10^9 G. In the range of 10^7 G, we have several examples of isolated WDs. For instance, WD 0806+376 has a field of 3.79×10^7 G and WD 1017-367 has a field of 6.5×10^7 G (Ferrario *et al.*, 2015, see also Fig.6.3). Thus, our estimate of magnetic field is consistent with both classes of magnetic CVs.

In appendix B we use $0.975 < R_m/R_c < 1$ to estimate the magnetic field for other SGR/AXPs in the accreting WD model. Those estimates are also consistent with the magnetic field of magnetic WDs.

6 Merger of white dwarfs

If this accreting white-dwarf model is correct, 4U 0142+61 is a fast-spinning, isolated, magnetic, hot and extremely massive white dwarf. Even though those characteristics are very uncommon for an white dwarf, sources with similar characteristics have already been observed. RE J0317-853, for example, is in an binary system without any interaction with the secondary. This object has a period of 725.4 s, a estimated mass of $1.35 M_{\odot}$, an effective temperature of ~ 50.000 K and magnetic field of 340 MG (Barstow *et al.*, 1995). The most plausible origin for that source is the merger of two less massive CO white dwarfs (Ferrario *et al.*, 1997).

Even though, no WD merger event was observed, there are some strong evidences of its existence. For instance, it is one of the most plausible scenarios to explain why magnetic isolated WDs are more massive than the non-magnetic ones (García-Berro *et al.*, 2012). Non-magnetic WDs have a mean mass of $0.663 \pm 0.136 M_{\odot}$, while magnetic WDs (considering field between 10^6 G and 10^9 G) have an average value of $0.784 \pm 0.047 M_{\odot}$ (Ferrario *et al.*, 2015). Figure 6.1 shows the comparison of the mass distribution between magnetic and non-magnetic WDs. Furthermore, by looking at Figure 6.1, we can note a higher concentration of magnetic white dwarfs with mass greater than $1 M_{\odot}$ for the magnetic sample.

Furthermore, recent *Gaia* observations in the neighborhood (~ 100 pc) show the presence of a substantial amount of massive WDs and a bifurcation in the color magnitude diagram that are consistent with a merger formation (Kilic *et al.*, 2018). Also, Toonen *et al.* (2017) analyzed the sample of WD within 20 pc and show that the amount of WDs in double WD systems ($\sim 25\%$) are smaller than the percentage of solar-type main sequence stars in double systems ($\sim 50\%$). They conclude that this discrepancy is consistent with the coalescence of WD binary system and that about 10-30 % of all isolated WD should be result of a merger. Thus, not only the merger scenario is a possibility but also is one of the best interpretations for several objects and general properties of the WD samples.

This merger can occur between WDs with different core compositions and leads to several final results (Dan *et al.*, 2014). In all of those scenarios our main interest is in a near-Chandrasekhar mass product (see sec. 5.1). In this sense, the following sections aims

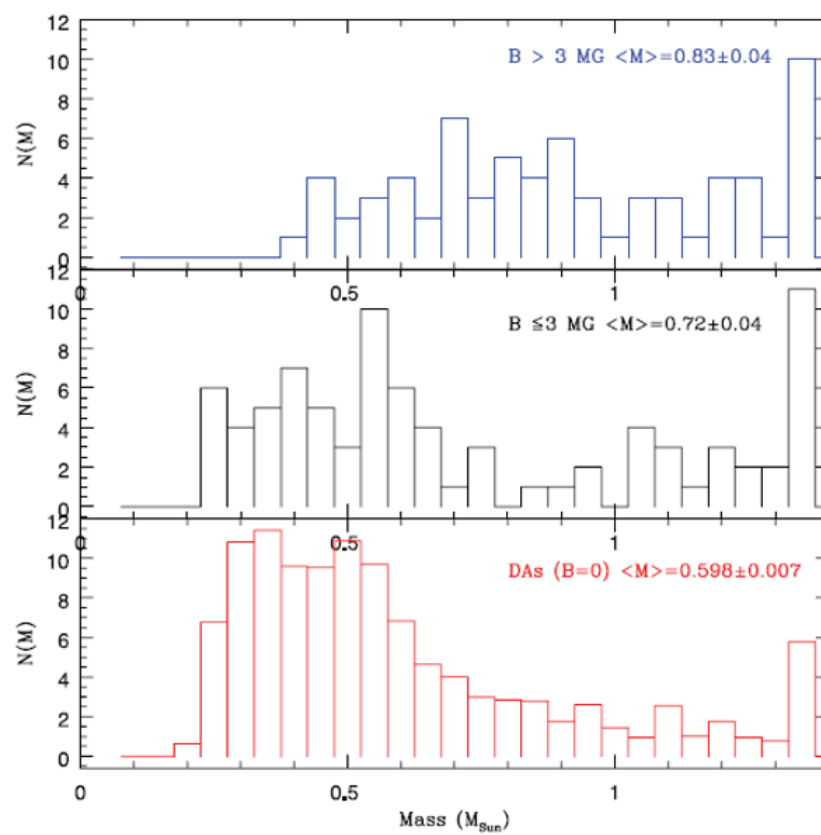


FIGURE 6.1 – Mass distribution histogram for magnetic and non-magnetic WDs. Reference: Kepler *et al.* (2013).

to summarize and discuss several characteristics of the remnant of this coalescence event for later comparison with our model.

6.1 Post-merger configuration

The merger of two WDs can lead to numerous final configurations. Those possible remnants are concisely presented in Figure 6.2. In our case, the most interesting product is the near-Chandrasekhar WDs (salmon and green regions from Fig. 6.2). In the following paragraphs we summarize the most important papers for this coalescence outcome.

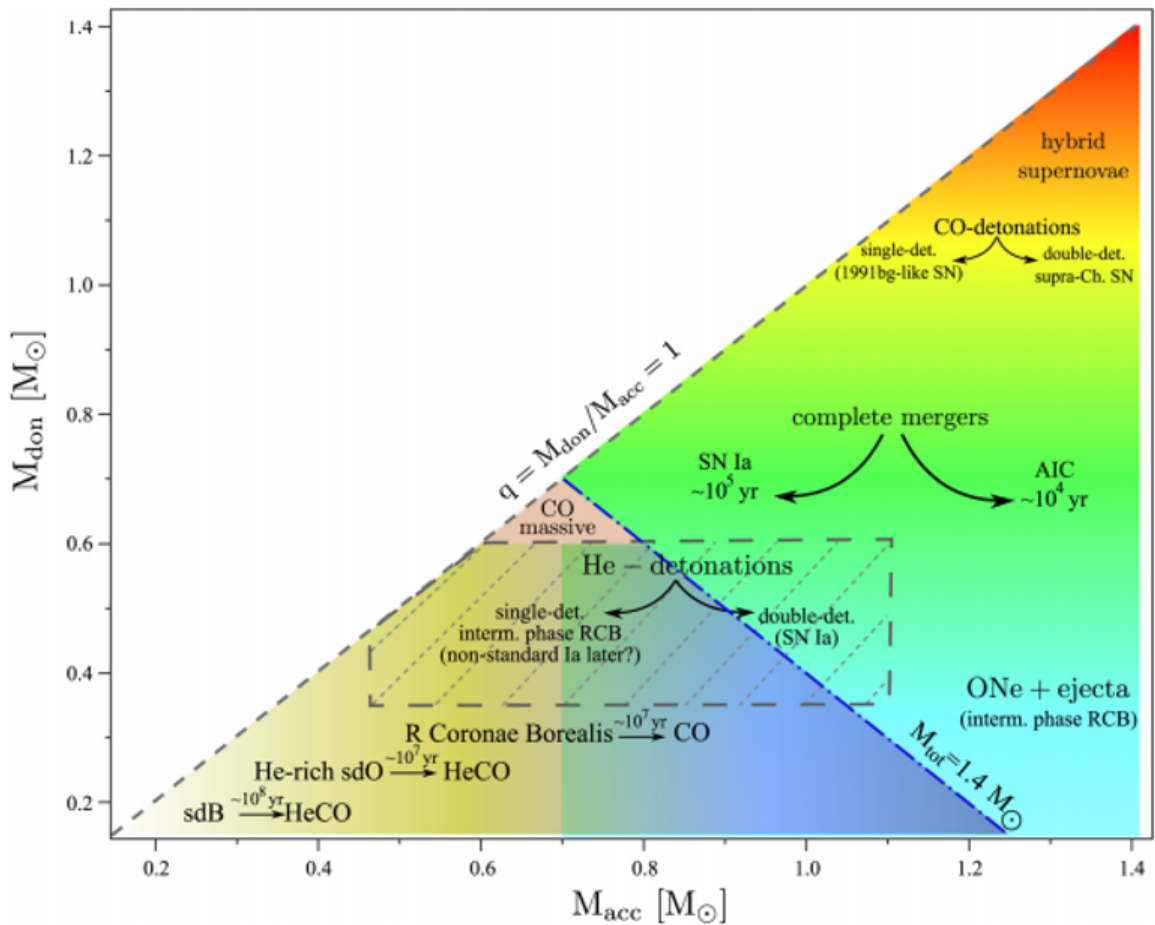


FIGURE 6.2 – Diagram of the final product of the coalescence by the mass of each WD progenitor. Each color in the mass-mass diagram represents the final outcome: HeCO core WD (brown); CO core WD (dark blue); ONe core WD (light blue); massive CO core WD (salmon); neutron star after some time (green); neutron star during the coalescence (yellow); small-mass black hole (red). The shaded area is the region where He detonations can occur. sdB (or sdO) = He-rich hot sub-dwarf of spectral type B (or type O); RCB = R Coronae Borealis stars; SN Ia = supernova Ia; AIC = auto-induced collapse. Reference: Dan *et al.* (2014)

There is no consensus about the merger product. Some properties, however, are con-

stant in all simulations. For instance, the remnant consists in a cold core formed by the primary, a hot envelope made by a fraction of the secondary mass and a Keplerian disk containing the remaining of the secondary (Yoon *et al.*, 2007; Lorén-Aguilar *et al.*, 2009; Raskin *et al.*, 2012). Just a little amount of mass is ejected of the system, about $10^{-3}M_{\odot}$ (Lorén-Aguilar *et al.*, 2009). Thus, almost all mass remain in the central remnant or in the disk. The exact percentage of the secondary in the disk varies according to the mass of the progenitors. According to simulations, a good estimate for this percentage is 50% of the less massive progenitor (Becerra *et al.*, 2018), which gives a initial mass of the disk in the order of $10^{-1} M_{\odot}$.

This newborn WD is also expected to have a short period right after the coalescence. Becerra *et al.* (2018) and Raskin *et al.* (2012) state that the remnant (cold core+envelope) spins as a rigid body. In contrast, Yoon *et al.* (2007) argue that the cold core rotates as a rigid body whereas the envelope spins deferentially leading the photosphere to present almost a Keplerian angular velocity. This differential rotation, however, vanishes quickly and the remnant eventually starts to rotate uniformly.

It is also expected the growth of a magnetic field during the coalescence and in the early years after the merger. García-Berro *et al.* (2012) studied the grown of the magnetic field after the coalescence and its importance in the evolution of the remnant. Huge magnetic fields can be developed in the post-merger scenario. The hot, convective and differential rotating corona can generate the field values we observe in isolate WDs. Moreover, that magnetic field does not decay over time neither is transferred from the corona to inner layers of the remnant nor to the disk. Ji *et al.* (2013) treated, for the first time, the possibility of the grown of the magnetic field right after the merger phase. At first, the two $0.6\text{-}0.6 M_{\odot}$ WD progenitors are weakly magnetized. The product is a rotating $0.96 M_{\odot}$ remnant + $0.04 M_{\odot}$ hot corona. Magneto-rotational instability (MRI) in the disk leads to the rapid growth of an weak magnetic field in the disk and, after several inner rotational periods, this MRI developed in the disk and the magnetic flux is advected into the remnant. They used a model of *alpha* prescription to model the evolution of the disk, that can leads to center carbon ignition. Later, Zhu *et al.* (2015) shows that the field can be amplified during the coalescence by Kelvin–Helmholtz instability-generated vortices. They found that the magnetic field in the core of this newborn $0.64 M_{\odot}$ WD, surrounded by a thermally supported envelope $0.42 M_{\odot}$ + disk $0.21 M_{\odot}$, can achieve values $> 10^{10}$ G and have a very complex geometry.

All those previous properties - presence of the disk, small spin period and huge magnetic field - are consistent with the observations of 4U 0142+61 . Thus, if the accreting white-dwarf model for 4U 0142+61 is correct, this object is probably a young product of a merger of two less massive CO WDs.

6.2 Accretion onto the merger remnant

The remnant is expected to accrete matter from the disk during its early years. However, how the disk and the accretion rate evolve is still question for debate. Külebi *et al.* (2013) argues that the disk is viscous supported and can be described by the α formalism of Shakura & Sunyaev (1973). The dynamic of the viscous supported disk evolves following equation 6.1. The accretion rate and the outer radius of the disk are given by equations 6.2 and 6.3. The viscous timescale is given by equation 6.4. According to Külebi *et al.* (2013), α is 19/16 if electron scattering dominates and 5/4 for the bound-free regime. Those two values are very close and chose one or another not affect the results substantially.

$$\frac{\partial \Sigma}{\partial t} = \frac{3}{r} \frac{\partial}{\partial r} \left[r^{1/2} \frac{\partial}{\partial r} \left(\nu \Sigma r^{1/2} \right) \right]. \quad (6.1)$$

$$\dot{M} = \dot{M}_0 \left(1 + \frac{t}{t_0} \right)^{-\alpha}. \quad (6.2)$$

$$R_{out} = r_0 \left(1 + \frac{t}{t_0} \right)^{2\alpha}. \quad (6.3)$$

$$t_0 \sim 15s \left(\frac{j_0}{10^{18} cm^2 s^{-1}} \right)^{25/7} \left(\frac{M_0}{10^{-1} M_\odot} \right)^{-3/7}. \quad (6.4)$$

For that accretion model, the accretion rate in the beginning is much larger compared to the thermal supported scenario (see below), up to $10^{-1} M_\odot.s^{-1}$ (Becerra *et al.*, 2018) and drops exponentially by equation 6.2. For those high accretion rates, 4U 0142+61 would spin-down in the first years and would probably break (Külebi *et al.*, 2013). Therefore, we do not consider this evolutionary hypothesis.

Conversely, Yoon *et al.* (2007) argue that the disk is more likely to be thermal-pressure supported. In this case, the accretion rate can be estimated by equation 6.5 (Becerra *et al.*, 2018), where τ_ν (eq. 6.6) and $\tau_{thermal}$ (eq. 6.7) are the neutrino and thermal cooling time (Henyey; L'Ecuyer, 1969; Becerra *et al.*, 2018). The accretion rate is about $10^{-7} M_\odot.yr^{-1}$ in the beginning, when neutrino cooling dominates.

$$\dot{M} = \frac{M_{disk}}{\min(\tau_\nu, \tau_{thermal})}. \quad (6.5)$$

$$\tau_\nu = \frac{c_v T_s}{\epsilon_\nu} \Big|_s. \quad (6.6)$$

$$\tau_{thermal} = \frac{3}{64\sigma} \left(\int_{\Delta r} \left(\frac{\kappa c_v}{T^3} \right)^{1/2} \rho dr \right)^2. \quad (6.7)$$

Considering the initial spin period of about 2.5 s (Becerra *et al.*, 2018) and accretion rate of $10^{-7} M_\odot \cdot \text{yr}^{-1}$, we have $R_m > R_c$ in the early years. Thus, the remnant initially would pass through a propeller phase. This propeller phase spin-downs the remnant, protecting it from breaking. Moreover, the lack of accretion would avoid carbon ignition, center or off-center. As a consequence of the spin-down, the period and the corotational radius tend to increase thus enabling the white dwarf to accrete matter from the disk. The accretion rate dropped until it achieved the current $\sim 10^{-9} M_\odot \cdot \text{yr}^{-1}$.

How this very massive white dwarf would evolve after the accretion starts is a hard task, since neither the evolution for the post-merger product nor the fate of very massive accreting white dwarfs are well understood. In either case, 4U 0142+61 would be a strong candidate to become a neutron star, by collapse or SN Ia.

SN Ia are extremely bright standard candles. Thus, they are essential for measuring cosmological distances. However, the origin of SN Ia is still not well known and several models have been proposed (Maoz *et al.*, 2014). The most accepted model is the single degenerate (SD), in which a CO WD increases its mass by accretion (Maoz *et al.*, 2014). Eventually, when this WD reaches the Chandrasekhar limiting mass, it explodes as a supernova. The most important candidates for the SD model are the Super-Soft Sources (SSS). The amount of SSS, however, are not enough to explain the rate of SN Ia explosions.

In this context, the double degenerate (DD) model raises in the attempt to explain part or all SN Ia events (Maoz *et al.*, 2014). The DD model points out that the merger of two CO WDs could lead to a supernova event during the coalescence (yellow region of Figure 6.2) or after some time (green region). There are several studies about the merger of CO WDs in the SN Ia context (van Kerkwijk *et al.*, 2010; Dan *et al.*, 2014; Becerra *et al.*, 2018, e.g.). In this case, the parameters that lead to a SN Ia event are quite complex and mainly depend on the remnant mass and on the evolutionary model for the disk.

Moreover, Maoz *et al.* (2014) discuss the possibility that SGR/AXPs as WD pulsars were good candidates for SN Ia. In this case, the rapid rotation delays the explosion (Saio; Nomoto, 2004), in a similar mechanism to the "spin-up/spin-down" SN Ia model. The spin-down effect leads the WD to smoothly decrease the rotation period and, consequently, to lose stability. Eventually, the WD would present a center carbon explosion.

For our model, the in-falling matter can also disturb its stability. Saio & Nomoto

(2004) argue that a white dwarf with the same origin of 4U 0142+61 would not explode as a SN Ia because it would inevitably become a ONeMg WD. In this case, the accretion could lead 4U 0142+61 to exceed the limiting mass and become a neutron star by carbon deflagration collapse (Nomoto; Kondo, 1991). However, they consider a 10^{-5} - $10^{-6} M_{\odot} \cdot \text{yr}^{-1}$ and do not take into account the effect of the magnetic field nor the spin period, which are essential parameters to predict the evolution of WD merger products.

Conversely, Yoon *et al.* (2007) considered an accretion rate smaller than $10^{-6} M_{\odot} \cdot \text{yr}^{-1}$ (which is consistent with our findings and with a thermal supported disk) and take into account the spin period. They found that the remnant of two CO WD can lead to a SN Ia after $\sim 10^5$ yr. Moreover, Becerra *et al.* (2018) simulate the evolution of a $1.45 M_{\odot}$ WD remnant for a thermal pressure supported disk. For a 10^7 G magnetic field (see. sec 5.3), the object would suffer a carbon ignition after about 5×10^4 yr. Therefore, the age to explode as a SN Ia is consistent with the derived cooling age. Thus, for the WD accreting model, 4U 0142+61 is a good candidate to explode as a SN Ia in a small amount of time.

6.3 Magnetic isolated WDs

The magnetic field plays an essential role in the evolution of the remnant. For instance, the magnitude of the field is essential to describe how the spin-down evolve (see sec. 5.3). Even though merged WDs have always been thought to be magnetic, the first simulations of the coalescence and later remnant evolution didn't consider any magnetic field. This dichotomic reality was consequence of the forbidden computational price to run magneto-hydrodynamics simulations years ago. Even today, only a few works consider such fields.

Furthermore, the spin period changes (see sec.5.3). On the other hand, the magnetic field is thought to remain the same. For that reason, the magnetic isolated WDs is the best class to find merger remnant candidates.

For all those reasons it is important to understand the class of magnetic isolated WDs. The current percentage of magnetic WD onto the total amount of WDs is about 20% for samples limited in volume. For samples up to a specific apparent magnitude this value is ~ 8 . The search for magnetic WDs performed mainly by the SDSS, HQS and the Cape Survey groups increased the number of known magnetic WDs (2-1000 MG) from approximately 70 in the early 2000s to more than 600 sources (Ferrario *et al.*, 2015). Thus, today we have a reasonable amount of magnetic WDs that gives us the possibility to study further its properties. In the following subsections, we present the relation between the magnetic field values and other parameters and discuss the consequences of the observations.

6.3.1 Relation between the effective temperature and the magnetic field

WDs have very disperse effective temperature values. The colder WD has an effective temperature close to 3000 K (Kaplan *et al.*, 2014), while one of hottest dwarfs have values up to 250,000 K (Werner; Rauch, 2015). This effective temperature (T_e) is obtained from equation A.24.

Some spectral classifications for WDs and their respective temperature ranges can be seen in Table 6.1.

TABLE 6.1 – Spectral types of WDs and their respective temperatures. Source:Koester (2013).

Name	Spectral types	Temperature (K)
DA	Only Balmer lines; without metals or HeI;	5.000 - >100.000 K
DB	HeI lines; without H or metals;	10.000 - 30.000 K
DC	Continuous spectrum; without lines deeper than 5 %;	<10.000 K
DO	HeII lines; Weak HeI and H lines;	45,000 - >100,000 K
DQ	Carbon lines, molecular or atomic;	10.000 - 24.000 K

According to Valyavin & Fabrika (1999), magnetic WDs tend to be colder (and consequently older), which probably indicates that the magnetic field value is amplified over time. However, Ferrario *et al.* (2015) studied a larger sample of WDs and showed that there is no relation between the magnetic field value and temperature (see Fig 6.3).

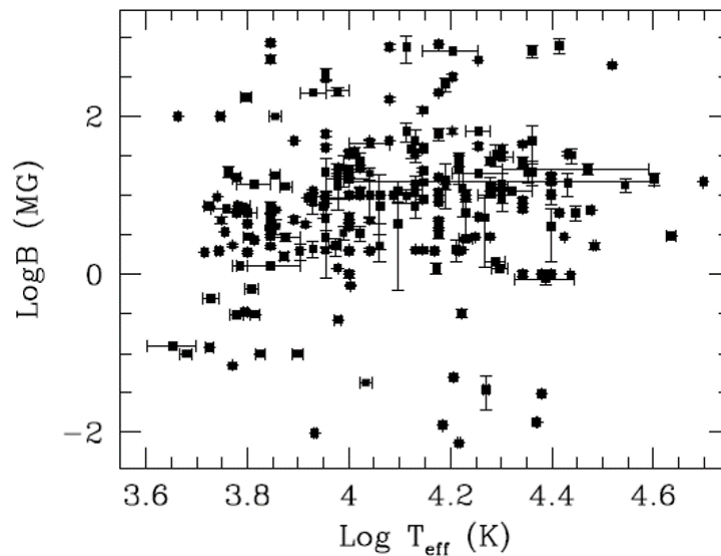


FIGURE 6.3 – Relation between the magnetic field and the effective temperature for isolated WDs. Reference: Ferrario *et al.* (2015).

In addition, the sample of WDs by Wickramasinghe & Ferrario (2000) and Ferrario *et*

al. (2015) is formed by approximately 80% white DA-type dwarfs. According to Koester (2013), DA-type dwarfs are the most common for non-magnetic WDs and have the widest range of temperatures. Hence, it is expected not to see any preferential temperature around magnetic WDs.

In section 5.1, we estimate T_{eff} of 4U 0142+61 as 287,000 K and in section 5.3, we found an magnetic field of $B \sim 3 - 7 \times 10^7$ G. By Figure 6.3, it is not possible correlate any relation between T_{eff} and B. Thus, the estimated values for those two parameters are not excluded.

6.4 Spin period for magnetic isolated WDs

As already discussed in Sec. 6.1, the merger remnant is fast after the coalescence. Thus, it is important to discuss the period onto isolated WDs.

Boshkayev *et al.* (2013) state that the minimum stable period for a rigid-body WDs with 4-He, 12-C, 16-O and 56-Fe nuclei are 0.3 s, 0.5 s, 0.7 s and 2.2 s, respectively. Thus, all SGR/AXPs and new remnants have spins above the bottom theoretical limit.

However, those small spin periods do not agree with observations of isolated magnetic WDs. Excluding RE J0317-853, there is no evidence of fast-rotating isolate magnetic WDs. Even though this lack of fast remnants is still a problem that the merger model faces, there are some possible reasons for that absence.

For instance, García-Berro *et al.* (2012) point out that the spin-down effect is enough to stop the remnant and explain lack of fast spinner in the magnetic isolate WDs classes. In this model, RE J0317-853 is still relatively fast because is the product of a coalescence of two equal mass WDs. This way, the field were less misaligned and the spin-down were smaller, not sufficient to stop the star.

Due to the importance of the period for the SGR/AXPs class, we present and discuss in this section some some observational properties of the period distribution in the isolate magnetic WDs.

6.4.1 Period range for magnetic isolated WDs

Measuring the period value for isolated WDs is a difficult task that can be performed from asteroseismology, polarimetry or spectroscopy. Wickramasinghe & Ferrario (2000) and Brinkworth *et al.* (2013) show that there is a bi-modal period distribution for magnetic WDs, with a group of faster sources, with a period in order of hours, and others quite slowly, with the period of decades or even centuries. Figure 6.4 shows histogram density

of the faster sources.

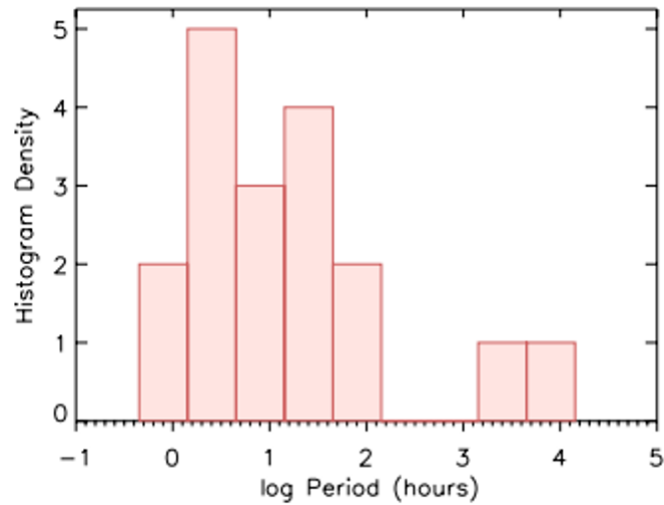


FIGURE 6.4 – Histogram of the period distribution for a sample of 30 magnetic WDs. Reference: Brinkworth *et al.* (2013).

In addition, Figure 6.5 shows a comparative histogram between the period of a sample of magnetic and non-magnetic WDs. Despite the small number of sources present in the samples (17 magnetic and 24 non-magnetic), that prohibit us to state any emphatic conclusion, we can perceive a peak around 1 day in the distribution. Furthermore, sources with shorter periods (order of minutes) tend to be magnetic.

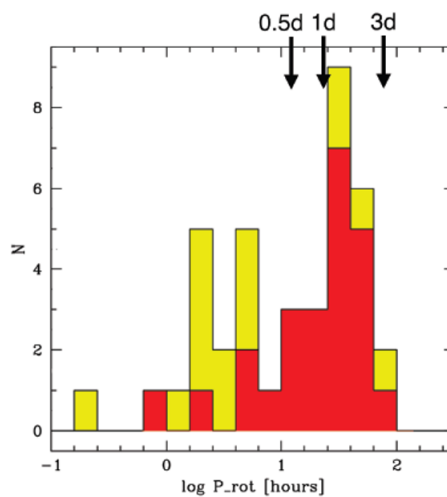


FIGURE 6.5 – Periodic distribution histogram for magnetic WDs (yellow) and non-magnetic WDs (red). Reference: Kawaler (2015).

It is also possible to relate other parameters (magnetic field, mass, age and temperature) with the period. Brinkworth *et al.* (2013) did not find any correlation between the period and other parameters, as can be seen in Figures 6.6, 6.7, 6.8 and 6.9.

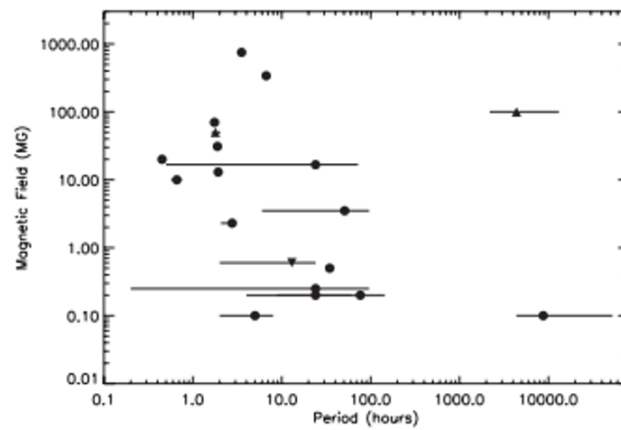


FIGURE 6.6 – Relation between the magnetic field and the period for magnetic WDs. White DA-type dwarfs are circled, DBs are triangles, and fonts that have already been reported as DA or DB are marked as an inverted triangle. Reference: Brinkworth *et al.* (2013).

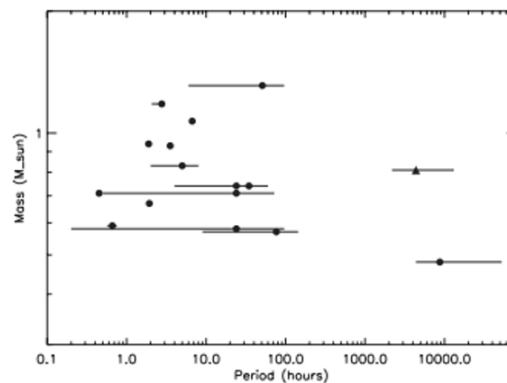


FIGURE 6.7 – Relation between mass and period for magnetic WDs. Reference: Brinkworth *et al.* (2013).

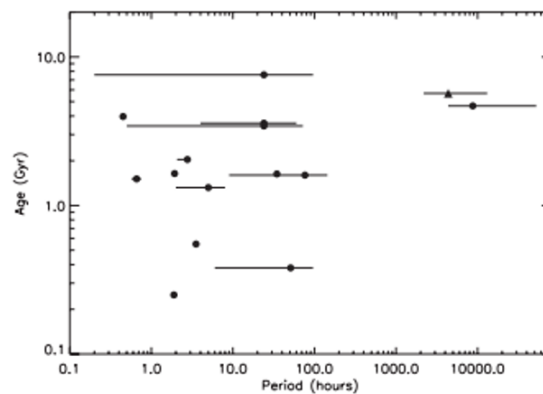


FIGURE 6.8 – Relation between age and period for magnetic WDs. Reference: Brinkworth *et al.* (2013).

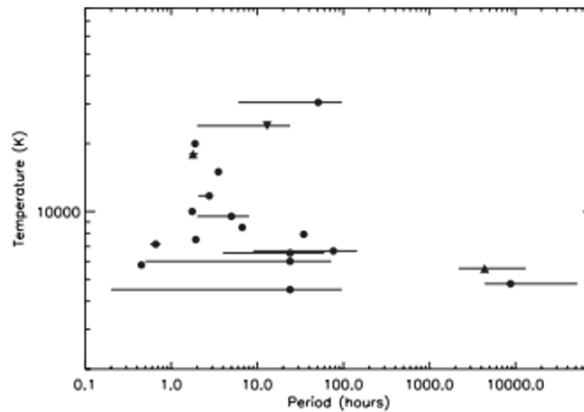


FIGURE 6.9 – Relation between temperature and period for magnetic WDs. Reference: Brinkworth *et al.* (2013).

Unfortunately, the amount of WDs with measured spin period is small, so it is not possible to correlate the period values with other parameters. Also, it is not possible to unambiguously affirm the bi-model behavior of the sample of magnetic WDs. However, if this behavior were true, it would be pointing to two different groups of isolate magnetic WDs.

Those two groups could mean the segregation between the products of merger and those which are formed by other means. It could also point to some differences in the merger process. For instance, the merger of two equal masses WDs tends to generate less misalignment magnetic fields and, consequently, smaller spin-down values. This would lead to a group of faster remnants. Moreover, it is clear that WDs with short period values (of the order of seconds), although uncommon, cannot be discarded.

4U 0142+61 has a period is 8.68 s (Tab. 2.1) and, for the WD accreting model, $B \sim 3 - 7 \times 10^7$ G (see sec. 5.3). That spin period is much smaller than any measured period for isolated magnetic WDs. However, Section 5.2.2 points out to an young object based on T_{eff} . Therefore, the period of 4U 0142+61 is coherent with its short life. For instance, the set of WDs from Tables 6.6 to 6.9 are much older. The youngest WD from Table 6.8 is about 0.1 Gyr old whereas 4U 0142+61 has about 55 kyr. Therefore, it is not possible to compare the spin periods of 4U 0142+61 with the class of magnetic isolated WDs once their ages are not similar.

Considering the spin-down of 2×10^{-12} s.s $^{-1}$, 4U 0142+61 would take 0.05 Gyr to achieve the spin of 1 hour, which is a compatible value for the class of magnetic isolated WDs. Thus, event though its current period is not consistent with other isolated magnetic WDs, it could be after some time.

7 Conclusions and future paths

We show that quiescent emission of the AXP/SGR 4U 0142+61 over all observed spectral range can be explained by a scenario of an accreting white dwarf with a debris disk. The optical/infrared emission of 4U 0142+61 comes from the WD itself and from a debris disk. The hard X-rays is emitted by an accretion column and the soft X-rays by a hot spots in the WD photosphere.

The emission from the hard X-ray bremsstrahlung implies a near-Chandrasekhar WD, with a mass of $1.41 M_{\odot}$ and a radius of 1,021 km. Moreover, from the optical/infrared emission, we obtain an WD effective temperature of 287,000 K. Those radius and temperature point out to an young WD, with an estimate age of 31 kyr. The disk has an inner and outer temperatures of 1937 and 254 K, which leads to a minimum mass of about $10^{-7} M_{\odot}$. From the spin-down, we can estimate a magnetic field of $\sim 10^7$ G, which is consistent with the class of magnetic WDs. Such a WD can be understood as the result of a recent merger of two less massive WDs. In this scenario, 4U 0142+61 is a good candidate to become a SN Ia.

We also performed some estimates of basic properties of other SGR/AXPs in the context of an accreting WD model. For instance, we estimate the magnetic field for the other SGR/AXPs objects. The calculated values are consistent with the observed magnetic fields for both classes of magnetic WDs: isolated and CVs.

We estimated new values of distance for some SGR/AXPs, based on the 3D reddening map of Green *et al.* (2018), including the new estimate of $2.57_{-0.57}^{+0.30}$ kpc for 4U 0142+61 .

There are many perspectives to carry on the study of the accreting WD model for SGR/AXPs. Some are presented below. First, 4U 0142+61 has a period variability in the optical, soft and hard X-rays (see cap. 3) and some outbursts events. Therefore, the WD accreting model must be improved to explain all the observed data of 4U 0142+61 . Thus, it is extremely important to verify whether the periodic emission, as well as the outbursts events of 4U 0142+61 can be explained in this context or not. Also, the model can be tested for other sources of the class, specially those with hard X-rays or optical/infrared emissions. It could be performed more detailed emission of the post-shock region, considering appropriated shock profiles.

Bibliography

Aizu, K. X-Ray Emission Region of a White Dwarf with Accretion. **Progress of Theoretical Physics**, v. 49, p. 1184–1194, abr. 1973.

Alford, J. A. J.; Halpern, J. P. Evolution of the X-Ray Properties of the Transient Magnetar XTE J1810-197. **Astrophysical Journal**, v. 818, p. 122, fev. 2016.

Alpar, M. A. On Young Neutron Stars as Propellers and Accretors with Conventional Magnetic Fields. **Astrophysical Journal**, v. 554, p. 1245–1254, jun. 2001.

Althaus, L. G.; Córscico, A. H.; Isern, J.; García-Berro, E. Evolutionary and pulsational properties of white dwarf stars. **Astronomy & Astrophysics Review**, v. 18, p. 471–566, out. 2010.

An, H.; Kaspi, V. M.; Archibald, R.; Cumming, A. Spectral and Timing Properties of the Magnetar CXOU J164710.2-455216. **Astrophysical Journal**, v. 763, p. 82, fev. 2013.

An, H.; Kaspi, V. M.; Tomsick, J. A.; Cumming, A.; Bodaghee, A.; Gotthelf, E. V.; Rahoui, F. Chandra Observations of SGR 1627-41 near Quiescence. **Astrophysical Journal**, v. 757, p. 68, set. 2012.

Anderson, G. E.; Gaensler, B. M.; Slane, P. O.; Rea, N.; Kaplan, D. L.; Posselt, B.; Levin, L.; Johnston, S.; Murray, S. S.; Brogan, C. L.; Bailes, M.; Bates, S.; Benjamin, R. A.; Bhat, N. D. R.; Burgay, M.; Burke-Spolaor, S.; Chakrabarty, D.; D'Amico, N.; Drake, J. J.; Esposito, P.; Grindlay, J. E.; Hong, J.; Israel, G. L.; Keith, M. J.; Kramer, M.; Lazio, T. J. W.; Lee, J. C.; Mauerhan, J. C.; Milia, S.; Possenti, A.; Stappers, B.; Steeghs, D. T. H. Multi-wavelength Observations of the Radio Magnetar PSR J1622-4950 and Discovery of Its Possibly Associated Supernova Remnant. **Astrophysical Journal**, v. 751, p. 53, maio 2012.

Archibald, R. F.; Kaspi, V. M.; Scholz, P.; Beardmore, A. P.; Gehrels, N.; Kennea, J. A. SWIFT Observations of Two Outbursts from the Magnetar 4U0142+61. **Astrophysical Journal**, v. 834, p. 163, jan. 2017.

Ayasli, S.; Joss, P. C. Thermonuclear processes on accreting neutron stars - A systematic study. **Astrophysical Journal**, v. 256, p. 637–665, maio 1982.

Barstow, M. A.; Jordan, S.; O'Donoghue, D.; Burleigh, M. R.; Napiwotzki, R.; Harrop-Allin, M. K. RE J0317-853: the hottest known highly magnetic DA white dwarf. **MNRAS**, v. 277, p. 971–985, dez. 1995.

- Becerra, L.; Rueda, J. A.; Lorén-Aguilar, P.; García-Berro, E. The Spin Evolution of Fast-rotating, Magnetized Super-Chandrasekhar White Dwarfs in the Aftermath of White Dwarf Mergers. **Astrophysical Journal**, v. 857, p. 134, abr. 2018.
- Belloni, D. Private Comunication. 2018.
- Belloni, D.; Rodrigues, C.; et al. In Preparation. 2019.
- Beloborodov, A. M. On the Mechanism of Hard X-Ray Emission from Magnetars. **Astrophysical Journal**, v. 762, p. 13, jan. 2013.
- Beloborodov, A. M.; Thompson, C. Corona of Magnetars. **Astrophysical Journal**, v. 657, p. 967–993, mar. 2007.
- Bernardini, F.; Israel, G. L.; Stella, L.; Turolla, R.; Esposito, P.; Rea, N.; Zane, S.; Tiengo, A.; Campana, S.; Götz, D.; Mereghetti, S.; Romano, P. Multi-instrument X-ray monitoring of the January 2009 outburst from the recurrent magnetar candidate 1E 1547.0-5408. **Astronomy & Astrophysics**, v. 529, p. A19, maio 2011.
- Beskrovnaya, N. G.; Ikhsanov, N. R. On the origin of the peculiar cataclysmic variable AE Aquarii. **Advances in Space Research**, v. 55, p. 787–790, fev. 2015.
- Bessell, M. S. Standard Photometric Systems. **Annual Review of Astronomy and Astrophysics**, v. 43, p. 293–336, set. 2005.
- Boshkayev, K.; Rueda, J. A.; Ruffini, R.; Siutsou, I. On General Relativistic Uniformly Rotating White Dwarfs. **Astrophysical Journal**, v. 762, p. 117, jan. 2013.
- Bradt, H. V. D.; McClintock, J. E. The optical counterparts of compact galactic X-ray sources. **Annual Review of Astronomy and Astrophysics**, v. 21, p. 13–66, 1983.
- Brinkworth, C. S.; Burleigh, M. R.; Lawrie, K.; Marsh, T. R.; Knigge, C. Measuring the Rotational Periods of Isolated Magnetic White Dwarfs. **Astrophysical Journal**, v. 773, p. 47, ago. 2013.
- Camero, A.; Papitto, A.; Rea, N.; Viganò, D.; Pons, J. A.; Tiengo, A.; Mereghetti, S.; Turolla, R.; Esposito, P.; Zane, S.; Israel, G. L.; Götz, D. Quiescent state and outburst evolution of SGR 0501+4516. **MNRAS**, v. 438, p. 3291–3298, mar. 2014.
- Camilo, F.; Ransom, S. M.; Halpern, J. P.; Reynolds, J. 1E 1547.0-5408: A Radio-emitting Magnetar with a Rotation Period of 2 Seconds. **The Astrophysical Journal, Letters**, v. 666, p. L93–L96, set. 2007.
- CARROLL, B.; OSTLIE, D. **An Introduction to Modern Astrophysics**. Pearson Addison-Wesley, 2007. ISBN 9780805304022. Disponível em: <<http://books.google.com.br/books?id=M8wPAQAAMAAJ>>.
- Carvalho, G. A.; Marinho, R. M.; Malheiro, M. General relativistic effects in the structure of massive white dwarfs. **General Relativity and Gravitation**, v. 50, p. 38, abr. 2018.
- Chiang, E. I.; Goldreich, P. Spectral Energy Distributions of T Tauri Stars with Passive Circumstellar Disks. **Astrophysical Journal**, v. 490, p. 368–376, nov. 1997.

- Chu, Y.-H.; Su, K. Y. L.; Bilikova, J.; Gruendl, R. A.; De Marco, O.; Guerrero, M. A.; Updike, A. C.; Volk, K.; Rauch, T. Spitzer 24 μm Survey for Dust Disks around Hot White Dwarfs. **Astronomical Journal**, v. 142, p. 75, set. 2011.
- Coelho, J. G. Private Comunication. 2017.
- Coelho, J. G.; Malheiro, M. Similarities of SGRs with Low Magnetic Field and White Dwarf Pulsars. **International Journal of Modern Physics Conference Series**, v. 18, p. 96–100, jan. 2012.
- Coelho, J. G.; Malheiro, M. Magnetic dipole moment of soft gamma-ray repeaters and anomalous X-ray pulsars described as massive and magnetic white dwarfs. **Publ. Astron. Soc. Japan**, v. 66, p. 14, fev. 2014.
- Dan, M.; Rosswog, S.; Brüggen, M.; Podsiadlowski, P. The structure and fate of white dwarf merger remnants. **MNRAS**, v. 438, p. 14–34, fev. 2014.
- Danilenko, A. A.; Zyuzin, D. A.; Shibarov, Y. A.; Zharikov, S. V. The Vela and Geminga pulsars in the mid-infrared. **MNRAS**, v. 415, p. 867–880, jul. 2011.
- Davies, B.; Figer, D. F.; Kudritzki, R.-P.; Trombly, C.; Kouveliotou, C.; Wachter, S. The Progenitor Mass of the Magnetar SGR1900+14. **Astrophysical Journal**, v. 707, p. 844–851, dez. 2009.
- Debes, J. H.; Hoard, D. W.; Wachter, S.; Leisawitz, D. T.; Cohen, M. The WIRED Survey. II. Infrared Excesses in the SDSS DR7 White Dwarf Catalog. **Astrophysical Journal Suppl. Ser.**, v. 197, p. 38, dez. 2011.
- den Hartog, P. R.; Kuiper, L.; Hermsen, W.; Kaspi, V. M.; Dib, R.; Knödseder, J.; Gavriil, F. P. Detailed high-energy characteristics of AXP 4U 0142+61. Multi-year observations with INTEGRAL, RXTE, XMM-Newton, and ASCA. **Astronomy & Astrophysics**, v. 489, p. 245–261, out. 2008.
- Dhillon, V. S.; Marsh, T. R.; Hulleman, F.; van Kerkwijk, M. H.; Shearer, A.; Littlefair, S. P.; Gavriil, F. P.; Kaspi, V. M. High-speed, multicolour optical photometry of the anomalous X-ray pulsar 4U 0142+61 with ULTRACAM. **MNRAS**, v. 363, p. 609–614, out. 2005.
- Dhillon, V. S.; Marsh, T. R.; Littlefair, S. P.; Copperwheat, C. M.; Kerry, P.; Dib, R.; Durant, M.; Kaspi, V. M.; Mignani, R. P.; Shearer, A. Optical pulsations from the anomalous X-ray pulsar 1E1048.1-5937. **MNRAS**, v. 394, p. L112–L116, mar. 2009.
- Dhillon, V. S.; Marsh, T. R.; Littlefair, S. P.; Copperwheat, C. M.; Hickman, R. D. G.; Kerry, P.; Levan, A. J.; Rea, N.; Savoury, C. D. J.; Tanvir, N. R.; Turolla, R.; Wiersema, K. The first observation of optical pulsations from a soft gamma repeater: SGR 0501+4516. **MNRAS**, v. 416, p. L16–L20, set. 2011.
- Dib, R.; Kaspi, V. M. 16 yr of RXTE Monitoring of Five Anomalous X-Ray Pulsars. **Astrophysical Journal**, v. 784, p. 37, mar. 2014.
- Duncan, R. C.; Thompson, C. Formation of very strongly magnetized neutron stars - Implications for gamma-ray bursts. **The Astrophysical Journal, Letters**, v. 392, p. L9–L13, jun. 1992.

- Durant, M.; van Kerkwijk, M. H. Distances to Anomalous X-Ray Pulsars Using Red Clump Stars. **Astrophysical Journal**, v. 650, p. 1070–1081, out. 2006.
- Durant, M.; van Kerkwijk, M. H. Extinction Columns and Intrinsic X-Ray Spectra of the Anomalous X-Ray Pulsars. **Astrophysical Journal**, v. 650, p. 1082–1090, out. 2006.
- Durant, M.; van Kerkwijk, M. H. Multiwavelength Variability of the Magnetar 4U 0142+61. **Astrophysical Journal**, v. 652, p. 576–583, nov. 2006.
- Eichler, D.; Gedalin, M.; Lyubarsky, Y. Coherent Emission from Magnetars. **The Astrophysical Journal, Letters**, v. 578, p. L121–L124, out. 2002.
- Ekşi, K. Y.; Hernquist, L.; Narayan, R. Where Are All the Fallback Disks? Constraints on Propeller Systems. **The Astrophysical Journal, Letters**, v. 623, p. L41–L44, abr. 2005.
- Enoto, T.; Makishima, K.; Nakazawa, K.; Kokubun, M.; Kawaharada, M.; Kotoku, J.; Shibasaki, N. Soft and Hard X-Ray Emissions from the Anomalous X-Ray Pulsar 4U 0142+61 Observed with Suzaku. **Publ. Astron. Soc. Japan**, v. 63, p. 387–396, abr. 2011.
- Enoto, T.; Nakazawa, K.; Makishima, K.; Rea, N.; Hurley, K.; Shibata, S. Broadband Study with Suzaku of the Magnetar Class. **The Astrophysical Journal, Letters**, v. 722, p. L162–L167, out. 2010.
- Enoto, T.; Shibata, S.; Kitaguchi, T.; Suwa, Y.; Uchide, T.; Nishioka, H.; Kisaka, S.; Nakano, T.; Murakami, H.; Makishima, K. Magnetar Broadband X-Ray Spectra Correlated with Magnetic Fields: Suzaku Archive of SGRs and AXPs Combined with NuSTAR, Swift, and RXTE. **Astrophysical Journal Suppl. Ser.**, v. 231, p. 8, jul. 2017.
- Ertan, Ü.; Cheng, K. S. On the Infrared, Optical, and High-Energy Emission from the Anomalous X-Ray Pulsar 4U 0142+61. **Astrophysical Journal**, v. 605, p. 840–845, abr. 2004.
- Ertan, Ü.; Erkut, M. H.; Ekşi, K. Y.; Alpar, M. A. The Anomalous X-Ray Pulsar 4U 0142+61: A Neutron Star with a Gaseous Fallback Disk. **Astrophysical Journal**, v. 657, p. 441–447, mar. 2007.
- Esposito, P.; Israel, G. L.; Turolla, R.; Tiengo, A.; Götz, D.; de Luca, A.; Mignani, R. P.; Zane, S.; Rea, N.; Testa, V.; Caraveo, P. A.; Chaty, S.; Mattana, F.; Mereghetti, S.; Pellizzoni, A.; Romano, P. Early X-ray and optical observations of the soft gamma-ray repeater SGR0418+5729. **MNRAS**, v. 405, p. 1787–1795, jul. 2010.
- Esposito, P.; Tiengo, A.; Mereghetti, S.; Israel, G. L.; De Luca, A.; Götz, D.; Rea, N.; Turolla, R.; Zane, S. Xmm-Newton Discovery of 2.6 s Pulsations in the Soft Gamma-Ray Repeater SGR 1627-41. **The Astrophysical Journal, Letters**, v. 690, p. L105–L109, jan. 2009.
- Fahlman, G. G.; Gregory, P. C. An X-ray pulsar in SNR G109.1-1.0. **Nature**, v. 293, p. 202–204, set. 1981.

- Farihi, J.; Jura, M.; Zuckerman, B. Infrared Signatures of Disrupted Minor Planets at White Dwarfs. **Astrophysical Journal**, v. 694, p. 805–819, abr. 2009.
- Ferrario, L.; de Martino, D.; Gänsicke, B. T. Magnetic White Dwarfs. **Space Science Reviews**, v. 191, p. 111–169, out. 2015.
- Ferrario, L.; Vennes, S.; Wickramasinghe, D. T.; Bailey, J. A.; Christian, D. J. EUVE J0317-855 A rapidly rotating, high-field magnetic white dwarf. **MNRAS**, v. 292, p. 205, nov. 1997.
- Ferrario, L.; Wickramasinghe, D. T.; Tuohy, I. R. An emission-line model for AM Herculis systems. **Astrophysical Journal**, v. 341, p. 327–339, jun. 1989.
- Filho, K.; Saraiva, M. **Astronomia e astrofísica**. Ed. Universidade/UFRGS, 2000. ISBN 9788570255396. Disponível em:
<<http://books.google.com.br/books?id=lfVwPwAACAAJ>>.
- Foight, D. R.; Güver, T.; Özel, F.; Slane, P. O. Probing X-Ray Absorption and Optical Extinction in the Interstellar Medium Using Chandra Observations of Supernova Remnants. **Astrophysical Journal**, v. 826, p. 66, jul. 2016.
- Frank, J.; King, A.; Raine, D. J. **Accretion Power in Astrophysics: Third Edition**. [S.l.: s.n.], 2002. 398 p.
- Fukugita, M.; Ichikawa, T.; Gunn, J. E.; Doi, M.; Shimasaku, K.; Schneider, D. P. The Sloan Digital Sky Survey Photometric System. **Astronomical Journal**, v. 111, p. 1748, abr. 1996.
- Gaensler, B. M.; McClure-Griffiths, N. M.; Oey, M. S.; Haverkorn, M.; Dickey, J. M.; Green, A. J. A Stellar Wind Bubble Coincident with the Anomalous X-Ray Pulsar 1E 1048.1-5937: Are Magnetars Formed from Massive Progenitors? **The Astrophysical Journal, Letters**, v. 620, p. L95–L98, fev. 2005.
- García-Berro, E.; Lorén-Aguilar, P.; Aznar-Siguán, G.; Torres, S.; Camacho, J.; Althaus, L. G.; Córscico, A. H.; Külebi, B.; Isern, J. Double Degenerate Mergers as Progenitors of High-field Magnetic White Dwarfs. **Astrophysical Journal**, v. 749, p. 25, abr. 2012.
- Gasques, L. R.; Afanasjev, A. V.; Aguilera, E. F.; Beard, M.; Chamon, L. C.; Ring, P.; Wiescher, M.; Yakovlev, D. G. Nuclear fusion in dense matter: Reaction rate and carbon burning. **Physical Review C**, v. 72, n. 2, p. 025806, ago. 2005.
- Gavriil, F. P.; Dib, R.; Kaspi, V. M. The 2006-2007 Active Phase of Anomalous X-ray Pulsar 4U 0142+61: Radiative and Timing Changes, Bursts, and Burst Spectral Features. **Astrophysical Journal**, v. 736, p. 138, ago. 2011.
- Gelfand, J. D.; Gaensler, B. M. The Compact X-Ray Source 1E 1547.0-5408 and the Radio Shell G327.24-0.13: A New Proposed Association between a Candidate Magnetar and a Candidate Supernova Remnant. **Astrophysical Journal**, v. 667, p. 1111–1118, out. 2007.
- Geng, J.-J.; Zhang, B.; Huang, Y.-F. A Model of White Dwarf Pulsar AR Scorpii. **The Astrophysical Journal, Letters**, v. 831, p. L10, nov. 2016.

- Girven, J.; Brinkworth, C. S.; Farihi, J.; Gänsicke, B. T.; Hoard, D. W.; Marsh, T. R.; Koester, D. Constraints on the Lifetimes of Disks Resulting from Tidally Destroyed Rocky Planetary Bodies. **Astrophysical Journal**, v. 749, p. 154, abr. 2012.
- Göhler, E.; Wilms, J.; Staubert, R. XMM-Newton observation of the anomalous X-ray pulsar 4U 0142+61. **Astronomy & Astrophysics**, v. 433, p. 1079–1083, abr. 2005.
- Goodman, J.; Weare, J. Ensemble samplers with affine invariance. **Communications in Applied Mathematics and Computational Science**, Vol. 5, No. 1, p. 65–80, 2010, v. 5, p. 65–80, 2010.
- Gorenstein, P. Empirical relation between interstellar X-ray absorption and optical extinction. **Astrophysical Journal**, v. 198, p. 95–101, maio 1975.
- Gotthelf, E. V.; Halpern, J. P.; Buxton, M.; Bailyn, C. Imaging X-Ray, Optical, and Infrared Observations of the Transient Anomalous X-Ray Pulsar XTE J1810-197. **Astrophysical Journal**, v. 605, p. 368–377, abr. 2004.
- Green, G. M.; Schlafly, E. F.; Finkbeiner, D.; Rix, H.-W.; Martin, N.; Burgett, W.; Draper, P. W.; Flewelling, H.; Hodapp, K.; Kaiser, N.; Kudritzki, R.-P.; Magnier, E. A.; Metcalfe, N.; Tonry, J. L.; Wainscoat, R.; Waters, C. Galactic reddening in 3D from stellar photometry - an improved map. **MNRAS**, v. 478, p. 651–666, jul. 2018.
- Güver, T.; Özel, F. The relation between optical extinction and hydrogen column density in the Galaxy. **MNRAS**, v. 400, p. 2050–2053, dez. 2009.
- Harding, A. K. The neutron star zoo. **Frontiers of Physics**, v. 8, p. 679–692, dez. 2013.
- Hascoët, R.; Beloborodov, A. M.; den Hartog, P. R. Phase-resolved X-Ray Spectra of Magnetars and the Coronal Outflow Model. **The Astrophysical Journal, Letters**, v. 786, p. L1, maio 2014.
- Henyey, L.; L'Ecuyer, J. Studies in Stellar Evolution. VIII. The Time Scale for the Diffusion of Energy in the Stellar Interior. **Astrophysical Journal**, v. 156, p. 549, maio 1969.
- Hulleman, F.; van Kerkwijk, M. H.; Kulkarni, S. R. An optical counterpart to the anomalous X-ray pulsar 4U0142+61. **Nature**, v. 408, p. 689–692, dez. 2000.
- Hulleman, F.; van Kerkwijk, M. H.; Kulkarni, S. R. The Anomalous X-ray Pulsar 4U 0142+61: Variability in the infrared and a spectral break in the optical. **Astronomy & Astrophysics**, v. 416, p. 1037–1045, mar. 2004.
- Hurley, J. R.; Shara, M. M. White Dwarf Sequences in Dense Star Clusters. **Astrophysical Journal**, v. 589, p. 179–198, maio 2003.
- Hurley, K.; Cline, T.; Mazets, E.; Barthelmy, S.; Butterworth, P.; Marshall, F.; Palmer, D.; Aptekar, R.; Golenetskii, S.; Il'Inskii, V.; Frederiks, D.; McTiernan, J.; Gold, R.; Trombka, J. A giant periodic flare from the soft γ -ray repeater SGR1900+14. **Nature**, v. 397, p. 41–43, jan. 1999.

- Hurley, K.; Li, P.; Kouveliotou, C.; Murakami, T.; Ando, M.; Strohmayer, T.; van Paradijs, J.; Vrba, F.; Luginbuhl, C.; Yoshida, A.; Smith, I. ASCA Discovery of an X-Ray Pulsar in the Error Box of SGR 1900+14. **The Astrophysical Journal, Letters** , v. 510, p. L111–L114, jan. 1999.
- Israel, G.; Oosterbroek, T.; Stella, L.; Campana, S.; Mereghetti, S.; Parmar, A. N. The Pulse-Phase-dependent Spectrum of the Anomalous X-Ray Pulsar 1RXS J170849-400910. **The Astrophysical Journal, Letters** , v. 560, p. L65–L69, out. 2001.
- Israel, G. L.; Esposito, P.; Rea, N.; Coti Zelati, F.; Tiengo, A.; Campana, S.; Mereghetti, S.; Rodriguez Castillo, G. A.; Götz, D.; Burgay, M.; Possenti, A.; Zane, S.; Turolla, R.; Perna, R.; Cannizzaro, G.; Pons, J. The discovery, monitoring and environment of SGR J1935+2154. **MNRAS**, v. 457, p. 3448–3456, abr. 2016.
- Itoh, N.; Sakamoto, T.; Kusano, S.; Nozawa, S.; Kohyama, Y. Relativistic Thermal Bremsstrahlung Gaunt Factor for the Intracluster Plasma. II. Analytic Fitting Formulae. **Astrophysical Journal Suppl. Ser.**, v. 128, p. 125–138, maio 2000.
- Ji, S.; Fisher, R. T.; García-Berro, E.; Tzeferacos, P.; Jordan, G.; Lee, D.; Lorén-Aguilar, P.; Cremer, P.; Behrends, J. The Post-merger Magnetized Evolution of White Dwarf Binaries: The Double-degenerate Channel of Sub-Chandrasekhar Type Ia Supernovae and the Formation of Magnetized White Dwarfs. **Astrophysical Journal**, v. 773, p. 136, ago. 2013.
- Juett, A. M.; Marshall, H. L.; Chakrabarty, D.; Schulz, N. S. Chandra High-Resolution Spectrum of the Anomalous X-Ray Pulsar 4U 0142+61. **The Astrophysical Journal, Letters** , v. 568, p. L31–L34, mar. 2002.
- Jura, M. A Tidally Disrupted Asteroid around the White Dwarf G29-38. **The Astrophysical Journal, Letters** , v. 584, p. L91–L94, fev. 2003.
- Kaplan, D. L.; Boyles, J.; Dunlap, B. H.; Tendulkar, S. P.; Deller, A. T.; Ransom, S. M.; McLaughlin, M. A.; Lorimer, D. R.; Stairs, I. H. A 1.05 M_{\odot} Companion to PSR J2222-0137: The Coolest Known White Dwarf? **Astrophysical Journal**, v. 789, p. 119, jul. 2014.
- Kaplan, D. L.; Chakrabarty, D.; Wang, Z.; Wachter, S. A Mid-Infrared Counterpart to the Magnetar 1E 2259+586. **Astrophysical Journal**, v. 700, p. 149–154, jul. 2009.
- Karzas, W. J.; Latter, R. Electron Radiative Transitions in a Coulomb Field. **Astrophysical Journal Suppl. Ser.**, v. 6, p. 167, maio 1961.
- Kaspi, V. M.; Beloborodov, A. M. Magnetars. **Annual Review of Astronomy and Astrophysics**, v. 55, p. 261–301, ago. 2017.
- Kawaler, S. D. Rotation of White Dwarf Stars. In: Dufour, P.; Bergeron, P.; Fontaine, G. (Ed.). **19th European Workshop on White Dwarfs**. [S.l.: s.n.], 2015. (Astronomical Society of the Pacific Conference Series, v. 493), p. 65.
- Kellogg, E.; Baldwin, J. R.; Koch, D. Studies of cluster X-ray sources, energy spectra for the Perseus, Virgo, and Coma clusters. **Astrophysical Journal**, v. 199, p. 299–306, jul. 1975.

- Kepler, S. O.; Pelisoli, I.; Jordan, S.; Kleinman, S. J.; Koester, D.; Külebi, B.; Peçanha, V.; Castanheira, B. G.; Nitta, A.; Costa, J. E. S.; Winget, D. E.; Kanaan, A.; Fraga, L. Magnetic white dwarf stars in the Sloan Digital Sky Survey. **MNRAS**, v. 429, p. 2934–2944, mar. 2013.
- Kern, B.; Martin, C. Optical pulsations from the anomalous X-ray pulsar 4U0142+61. **Nature**, v. 417, p. 527–529, maio 2002.
- Kilic, M.; Hambly, N. C.; Bergeron, P.; Genest-Beaulieu, C.; Rowell, N. Gaia reveals evidence for merged white dwarfs. **MNRAS**, v. 479, p. L113–L117, set. 2018.
- Kitaguchi, T.; An, H.; Beloborodov, A. M.; Gotthelf, E. V.; Hayashi, T.; Kaspi, V. M.; Rana, V. R.; Boggs, S. E.; Christensen, F. E.; Craig, W. W.; Hailey, C. J.; Harrison, F. A.; Stern, D.; Zhang, W. W. NuSTAR and Swift Observations of the Fast Rotating Magnetized White Dwarf AE Aquarii. **Astrophysical Journal**, v. 782, p. 3, fev. 2014.
- Koester, D. White Dwarf Stars. In: _____. **Planets, Stars and Stellar Systems. Volume 4: Stellar Structure and Evolution**. [S.l.: s.n.], 2013. p. 559.
- Koester, D.; Gänsicke, B. T.; Farihi, J. The frequency of planetary debris around young white dwarfs. **Astronomy & Astrophysics**, v. 566, p. A34, jun. 2014.
- Kothes, R.; Foster, T. A Thorough Investigation of the Distance to the Supernova Remnant CTB109 and Its Pulsar AXP J2301+5852. **The Astrophysical Journal, Letters** , v. 746, p. L4, fev. 2012.
- Koyama, K.; Hoshi, R.; Nagase, F. X-ray observations of the extraordinary pulsar 1E 2259 + 586. **Publ. Astron. Soc. Japan**, v. 39, p. 801–807, 1987.
- Kuiper, L.; Hermsen, W.; den Hartog, P. R.; Collmar, W. Discovery of Luminous Pulsed Hard X-Ray Emission from Anomalous X-Ray Pulsars 1RXS J1708-4009, 4U 0142+61, and 1E 2259+586 by INTEGRAL and RXTE. **Astrophysical Journal**, v. 645, p. 556–575, jul. 2006.
- Külebi, B.; Ekşi, K. Y.; Lorén-Aguilar, P.; Isern, J.; García-Berro, E. Magnetic white dwarfs with debris discs. **MNRAS**, v. 431, p. 2778–2788, maio 2013.
- Lamb, D. Q.; Masters, A. R. X and UV radiation from accreting magnetic degenerate dwarfs. **The Astrophysical Journal, Letters** , v. 234, p. L117–L122, dez. 1979.
- Laros, J. G.; Fenimore, E. E.; Klebesadel, R. W.; Atteia, J.-L.; Boer, M.; Hurley, K.; Niel, M.; Vedrenne, G.; Kane, S. R.; Kouveliotou, C.; Cline, T. L.; Dennis, B. R.; Desai, U. D.; Orwig, L. E.; Kuznetsov, A. V.; Sunyaev, R. A.; Terekhov, O. V. A new type of repetitive behavior in a high-energy transient. **The Astrophysical Journal, Letters** , v. 320, p. L111–L115, set. 1987.
- LÉNA, P.; LEBRUN, F.; MIGNARD, F. **Observational Astrophysics**. Springer, 1998. (Astronomy and astrophysics library). ISBN 9783540634829. Disponível em: <<http://books.google.com.br/books?id=wXCMYy0yF5cC>>.
- Lewin, W. H. G.; van Paradijs, J.; Taam, R. E. X-Ray Bursts. **Space Science Reviews**, v. 62, p. 223–389, set. 1993.

- Lin, L.; Kouveliotou, C.; Baring, M. G.; van der Horst, A. J.; Guiriec, S.; Woods, P. M.; Göğüş, E.; Kaneko, Y.; Scargle, J.; Granot, J.; Preece, R.; von Kienlin, A.; Chaplin, V.; Watts, A. L.; Wijers, R. A. M. J.; Zhang, S. N.; Bhat, N.; Finger, M. H.; Gehrels, N.; Harding, A.; Kaper, L.; Kaspi, V.; Mcenery, J.; Meegan, C. A.; Paciesas, W. S.; Pe'er, A.; Ramirez-Ruiz, E.; van der Klis, M.; Wachter, S.; Wilson-Hodge, C. Fermi/Gamma-Ray Burst Monitor Observations of SGR J0501+4516 Bursts. **Astrophysical Journal**, v. 739, p. 87, out. 2011.
- Lodders, K. Solar System Abundances and Condensation Temperatures of the Elements. **Astrophysical Journal**, v. 591, p. 1220–1247, jul. 2003.
- López-Corredoira, M.; Cabrera-Lavers, A.; Garzón, F.; Hammersley, P. L. Old stellar Galactic disc in near-plane regions according to 2MASS: Scales, cut-off, flare and warp. **Astronomy & Astrophysics**, v. 394, p. 883–899, nov. 2002.
- Lorén-Aguilar, P.; Isern, J.; García-Berro, E. High-resolution smoothed particle hydrodynamics simulations of the merger of binary white dwarfs. **Astronomy & Astrophysics**, v. 500, p. 1193–1205, jun. 2009.
- Madej, J.; Należyty, M.; Althaus, L. G. Mass distribution of DA white dwarfs in the First Data Release of the Sloan Digital Sky Survey. **Astronomy & Astrophysics**, v. 419, p. L5–L8, maio 2004.
- Malheiro, M.; Coelho, J. G. Describing SGRs/AXPs as fast and magnetized white dwarfs. **ArXiv e-prints**, jul. 2013.
- Malheiro, M.; Rueda, J. A.; Ruffini, R. SGRs and AXPs as Rotation-Powered Massive White Dwarfs. **Publ. Astron. Soc. Japan**, v. 64, p. 56, jun. 2012.
- Malheiro, M.; Rueda, J. A.; Ruffini, R. SGRs and AXPs as Rotation-Powered Massive White Dwarfs. **Publ. Astron. Soc. Japan**, v. 64, p. 56, jun. 2012.
- Maoz, D.; Mannucci, F.; Nelemans, G. Observational Clues to the Progenitors of Type Ia Supernovae. **Annual Review of Astronomy and Astrophysics**, v. 52, p. 107–170, ago. 2014.
- Mazets, E. P.; Golenetskii, S. V.; Ilinskii, V. N.; Panov, V. N.; Aptekar, R. L.; Gurian, I. A.; Proskura, M. P.; Sokolov, I. A.; Sokolova, Z. I.; Kharitonova, T. V. Catalog of cosmic gamma-ray bursts from the KONUS experiment data. I. **Astrophysics and Space Science**, v. 80, p. 3–83, nov. 1981.
- Mazets, E. P.; Golentskii, S. V.; Ilinskii, V. N.; Aptekar, R. L.; Guryan, I. A. Observations of a flaring X-ray pulsar in Dorado. **Nature**, v. 282, p. 587–589, dez. 1979.
- Melis, C.; Dufour, P.; Farihi, J.; Bochanski, J.; Burgasser, A. J.; Parsons, S. G.; Gänsicke, B. T.; Koester, D.; Swift, B. J. Gaseous Material Orbiting the Polluted, Dusty White Dwarf HE 1349-2305. **The Astrophysical Journal, Letters**, v. 751, p. L4, maio 2012.
- Menou, K.; Perna, R.; Hernquist, L. Stability and Evolution of Supernova Fallback Disks. **Astrophysical Journal**, v. 559, p. 1032–1046, out. 2001.

- Mereghetti, S. The strongest cosmic magnets: soft gamma-ray repeaters and anomalous X-ray pulsars. **Astronomy & Astrophysics Review**, v. 15, p. 225–287, jul. 2008.
- Mereghetti, S.; Esposito, P.; Tiengo, A.; Zane, S.; Turolla, R.; Stella, L.; Israel, G. L.; Götz, D.; Feroci, M. The First XMM-Newton Observations of the Soft Gamma-Ray Repeater SGR 1900+14. **Astrophysical Journal**, v. 653, p. 1423–1428, dez. 2006.
- Mereghetti, S.; La Palombara, N.; Tiengo, A.; Pizzolato, F.; Esposito, P.; Woudt, P. A.; Israel, G. L.; Stella, L. X-Ray and Optical Observations of the Unique Binary System HD 49798/RX J0648.0-4418. **Astrophysical Journal**, v. 737, p. 51, ago. 2011.
- Mestel, L. On the theory of white dwarf stars. I. The energy sources of white dwarfs. **MNRAS**, v. 112, p. 583, 1952.
- Metzger, B. D.; Rafikov, R. R.; Bochkarev, K. V. Global models of runaway accretion in white dwarf debris discs. **MNRAS**, v. 423, p. 505–528, jun. 2012.
- Mewe, R.; Lemen, J. R.; van den Oord, G. H. J. Calculated X-radiation from optically thin plasmas. VI - Improved calculations for continuum emission and approximation formulae for nonrelativistic average Gaunt factors. **Astronomy & Astrophysics, Supplement**, v. 65, p. 511–536, set. 1986.
- Miller, M. C.; Hamilton, D. P. Implications of the PSR 1257+12 Planetary System for Isolated Millisecond Pulsars. **Astrophysical Journal**, v. 550, p. 863–870, abr. 2001.
- Morii, M.; Kawai, N.; Kataoka, J.; Yatsu, Y.; Kobayashi, N.; Terada, H. Near-infrared, optical, and X-ray observations of the anomalous X-ray pulsar 4U 0142 + 61. **Advances in Space Research**, v. 35, p. 1177–1180, 2005.
- Morii, M.; Kobayashi, N.; Kawai, N.; Terada, H.; Tanaka, Y. T.; Kitamoto, S.; Shibasaki, N. Search for Near-Infrared Pulsation of the Anomalous X-Ray Pulsar 4U 0142+61. **Publ. Astron. Soc. Japan**, v. 61, p. 51–56, fev. 2009.
- Morii, M.; Sato, R.; Kataoka, J.; Kawai, N. Chandra Observation of the Anomalous X-Ray Pulsar 1E 1841-045. **Publ. Astron. Soc. Japan**, v. 55, p. L45–L48, jun. 2003.
- Morrison, R.; McCammon, D. Interstellar photoelectric absorption cross sections, 0.03-10 keV. **Astrophysical Journal**, v. 270, p. 119–122, jul. 1983.
- Muñoz-Darias, T.; de Ugarte Postigo, A.; Casares, J. The featureless and non-variable optical spectral energy distribution of AXP 4U 0142+61. **MNRAS**, v. 458, p. L114–L117, maio 2016.
- Nakagawa, Y. E.; Mihara, T.; Yoshida, A.; Yamaoka, K.; Sugita, S.; Murakami, T.; Yonetoku, D.; Suzuki, M.; Nakajima, M.; Tashiro, M. S.; Nakazawa, K. Suzaku Observations of SGR1900+14 and SGR1806-20. **Publ. Astron. Soc. Japan**, v. 61, p. S387–S393, jan. 2009.
- NASA/IPAC. **EXTRAGALACTIC DATABASE - Coordinate Transformation & Galactic Extinction Calculator**. 2018. Disponível em: <<https://ned.ipac.caltech.edu/forms/calculator.html>>.

- Nauenberg, M. Analytic Approximations to the Mass-Radius Relation and Energy of Zero-Temperature Stars. **Astrophysical Journal**, v. 175, p. 417, jul. 1972.
- Nomoto, K.; Kondo, Y. Conditions for accretion-induced collapse of white dwarfs. **The Astrophysical Journal, Letters**, v. 367, p. L19–L22, jan. 1991.
- Nozawa, S.; Itoh, N.; Kohyama, Y. Relativistic Thermal Bremsstrahlung Gaunt Factor for the Intracluster Plasma. **Astrophysical Journal**, v. 507, p. 530–557, nov. 1998.
- Olausen, S. A.; Kaspi, V. M. The McGill Magnetar Catalog. **Astrophysical Journal Suppl. Ser.**, v. 212, p. 6, maio 2014.
- Oosterbroek, T.; Parmar, A. N.; Mereghetti, S.; Israel, G. L. The two-component X-ray spectrum of the 6.4 S pulsar 1E 1048.1-5937. **Astronomy & Astrophysics**, v. 334, p. 925–930, jun. 1998.
- Ossenkopf, V.; Henning, T.; Mathis, J. S. Constraints on cosmic silicates. **Astronomy & Astrophysics**, v. 261, p. 567–578, ago. 1992.
- Ouyed, R.; Leahy, D.; Niebergal, B. SGR 0418+5729 as an evolved Quark-Nova compact remnant. **MNRAS**, v. 415, p. 1590–1596, ago. 2011.
- Park, S.; Hughes, J. P.; Slane, P. O.; Burrows, D. N.; Lee, J.-J.; Mori, K. An X-Ray Study of Supernova Remnant N49 and Soft Gamma-Ray Repeater 0526-66 in the Large Magellanic Cloud. **Astrophysical Journal**, v. 748, p. 117, abr. 2012.
- Patterson, J.; Raymond, J. C. X-ray emission from cataclysmic variables with accretion disks. I - Hard X-rays. II - EUV/soft X-ray radiation. **Astrophysical Journal**, v. 292, p. 535–558, maio 1985.
- Pavlović, M. Z.; Urošević, D.; Vukotić, B.; Arbutina, B.; Göker, Ü. D. The Radio Surface-brightness-to-Diameter Relation for Galactic Supernova Remnants: Sample Selection and Robust Analysis with Various Fitting Offsets. **Astrophysical Journal Suppl. Ser.**, v. 204, p. 4, jan. 2013.
- Perna, R.; Hernquist, L.; Narayan, R. Emission Spectra of Fallback Disks around Young Neutron Stars. **Astrophysical Journal**, v. 541, p. 344–350, set. 2000.
- Predehl, P.; Schmitt, J. H. M. M. X-raying the interstellar medium: ROSAT observations of dust scattering halos. **Astronomy & Astrophysics**, v. 293, p. 889–905, jan. 1995.
- Rafikov, R. R.; Garmilla, J. A. Inner Edges of Compact Debris Disks around Metal-rich White Dwarfs. **Astrophysical Journal**, v. 760, p. 123, dez. 2012.
- Ramsay, G.; Cropper, M. The energy balance of polars revisited. **MNRAS**, v. 347, p. 497–507, jan. 2004.
- Raskin, C.; Scannapieco, E.; Fryer, C.; Rockefeller, G.; Timmes, F. X. Remnants of Binary White Dwarf Mergers. **Astrophysical Journal**, v. 746, p. 62, fev. 2012.

- Rea, N.; Israel, G. L.; Pons, J. A.; Turolla, R.; Viganò, D.; Zane, S.; Esposito, P.; Perna, R.; Papitto, A.; Terreran, G.; Tiengo, A.; Salvetti, D.; Girart, J. M.; Palau, A.; Possenti, A.; Burgay, M.; Göğüş, E.; Caliendo, G. A.; Kouveliotou, C.; Götz, D.; Mignani, R. P.; Ratti, E.; Stella, L. The Outburst Decay of the Low Magnetic Field Magnetar SGR 0418+5729. **Astrophysical Journal**, v. 770, p. 65, jun. 2013.
- Rea, N.; Nichelli, E.; Israel, G. L.; Perna, R.; Oosterbroek, T.; Parmar, A. N.; Turolla, R.; Campana, S.; Stella, L.; Zane, S.; Angelini, L. Very deep X-ray observations of the anomalous X-ray pulsar 4U0142+614. **MNRAS**, v. 381, p. 293–300, out. 2007.
- Rea, N.; Pons, J. A.; Torres, D. F.; Turolla, R. The Fundamental Plane for Radio Magnetars. **The Astrophysical Journal, Letters**, v. 748, p. L12, mar. 2012.
- Reina, C.; Tarengi, M. X-ray Absorption and Optical Extinction in Interstellar Space. **Astronomy & Astrophysics**, v. 26, p. 257, jul. 1973.
- Rodríguez Castillo, G. A.; Israel, G. L.; Esposito, P.; Pons, J. A.; Rea, N.; Turolla, R.; Viganò, D.; Zane, S. Pulse phase-coherent timing and spectroscopy of CXOU J164710.2-45521 outbursts. **MNRAS**, v. 441, p. 1305–1316, jun. 2014.
- Rueda, J. A.; Boshkayev, K.; Izzo, L.; Ruffini, R.; Lorén-Aguilar, P.; Külebi, B.; Aznar-Siguán, G.; García-Berro, E. A White Dwarf Merger as Progenitor of the Anomalous X-Ray Pulsar 4U 0142+61? **The Astrophysical Journal, Letters**, v. 772, p. L24, ago. 2013.
- RYBICKI, G.; LIGHTMAN, A. **Radiative Processes in Astrophysics**. Wiley, 1979. (A Wiley-Interscience publication). ISBN 9780471827597. Disponível em: <<https://books.google.com.br/books?id=LtdEjNABMlsc>>.
- Rybicki, G. B.; Lightman, A. P. **Radiative processes in astrophysics**. [S.l.: s.n.], 1979.
- Ryter, C.; Cesarsky, C. J.; Audouze, J. X-ray absorption, interstellar reddening, and elemental abundances in the interstellar medium. **Astrophysical Journal**, v. 198, p. 103–109, maio 1975.
- Saio, H.; Nomoto, K. Off-Center Carbon Ignition in Rapidly Rotating, Accreting Carbon-Oxygen White Dwarfs. **Astrophysical Journal**, v. 615, p. 444–449, nov. 2004.
- Sandberg, A.; Sollerman, J. Optical and infrared observations of the Crab Pulsar and its nearby knot. **Astronomy & Astrophysics**, v. 504, p. 525–530, set. 2009.
- Sato, T.; Bamba, A.; Nakamura, R.; Ishida, M. Identification of CXOU J171405.7-381031 as a New Magnetar with XMM-Newton. **Publ. Astron. Soc. Japan**, v. 62, p. L33–L36, out. 2010.
- Schlafly, E. F.; Finkbeiner, D. P. Measuring Reddening with Sloan Digital Sky Survey Stellar Spectra and Recalibrating SFD. **Astrophysical Journal**, v. 737, p. 103, ago. 2011.
- Schlegel, D. J.; Finkbeiner, D. P.; Davis, M. Maps of Dust Infrared Emission for Use in Estimation of Reddening and Cosmic Microwave Background Radiation Foregrounds. **Astrophysical Journal**, v. 500, p. 525–553, jun. 1998.

- Scholz, P.; Ng, C.-Y.; Livingstone, M. A.; Kaspi, V. M.; Cumming, A.; Archibald, R. F. Post-outburst X-Ray Flux and Timing Evolution of Swift J1822.3-1606. **Astrophysical Journal**, v. 761, p. 66, dez. 2012.
- Shakura, N. I.; Sunyaev, R. A. Black holes in binary systems. Observational appearance. **Astronomy & Astrophysics**, v. 24, p. 337–355, 1973.
- Suleimanov, V.; Doroshenko, V.; Ducci, L.; Zhukov, G. V.; Werner, K. GK Per and EX Hya: Intermediate polars with small magnetospheres. **ArXiv e-prints**, abr. 2016.
- Surnis, M. P.; Joshi, B. C.; Maan, Y.; Krishnakumar, M. A.; Manoharan, P. K.; Naidu, A. Radio Pulsation Search and Imaging Study of SGR J1935+2154. **Astrophysical Journal**, v. 826, p. 184, ago. 2016.
- Sutherland, R. S. Accurate free-free Gaunt factors for astrophysical plasmas. **MNRAS**, v. 300, p. 321–330, out. 1998.
- Tam, C. R.; Gavriil, F. P.; Dib, R.; Kaspi, V. M.; Woods, P. M.; Bassa, C. X-Ray and Near-IR Variability of the Anomalous X-Ray Pulsar 1E 1048.1-5937: From Quiescence Back to Activity. **Astrophysical Journal**, v. 677, p. 503–514, abr. 2008.
- Tendulkar, S. P.; Hascöet, R.; Yang, C.; Kaspi, V. M.; Beloborodov, A. M.; An, H.; Bachetti, M.; Boggs, S. E.; Christensen, F. E.; Craig, W. W.; Guillot, S.; Hailey, C. A.; Harrison, F. A.; Stern, D.; Zhang, W. Phase-resolved NuSTAR and Swift-XRT Observations of Magnetar 4U 0142+61. **Astrophysical Journal**, v. 808, p. 32, jul. 2015.
- Thompson, C.; Duncan, R. C. The soft gamma repeaters as very strongly magnetized neutron stars - I. Radiative mechanism for outbursts. **MNRAS**, v. 275, p. 255–300, jul. 1995.
- Tiengo, A.; Esposito, P.; Mereghetti, S. XMM-Newton Observations of CXOU J010043.1-721134: The First Deep Look at the Soft X-Ray Emission of a Magnetar. **The Astrophysical Journal, Letters**, v. 680, p. L133, jun. 2008.
- Tiengo, A.; Esposito, P.; Mereghetti, S.; Israel, G. L.; Stella, L.; Turolla, R.; Zane, S.; Rea, N.; Götz, D.; Feroci, M. Quiet but still bright: XMM-Newton observations of the soft gamma-ray repeater SGR0526-66. **MNRAS**, v. 399, p. L74–L78, out. 2009.
- Toonen, S.; Hollands, M.; Gänsicke, B. T.; Boekholt, T. The binarity of the local white dwarf population. **Astronomy & Astrophysics**, v. 602, p. A16, jun. 2017.
- Trümper, J. E.; Dennerl, K.; Kylafis, N. D.; Ertan, Ü.; Zezas, A. An Accretion Model for the Anomalous X-Ray Pulsar 4U 0142+61. **Astrophysical Journal**, v. 764, p. 49, fev. 2013.
- Turolla, R.; Zane, S.; Watts, A. L. Magnetars: the physics behind observations. A review. **Reports on Progress in Physics**, v. 78, n. 11, p. 116901, nov. 2015.
- Usov, V. V. Glitches in the X-ray pulsar 1E 2259+586. **Astrophysical Journal**, v. 427, p. 984–986, jun. 1994.

Valencic, L. A.; Smith, R. K. Interstellar Dust Properties from a Survey of X-Ray Halos. **Astrophysical Journal**, v. 809, p. 66, ago. 2015.

Valyavin, G.; Fabrika, S. White dwarfs magnetic fields evolution. In: Solheim, S.-E.; Meistas, E. G. (Ed.). **11th European Workshop on White Dwarfs**. [S.l.: s.n.], 1999. (Astronomical Society of the Pacific Conference Series, v. 169), p. 206.

van der Horst, A. J.; Connaughton, V.; Kouveliotou, C.; Göğüş, E.; Kaneko, Y.; Wachter, S.; Briggs, M. S.; Granot, J.; Ramirez-Ruiz, E.; Woods, P. M.; Aptekar, R. L.; Barthelmy, S. D.; Cummings, J. R.; Finger, M. H.; Frederiks, D. D.; Gehrels, N.; Gelino, C. R.; Gelino, D. M.; Golenetskii, S.; Hurley, K.; Krimm, H. A.; Mazets, E. P.; McEnery, J. E.; Meegan, C. A.; Oleynik, P. P.; Palmer, D. M.; Pal'shin, V. D.; Pe'er, A.; Svinkin, D.; Ulanov, M. V.; van der Klis, M.; von Kienlin, A.; Watts, A. L.; Wilson-Hodge, C. A. Discovery of a New Soft Gamma Repeater: SGR J0418 + 5729. **The Astrophysical Journal, Letters**, v. 711, p. L1–L6, mar. 2010.

van Hoof, P. A. M.; Ferland, G. J.; Williams, R. J. R.; Volk, K.; Chatzikos, M.; Lykins, M.; Porter, R. L. Accurate determination of the free-free Gaunt factor - II. Relativistic Gaunt factors. **MNRAS**, v. 449, p. 2112–2118, maio 2015.

van Kerkwijk, M. H.; Chang, P.; Justham, S. Sub-Chandrasekhar White Dwarf Mergers as the Progenitors of Type Ia Supernovae. **The Astrophysical Journal, Letters**, v. 722, p. L157–L161, out. 2010.

van Paradijs, J.; Taam, R. E.; van den Heuvel, E. P. J. On the nature of the 'anomalous' 6-s X-ray pulsars. **Astronomy & Astrophysics**, v. 299, p. L41, jul. 1995.

Vennes, S.; Schmidt, G. D.; Ferrario, L.; Christian, D. J.; Wickramasinghe, D. T.; Kawka, A. A Multiwavelength Study of the High-Field Magnetic White Dwarf EUVE J0317-85.5 (=RE J0317-853). **Astrophysical Journal**, v. 593, p. 1040–1048, ago. 2003.

Vennes, S.; Thejll, P. A.; Génova Galvan, R.; Dupuis, J. Hot White Dwarfs in the Extreme Ultraviolet Explorer Survey. II. Mass Distribution, Space Density, and Population Age. **Astrophysical Journal**, v. 480, p. 714–734, maio 1997.

Wang, W.; Tong, H.; Guo, Y.-J. Hard X-ray emission cutoff in the anomalous X-ray pulsar 4U 0142+61 detected by INTEGRAL. **Research in Astronomy and Astrophysics**, v. 14, p. 673–682, jun. 2014.

Wang, Y.-M. Disc accretion by magnetized neutron stars - A reassessment of the torque. **Astronomy & Astrophysics**, v. 183, p. 257–264, set. 1987.

Wang, Z.; Chakrabarty, D.; Kaplan, D. L. A debris disk around an isolated young neutron star. **Nature**, v. 440, p. 772–775, abr. 2006.

Wang, Z.; Chakrabarty, D.; Kaplan, D. L. Spitzer IRS Spectroscopy and MIPS Imaging of the Anomalous X-ray Pulsar 4U 0142+61. In: Bassa, C.; Wang, Z.; Cumming, A.; Kaspi, V. M. (Ed.). **40 Years of Pulsars: Millisecond Pulsars, Magnetars and More**. [S.l.: s.n.], 2008. (American Institute of Physics Conference Series, v. 983), p. 274–276.

- Wang, Z.; Tanaka, Y. T.; Wang, C.; Kawabata, K. S.; Fukazawa, Y.; Itoh, R.; Tziamtzis, A. Optical I-band Linear Polarimetry of the Magnetar 4U 0142+61 with Subaru. **Astrophysical Journal**, v. 814, p. 89, dez. 2015.
- Wang, Z.; Tanaka, Y. T.; Zhong, J. Subaru Constraint on Circular Polarization in I-Band Emission from the Magnetar 4U 0142+61. **Publ. Astron. Soc. Japan**, v. 64, abr. 2012.
- Warner, B. **Cataclysmic Variable Stars**. [S.l.: s.n.], 2003. 592 p.
- Watson, D. The Galactic dust-to-metals ratio and metallicity using gamma-ray bursts. **Astronomy & Astrophysics**, v. 533, p. A16, set. 2011.
- Webbink, R. F.; Livio, M.; Truran, J. W.; Orio, M. The nature of the recurrent novae. **Astrophysical Journal**, v. 314, p. 653–672, mar. 1987.
- Werner, K.; Rauch, T. Analysis of HST/COS spectra of the bare C-O stellar core <ASTROBJ>H1504+65</ASTROBJ> and a high-velocity twin in the Galactic halo. **Astronomy & Astrophysics**, v. 584, p. A19, dez. 2015.
- White, N. E.; Angelini, L.; Ebisawa, K.; Tanaka, Y.; Ghosh, P. The Spectrum of the 8.7s X-Ray Pulsar 4U0142+61. **The Astrophysical Journal, Letters**, v. 463, p. L83, jun. 1996.
- Wickramasinghe, D. T.; Farihi, J.; Tout, C. A.; Ferrario, L.; Stancliffe, R. J. Does GD356 have a terrestrial planetary companion? **MNRAS**, v. 404, p. 1984–1991, jun. 2010.
- Wickramasinghe, D. T.; Ferrario, L. Magnetism in Isolated and Binary White Dwarfs. **Publications of the ASP**, v. 112, p. 873–924, jul. 2000.
- Wilms, J.; Allen, A.; McCray, R. On the Absorption of X-Rays in the Interstellar Medium. **Astrophysical Journal**, v. 542, p. 914–924, out. 2000.
- Wolszczan, A.; Frail, D. A. A planetary system around the millisecond pulsar PSR1257 + 12. **Nature**, v. 355, p. 145–147, jan. 1992.
- Wynn, G. A.; King, A. R.; Horne, K. A magnetic propeller in the cataclysmic variable AE Aquarii. **MNRAS**, v. 286, p. 436–446, abr. 1997.
- Yoon, S.-C.; Podsiadlowski, P.; Rosswog, S. Remnant evolution after a carbon-oxygen white dwarf merger. **MNRAS**, v. 380, p. 933–948, set. 2007.
- Younes, G.; Kouveliotou, C.; Kargaltsev, O.; Pavlov, G. G.; Göğüş, E.; Wachter, S. XMM-Newton View of Swift J1834.9-0846 and Its Magnetar Wind Nebula. **Astrophysical Journal**, v. 757, p. 39, set. 2012.
- Yuan, H. B.; Liu, X. W.; Xiang, M. S. Empirical extinction coefficients for the GALEX, SDSS, 2MASS and WISE passbands. **MNRAS**, v. 430, p. 2188–2199, abr. 2013.
- Yuasa, T.; Nakazawa, K.; Makishima, K.; Saitou, K.; Ishida, M.; Ebisawa, K.; Mori, H.; Yamada, S. White dwarf masses in intermediate polars observed with the Suzaku satellite. **Astronomy & Astrophysics**, v. 520, p. A25, set. 2010.

Zezas, A.; Trümper, J. E.; Kylafis, N. D. Broad-band X-ray spectra of anomalous X-ray pulsars and soft γ -ray repeaters: pulsars in a weak-accretion regime? **MNRAS**, v. 454, p. 3366–3375, dez. 2015.

Zhou, P.; Chen, Y.; Li, X.-D.; Safi-Harb, S.; Mendez, M.; Terada, Y.; Sun, W.; Ge, M.-Y. Discovery of the Transient Magnetar 3XMM J185246.6+003317 near Supernova Remnant Kesteven 79 with XMM-Newton. **The Astrophysical Journal, Letters** , v. 781, p. L16, jan. 2014.

Zhu, C.; Pakmor, R.; van Kerkwijk, M. H.; Chang, P. Magnetized Moving Mesh Merger of a Carbon-Oxygen White Dwarf Binary. **The Astrophysical Journal, Letters** , v. 806, p. L1, jun. 2015.

Zhu, H.; Tian, W.; Li, A.; Zhang, M. The gas-to-extinction ratio and the gas distribution in the Galaxy. **MNRAS**, v. 471, p. 3494–3528, nov. 2017.

Zhu, W.; Kaspi, V. M.; Dib, R.; Woods, P. M.; Gavriil, F. P.; Archibald, A. M. The Long-Term Radiative Evolution of Anomalous X-Ray Pulsar 1E 2259+586 After Its 2002 Outburst. **Astrophysical Journal**, v. 686, p. 520–527, out. 2008.

Apendices

Appendix A - Principles of photometry

In this appendix, we present the photometric definitions we use in this thesis. We also discuss how interstellar extinction and distance affect the observed flux.

The optical and infrared emissions always are given in magnitude values, which is a logarithmic scale usually measured in a spectral band. In addition, this magnitude can be absolute or apparent. The apparent magnitude represents the brightness of the star seen from the Earth. This magnitude is affected by the distance of the object and by the extinction of the interstellar medium, since the amount of dust present in the path that light travels can significantly alter the final value of magnitude. The absolute magnitude, however, assumes that the object is at a fixed distance of 10 pc ($1 \text{ pc} = 3.09 \times 10^{16} \text{ m}$ or 3.26 light years).

A.1 Solid Angle

A plane angle (eq. A.1) is the ratio between the arc (a) and the radius (r) of a circle. Doing a similar analogy, we can perceive the solid angle (eq. A.2) such as a 'sector' of a sphere, calculated by the ratio between the area (A) on the surface of the sphere and its radius (R) (Filho; Saraiva, 2000). The unit of solid angle is $d\Omega = \sin \theta d\theta d\phi$.

$$\alpha = \frac{a}{r} \tag{A.1}$$

$$\Omega = \frac{A}{R^2} \tag{A.2}$$

A.2 Specific intensity or brightness

The light expands spherically when is emitted by an isotropic source in a homogeneous medium. The amount of energy passing through a unit area per unit time per unit of solid angle is known as the specific intensity (eq. A.3) (Filho; Saraiva, 2000). We can also consider the specific monochromatic intensity, which considers the amount of energy in a given wavelength range $[\lambda, \lambda + d\lambda]$ (eq A.4).

$$I = \frac{dE}{dt dA d\Omega} \quad (\text{A.3})$$

$$I_\lambda = \frac{dE}{dt dA d\Omega d\lambda} \quad (\text{A.4})$$

The monochromatic specific intensity can also be defined from a frequency range, once equation A.5 is valid. In addition, the intensity does not vary with distance, since the amount of energy within an angle remains the same, regardless of where it was emitted.

$$I_\lambda d\lambda = I_\nu d\nu = I_E dE \quad (\text{A.5})$$

A.3 Flux

The flux (f) at a given wavelength is the amount of net energy crossing a unit area, per unit time, per unit wavelength that arrives at a detector (eq A.6) (Filho; Saraiva, 2000). The angle θ is measured between the rays and the normal direction of the area.

$$df_\lambda = \frac{dE}{dA dt d\lambda} = I_\lambda \cos\theta d\Omega \quad (\text{A.6})$$

Thus it is possible to integrate equation A.6 to find the flow at a wavelength (eq A.7).

$$f_\lambda = \int_0^{2\pi} \int_0^{\pi/2} I_\lambda \cos\theta \sin\theta d\theta d\phi \quad (\text{A.7})$$

Unlike the specific intensity, the flux falls with the square of the distance by equation A.8, where R is the radius of the emitting region and D is the distance from the source to the observer.

$$f = \pi I \left(\frac{R}{D} \right)^2 \quad (\text{A.8})$$

The flow can be written as a function of frequency and wavelength by equation A.9.

$$f_\nu = -\frac{\lambda^2}{c} f_\lambda \quad (\text{A.9})$$

Plus, it is possible to define the relation between the flux in units of frequency and wavelength such as A.10.

$$d\nu = \frac{-c}{\lambda^2} d\lambda \quad (\text{A.10})$$

Finally, we can estimate the luminosity by knowing the flux and the distance D by the relation A.11.

$$L = f(4\pi D^2) \quad (\text{A.11})$$

A.4 Radiative transfer

When a light ray passes through a amount of matter, the specific intensity will probable change due to emission, that adds energy, or absorption, subtracting energy (Rybicki; Lightman, 1979).

A.4.1 Emission

The monochromatic emission coefficient j_λ (or j_ν) is the energy emitted per unit time per volume per solid angle per unit wavelength (or frequency) and is defined by equation A.12 (Rybicki; Lightman, 1979).

$$dE = j_\lambda dV d\Omega dt d\lambda \quad (\text{A.12})$$

For an isotropic emitter, equation A.13 is also valid, where P_λ is the radiative power per unit volume per wavelength.

$$j_\lambda = \frac{P_\lambda}{4\pi} \quad (\text{A.13})$$

The intensity added in the rays crossing a region of distance ds and area dA (volume $dV = dsdA$) is given by equation A.14.

$$dI_\lambda = j_\lambda ds \quad (\text{A.14})$$

A.4.2 Absorption

The absorption phenomenology can be understood such as the rays passing through a medium with particles density n , in which each particle of this medium has an absorbing area, or *cross section*, of σ_λ (cm^2). The total amount of absorbers particles through the region is $ndAds$ and the total absorbing area of the absorbers is $n\sigma_\lambda dAds$. This way, the energy absorbed is given by equation A.15 (Rybicki; Lightman, 1979).

$$dE = -dI_\nu dAd\Omega dt d\lambda = I_\lambda (n\sigma_\lambda dAds) d\Omega dt d\lambda \quad (\text{A.15})$$

The loss of intensity is represented in equation A.16.

$$dI_\lambda = -n\sigma_\lambda I_\lambda ds \quad (\text{A.16})$$

Using $\alpha_\lambda = n\sigma_\lambda$, we can also call the loss of intensity by the relation A.17. In this case, α_λ is the absorption coefficient.

$$dI_\lambda = -\alpha_\lambda I_\lambda ds \quad (\text{A.17})$$

A.4.3 Radiative transfer equation

A region can have both phenomenology, absorption and emission. For that reason, the expression A.18 is a more reliable relation to express the intensity change and the coefficients (Rybicki; Lightman, 1979).

$$\frac{dI_\lambda}{ds} = -\alpha_\lambda I_\lambda + j_\lambda \quad (\text{A.18})$$

In the case where we only have emission, the coefficient α_λ is zero and the equation reduces to:

$$\frac{dI_\lambda}{ds} = j_\lambda$$

Where the solution is:

$$I_\lambda(s) = I_\lambda(s_0) + \int_{s_0}^s j_\lambda(s') ds'$$

On the other hand, when the $j_\lambda = 0$ and only absorption occurs, we have the relation:

$$\frac{dI_\lambda}{ds} = -\alpha_\lambda I_\lambda$$

and the solution:

$$I_\lambda(s) = I_\lambda(s_0) \exp \left[- \int_{s_0}^s \alpha_\lambda(s') ds' \right]$$

A.4.4 Optical depth

We can define the optical depth along the path of a travelling ray such as equation A.19 (Rybicki; Lightman, 1979). In this case, a medium is optical thick or opaque when $\tau_\lambda > 1$ whereas a medium is optically thin or transparent when $\tau_\lambda < 1$.

$$\tau_\lambda(s) = \int_{s_0}^s \alpha_\lambda(s') ds' \quad (\text{A.19})$$

Using this equation we can rewrite the transfer equation such as A.20.

$$\frac{dI_\lambda}{d\tau_\lambda} = -I_\lambda + S_\lambda \quad (\text{A.20})$$

We can also define the source function S_λ by the relation A.21.

$$S_\lambda = \frac{j_\lambda}{\alpha_\lambda} \quad (\text{A.21})$$

The solution of this new equation is:

$$I_\lambda(\tau_\lambda) = S_\lambda + e^{-\tau_\lambda} (I_\lambda(0) - S_\lambda)$$

For an emitting ray created in the region we have $I_\lambda(0) = 0$ and the equation reduces to:

$$I_\lambda(\tau_\lambda) = S_\lambda (1 - e^{-\tau_\lambda})$$

For and optical depth $\tau_\lambda \ll 1$, we have $e^{-\tau_\lambda} = 1 - \tau_\lambda$. Thus, we can write equation A.22.

$$I_\lambda(\tau_\lambda) = S_\lambda \tau_\lambda \quad (\text{A.22})$$

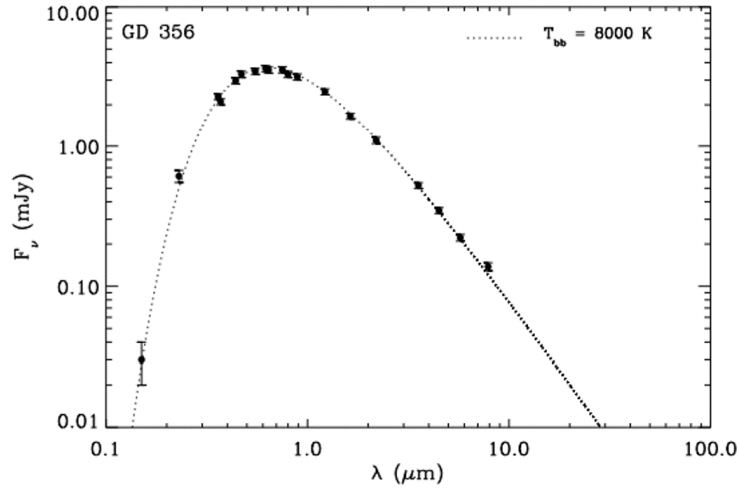


FIGURE A.1 – SED of the WD GD 356. The black dots are the observed flux and the dotted line is a blackbody with $T=8000$ K. Reference: Wickramasinghe *et al.* (2010)

A.5 Blackbody radiation

A blackbody is an idealized physical body that absorbs all the incident electromagnetic radiation, independent of the frequency or angle of incidence. Such body is in thermal equilibrium and emits electromagnetic radiation, represented by Planck's law (eq. A.23).

$$B(\lambda, T) = \frac{2hc^2}{\lambda^5} \frac{1}{e^{hc/\lambda k_B T} - 1} \quad (\text{A.23})$$

Equation A.23 shows the specific monochromatic intensity ($B(\lambda, T)$) of the radiation emitted by a blackbody at a given temperature T , which is equivalent to the source function S_λ defined by equation A.21 (Rybicki; Lightman, 1979). In this equation, h is the Planck constant, λ , the wavelength, c , the velocity of light, and k_B , the Boltzmann constant. The bolometric luminosity of a blackbody can be calculated by equation A.24.

$$L_{bol} = 4\pi R^2 \sigma T_e^4 \quad (\text{A.24})$$

A blackbody has two remarkable properties: it is an ideal emitter, which means that it emits equal or more thermal energy than any other body at the same temperature and its energy is isotropically emitted, regardless of the region.

The photosphere of a WD is well idealized by a blackbody, and therefore, such a model was used throughout the work. Figure A.1 shows the spectra of the magnetic WD GD 356 and its comparison with a blackbody model. It is possible to realize the remarkable correlation between the observational data and the model.

A.6 Relation between flux and apparent magnitude

We use equation A.25 to calculate of the apparent magnitude of the source in a given band from an flow value (LÉNA *et al.*, 1998).

$$m = -2.5\log[(f_\lambda)/e_{\lambda_0}] + A_{\lambda_0}. \quad (\text{A.25})$$

In equation A.25, λ_0 is the wavelength in which the magnitude was measure, f_λ is the object's flux at that wavelength. A_{λ_0} is the extinction, explained in details in the section A.8 and e_0 is the zeropoint, displaced in the section A.7.

A.7 Photometric Systems

Magnitude is not given for a specific wavelength. It is measured in regions of the spectrum, called bands, instead. The bands we use in this thesis are shown in Tables A.1, A.2 and A.3, representing each photometric system. Different bands of a given photometric system are defined by their spectral response, such as Figure A.2, detailed in section A.7.1. The spectral response curve can be relatively complex so that we usually represent/simplify a given band by the central wavelength (λ_0), and its width ($\Delta\lambda_0$). A photometric system also determines how the conversion between magnitude and flow is made. Thus, the reference flows (e_0), or the zeropoint, of each band need to be defined and are presented in Tables A.1, A.2 and A.3.

TABLE A.1 – Johnson-Cousin photometric system. Reference: Léna *et al.* (1998)

Bands	λ_0 (μm)	$\Delta\lambda$ (μm)	e_0 (Jy)
U	0.36	0.068	1880
B	0.44	0.098	4650
V	0.55	0.089	3950
R	0.70	0.22	2870
I	0.90	0.24	1770

TABLE A.2 – Near-Infrared bands. Reference: Léna *et al.* (1998)

Bands	λ_0 (μm)	$\Delta\lambda$ (μm)	e_0 (Jy)
J	1.25	0.30	636
H	1.65	0.35	629
K	2.20	0.40	312

The photometric system SDSS is an AB system, thus, the zeropoint value is 3631 Jy (1 Jy = $10^{-26} W m^{-2} Hz^{-1}$; Jansky (Jy) is a unit used in astronomy for flux density) for any band.

TABLE A.3 – SDSS photometric system. Reference: Fukugita *et al.* (1996)

Bands	λ_0 (μm)	$\Delta\lambda$ (μm)	e_0 (Jy)
u'	0.35	0.046	3631
g'	0.48	0.099	3631
r'	0.62	0.096	3631
i'	0.76	0.106	3631
z'	0.91	0.125	3631

A.7.1 Sensitivity function

The sensitivity function, $t_0(\lambda)$, is the spectral response of each band, and is used to describe the fraction of the flux detected at a given wavelength. To find the magnitude for a particular spectral band, equation A.25 must be integrated, taking into account the sensitivity function, since equation A.25 is only correct for a specific wavelength while a band is a continuous set of lengths, each one with different sensitivity. The final result can be found using equation A.26:

$$m_{(\lambda_0)} = -2.5 \log \int_0^\infty t_o(\lambda) e(\lambda) d\lambda + 2.5 \log \int_0^\infty t_o(\lambda) d\lambda + 2.5 \log e_0 \quad (\text{A.26})$$

Figure A.2 represents the sensitivity function for the Johnson-Cousins and SDSS photometric systems.

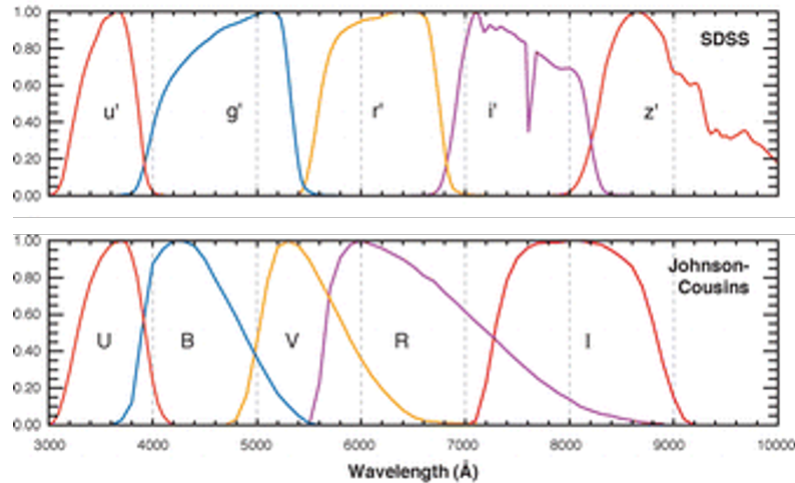


FIGURE A.2 – Sensitivity function for the photometric systems Johnson-Cousins and SDSS and its bands. Adapted from Bessell (2005)

A.8 Interstellar extinction

On a dark night, we can observe the sky has some bright regions and others fairly darker. Such dark regions are not lacking in stars, they are located in directions where clouds of gas and dust do not allow amounts of starlight to reach us instead. This phenomenon is known as interstellar extinction and is a result of two factors: scattering and absorption. A schematic view of such a phenomenon is represented in Figure A.3 (CARROLL; OSTLIE, 2007).

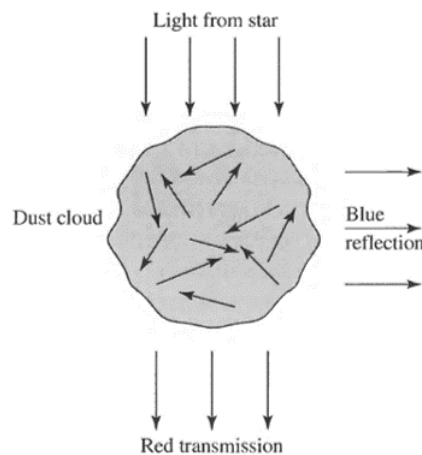


FIGURE A.3 – Extinction caused by the dust present in a interstellar cloud. Reference: Carroll & Ostlie (2007).

$A(\lambda)$ is the amount of interstellar extinction at a given wavelength. The extinction that the radiation will suffer while pass through a cloud varies according to the density of the grains and the thickness of this cloud. In addition, shorter wavelengths are more affected, leading infrared emission to suffer less from the effects of interstellar extinction than optical.

The extinction varies according to the direction, since the gas and dust of the interstellar medium are not equally distributed, and the distance from the star to Earth, leading farther sources to find a greater number of clouds.

If the telescope used is not in orbit, a component of the radiation is lost when the light enters Earth's atmosphere. In this case, the band U, closest to ultraviolet, is the most affected. This atmospheric extinction is neglected in the calculations, once we expect that the papers have already considered such effect and published the values of magnitude out of the atmosphere.

In order to find the value of the interstellar extinction of the SGR/AXPs we adopt two methodologies, described in the chapter 2.

Appendix B - Magnetic field for SGR/AXPs in the accreting WD model

To estimate the magnetic field of SGR/AXPs in the accreting WD model we proceed as follow. All SGR/AXPs have spin-down instead of spin-up. Thus, we must have $0.975 < R_m/R_c < 1$ for the accreting regime to causes spin-down (see sec. 5.3). Thus, we can get an estimate of magnetic field for the SGR/AXPs in the accretion WD model by doing $R_m = R_c$.

Equation 4.20 gives the value of R_m and equation 5.3 gives R_c . The spin period were taken from Table 2.1. The parameters \dot{M} and f were taken from the soft X-rays observations (see Tables 2.11 and 2.12). We consider $\beta = 90^\circ$ and the same mass and radius of 4U 0142+61 for all sources ($M_{wd} = 1.41 M_\odot$ and $R_{wd} = 1021$ km).

In section 2.5 we present the soft X-rays properties for the SGR/AXPs for two different fit models: BB+BB and BB+PL. We estimate the magnetic field for those two models separately. Table B.1 presents the estimated magnetic field for the BB+BB fit in the accreting WD model.

TABLE B.1 – Estimated magnetic field for SGR/AXP using the BB+BB model. \dot{M} = accretion rate in 10^{16} g.s $^{-1}$; f = fraction of the WD surface occupied by the accretion; R_c = corotational radius in 10^8 cm; B = magnetic field in 10^7 G.

Name	\dot{M}	f	R_c	B
CXOU J010043.1	3.72	16.15	6.72	4.24
SGR 0526	10.76	10.92	6.74	6.45
1E 1048.1	0.25	0.50	5.82	10.70
1RXS J170849.0	1.42	4.49	8.30	9.53
SGR 1806	3.31	0.96	6.45	15.80
1E 1841	11.14	4.81	8.69	15.30
SGR 1900	1.37	0.28	5.03	15.80
1E 2259	0.78	0.19	1.45	24.40

Table B.1 presents the estimated magnetic field for the BB+PL fit in the accreting WD model.

TABLE B.2 – Estimated magnetic field for SGR/AXP using the BB+PL model. \dot{M} = accretion rate in 10^{16} g.s $^{-1}$; f = fraction of the WD surface occupied by the accretion; R_c = corotational radius in 10^8 cm; B = magnetic field in 10^7 G.

Name	\dot{M}	f	R_c	B
CXOU J0100	3.60	9.35	6.72	5.53
SGR 0501	0.21	0.04	5.39	32.60
SGR 0526	15.10	4.14	6.74	11.20
1E 1048.1	2.42	0.32	5.82	21.40
1E 1547.0	0.07	0.05	2.73	7.01
SGR 1647	0.61	0.14	3.17	8.31
CXOU J164710.2	0.02	0.002	8.10	189
1RXS J170849.0	11.20	0.92	8.30	32.20
SGR 1806	4.82	1.30	6.45	14.70
1E 1841	11.80	4.46	8.69	16.0
SGR 1900	1.63	0.38	5.03	14.10
SGR 1935	0.87	0.17	3.68	10.60
1E 2259	0.93	1.28	6.12	9.62

The luminosities from Tables 2.11 and 2.12 are an order of magnitude estimates and the magnetic field varies with $(L_X)^{0.5}$ (see eqs. 4.2 and 4.20). To get a more correct estimate of the magnetic field we would have to fit the SED of all SGR/AXPs and get their X-rays bolometric luminosities. However, our estimates from Tables B.1 and B.2 gives an order of magnitude estimate for the magnetic fields of SGR/AXPs, which is sufficient for our analysis.

The average magnetic field of SGR/AXPs estimated in the accreting WD model is consistent with the classes of magnetic CVs and isolated magnetic WDs, such as we discuss in Section 5.3.

Moreover, the average magnetic field from the BB+BB fit is smaller than from the BB+PL fit. This happens because both blackbodies components of the BB+BB fit have estimated radius. Thus, the fraction f is estimated considering the sum of the area for both components. For the BB+PL fit, only the blackbody have an estimated radius. Thus, we only consider the occupied area for the blackbody emission, which underestimate the value of f. Consequently, the magnetic field estimate for the BB+PL model is overestimated due to the unfamiliarity with the occupied area of the power-law component.

FOLHA DE REGISTRO DO DOCUMENTO

1. CLASSIFICAÇÃO/TIPO DM	2. DATA 26 de novembro de 2018	3. DOCUMENTO No. DCTA/ITA/DM-092/2018	4. No. DE PÁGINAS 137
5. TÍTULO E SUBTÍTULO: Emission models of Soft Gamma-Ray Repeaters/Anomalous X-Ray Pulsars described as White Dwarfs			
6. AUTORA(ES): Sarah Villanova Borges			
7. INSTITUIÇÃO(ÕES)/ÓRGÃO(S) INTERNO(S)/DIVISÃO(ÕES): Instituto Tecnológico de Aeronáutica – ITA			
8. PALAVRAS-CHAVE SUGERIDAS PELA AUTORA: Magnetares; Anãs Brancas; Acreção; Estrelas de nêutron			
9. PALAVRAS-CHAVE RESULTANTES DE INDEXAÇÃO: Estrelas anãs; Campos magnéticos estelares; Aglomerações; Estrelas de nêutrons; Astrofísica; Física.			
10. APRESENTAÇÃO: <input checked="" type="checkbox"/> Nacional <input type="checkbox"/> Internacional ITA, São José dos Campos. Curso de Mestrado. Programa de Pós-Graduação em Física, Área de Física Nuclear. Orientadora: Profa Cláudia Vilega Rodrigues. Defesa em 22/10/2018. Publicada em 2018.			
11. RESUMO: As fontes astrofísicas <i>Soft Gamma Repeaters</i> (SGR) e <i>Anomalous X-Ray Pulsars</i> (AXP) apresentam uma luminosidade quiescente em raios-X moles, no intervalo de 2 – 10 keV, da ordem de $10^{29} - 10^{35} \text{ erg.s}^{-1}$, período de 2–12 s e <i>spin-down</i> de 10^{-15} a $10^{-10} \text{ s.s}^{-1}$. Em geral, os SGR/AXPs apresentam <i>bursts</i> em altas energias, nos quais a luminosidade pode atingir $10^{43} \text{ erg.s}^{-1}$. A natureza da emissão desses SGR/AXPs é motivo de debate e vários cenários já foram propostos. O cenário mais aceito é o modelo magnetar. Neste modelo, as fontes SGR/AXPs apresentam um enorme campo magnético (B), da ordem de $10^{13} - 10^{15} \text{ G}$, e sua luminosidade quiescente em raios-X, bem como os <i>bursts</i> , são produzidos pelo decaimento de seus altíssimos campos magnéticos. No entanto, algumas limitações desse cenário, como a descoberta da fonte de baixo campo magnético ($< 10^{13} \text{ G}$) SGR 0418+5729, aumentaram o interesse por cenários alternativos nos últimos anos. Nesta dissertação, apresentamos um novo cenário para explicar a emissão de SGR/AXPs. Nós propomos que a emissão persistente vem de uma anã branca isolada, que acreta matéria de um disco de detritos. Para testar o modelo, ajustamos a emissão quiescente da AXP 4U 0142+61, que cobre uma ampla faixa de energia, do infravermelho médio aos raios-X duros. Obtivemos um bom ajuste para toda a SED, assumindo que as emissões óticas e infravermelhas são causadas pelo disco de poeira opticamente espesso e pela fotosfera da anã branca, que os raios-X duros são devidos à região pós-choque da coluna de acreção e que os raios-X moles são formados por uma mancha quente na superfície da anã branca. Os parâmetros ajustados apontam para uma anã branca rápida, massiva e altamente magnética. Tal anã branca provavelmente formou-se durante a coalescência de duas anãs brancas menos massivas. Nós também estimamos o campo magnético para os SGR/AXPs no cenário de acreção em anãs brancas e apresentamos novas estimativas de distância para 7 SGR/AXPs, incluindo 4U 0142+61.			
12. GRAU DE SIGILO: <input checked="" type="checkbox"/> OSTENSIVO <input type="checkbox"/> RESERVADO <input type="checkbox"/> SECRETO			